

The Star-Forming Region in Orion KL

L. I. Matveyenko^{1*}, K. M. Zakharin¹, P. J. Diamond^{2**}, and D. A. Graham^{3***}

¹Space Research Institute, Profsoyuznaya ul. 84/32, Moscow, 117997 Russia

²Nuffield Radio Observatory, Macclesfield, Cheshire SK11, 9DL, UK

³Max-Planck-Institut für Radioastronomie, Auf dem Hügel 69, 53121 Bonn, Germany

Received May 12, 2003

Abstract—We have studied the fine structure of the active H₂O supermaser emission region in Orion KL with an angular resolution of 0.1 mas. We found central features suggestive of a bipolar outflow, bullets, and an envelope which correspond to the earliest stage of low-mass star formation. The ejector is a bright compact source ≤ 0.05 AU in size with a brightness temperature $T_b \cong 10^{17}$ K. The highly collimated bipolar outflow ~ 30 has a velocity $v_{ej} \cong 10$ km s⁻¹, a rotation period of ~ 0.5 yr, a precession period of ~ 10 yr, and a precession angle of $\sim 33^\circ$. Precession gives rise to a jet in the shape of a conical helix. The envelope amplifies the radio emission from the components by about three orders of magnitude at a velocity $v = 7.65$ km s⁻¹.

© 2003 MAIK “Nauka/Interperiodica”.

Key words: *star formation, accretion disks, maser emission.*

INTRODUCTION

Gravitational instabilities in gas–dust complexes give rise to local active zones that contain protostars in the phase of gravitational contraction. Physical conditions and chemical reactions lead to the formation of both simple and complex molecules accompanied by intense water-vapor maser emission. We investigated the fine structure of the H₂O supermaser zone in Orion KL at various epochs by using global VLBI network observations in 1985 and NRAO VLBA observations at subsequent epochs.

THE EPOCH OF ACTIVITY 1979–1987

Outbursts of H₂O supermaser emission were observed in Orion KL from 1979 to 1987. In October 1985, the maser emission was concentrated in a narrow line profile with a width of ~ 42 kHz; the peak flux densities reached $F_{\text{peak}} \sim 2$ MJy (Matveyenko 1981). A 10.8-AU-long chain of five groups of compact sources was observed; the sizes of the individual sources were ~ 0.1 AU (Fig. 1). The group velocities increased along the chain from 6.45 (west) to 8.75 km s⁻¹ (east). The brightest components had $v = 7.7$ km s⁻¹, $T_b = 5 \times 10^{16}$ K and $v = 7.9$ km s⁻¹, $T_b = 9 \times 10^{16}$ K. The maser emission was linearly

polarized, $P \approx 70\%$. We interpreted the chain of compact components as a thin disk separated into rings during Keplerian motion seen edge-on (Matveyenko *et al.* 1988). This model assumes the presence of a central protostar with a mass of $(0.1–0.5)M_\odot$, an inner ring radius $R_{\text{in}} \cong 6$ AU, a rotation velocity $v_{\text{rot}} = 5$ km s⁻¹, and an expansion velocity $v_{\text{exp}} \cong 3.8$ km s⁻¹. The outer ring radius is $R \cong 16.5$ AU and $v_{\text{rot}} = 3$ km s⁻¹. The expansion velocity corresponds to “maser rings” containing sublimed water-vapor molecules accelerated by radiation pressure and stellar wind. The active region is surrounded by an envelope that amplifies the emission of the

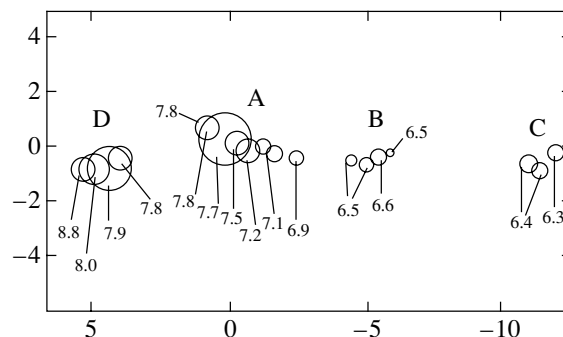


Fig. 1. The distribution of maser spots in October 1985. Relative right ascension and declination (in mas) are along the vertical and horizontal axes, respectively. The circle diameters are proportional to the logarithm of the intensity of the components. The maximum brightness is $T_b \approx 10^{17}$ K.

*E-mail: lmatveen@mx.iki.rssi.ru

**E-mail: pdiamond@jb.man.ac.uk

***E-mail: p062gra@mpifr-bonn.mpg.de

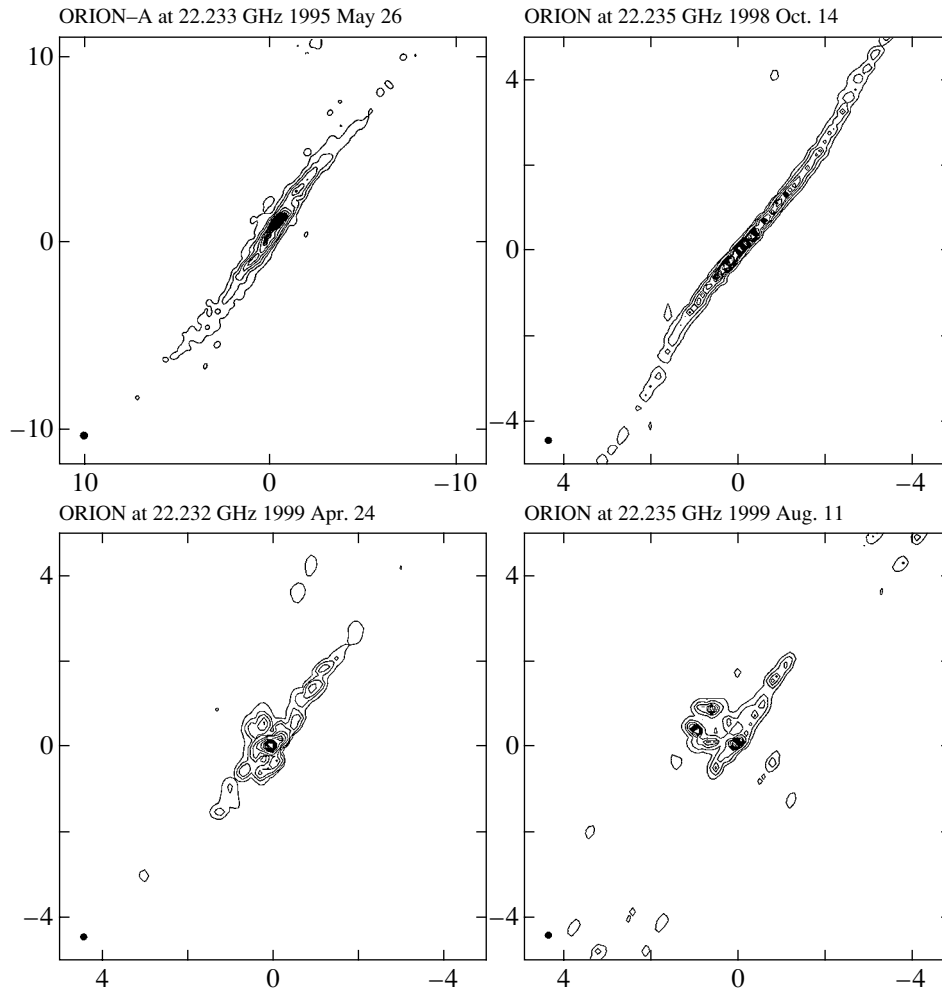


Fig. 2. The structure of the H₂O supermaser emission in the active region of Orion KL (scales in mas). The synthesized beam is shown in the lower left corner of each map; the epoch of observations is given above the maps.

components with $v = 7.65 \text{ km s}^{-1}$ by more than two orders of magnitude.

THE EPOCH OF QUIESCENCE

On May 25, 1995, we investigated the region with an ultrahigh angular resolution of 0.1 mas, or 0.04 AU (Matveenko *et al.* 1998, 2000, 2002). A 9×0.05 AU jet and two compact “bullet” components were detected. A bright, compact source, the presumed ejector, and an elongated 0.5×0.04 AU feature at a position angle of -44° with brightness temperature $T_{\text{ej}} \cong 10^{13}$ K and $T_{\text{jet}} \cong 10^{12}$ K are located at the jet center (Fig. 2). The interaction of bullets with the ambient medium, radiation pressure, and stellar wind form a comet-like head–tail structure. The tail can be in front of or behind the head. The maser emission is linearly polarized, $P \cong 55\%$ (Matveenko *et al.* 1998).

THE ACTIVITY PERIOD 1998-1999

The intensity of the H₂O maser emission exponentially increased, reaching 4.3 MJy in August 1998, and began to exponentially decrease in November. At the first stage of the outburst (March–October 1998), the structure remained virtually the same as that in the quiescence period (Matveenko *et al.* 1998), but the brightness of the components increased by more than three orders of magnitude, reaching $T_{\text{jet}} \cong 10^{15}$ K and $T_{\text{ej}} \cong 10^{17}$ K (Matveenko *et al.* 2002). At the final phase of activity in January–April 1999, the structure became more complex; additional features appeared in the central region, which can be part of a 1.2×0.8 AU torus ~ 0.15 AU in thickness (Fig. 2). The radial outflow velocity is $v_{\parallel} \cong 0.15 \text{ km s}^{-1}$. The velocity in the plane of the sky, $v_{\perp} \cong 10 \text{ km s}^{-1}$, is observed immediately before the outburst peak; at the peak, this velocity decreased to 6 km s^{-1} and reached $\sim 3 \text{ km s}^{-1}$ at the

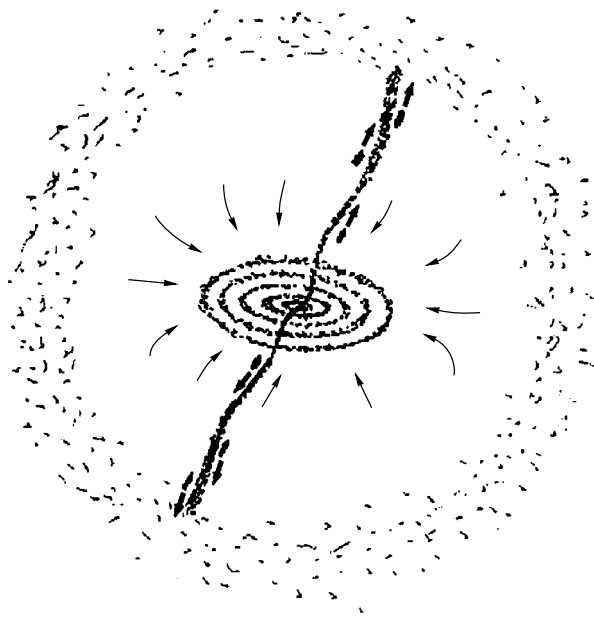


Fig. 3. A model of the star-forming region.

end of the activity period. The bipolar outflow has a helical structure whose pitch and diameter increase with distance from the ejector: $T = 1.3R^{0.7}$ mas, $\varnothing = 0.24R^{0.8}$ mas. The observed structural changes are probably attributable to precession of the rotation axis with a period of 110 months and a precession angle $X \approx 30^\circ$. The intensity of the ejector emission line seen at a velocity of 7.65 km s^{-1} in the $\Delta v = 0.42 \text{ km s}^{-1}$ band is $I = 3 \times 10^5$ Jy/beam. The line profile has broad wings, which are determined by the outflow rotation. The outflow radius is $R = 0.02 \text{ AU}$, and the rotation period is $T \sim 5$ months. This profile is determined by amplification in the envelope by a factor of approximately 450.

CONCLUSIONS

Our studies of the active region in Orion KL with an ultrahigh angular resolution reaching 0.1 mas or 0.05 AU during 1979–1999 have shown the following:

—The structure at an early formation stage of a low-mass star includes an accretion disk, a bipolar outflow, and accompanying maser emission (Fig. 3), which corresponds to the model by Bachiller (1998).

—The accretion disk is at the stage of separation into protoplanetary rings. The disk is $\sim 32 \text{ AU}$ in diameter and $\sim 0.05 \text{ AU}$ in thickness; a torus $\sim 1.2 \text{ AU}$

in diameter and 0.15 AU in thickness is located in the central part. The mass of the central body is $(0.1\text{--}0.5)M_\odot$.

—The accretion and ejection of matter are different aspects of the same process. The ejector size is $\leq 0.05 \text{ AU}$, and the brightness temperature is $T_b \cong 10^{17} \text{ K}$. The ejected matter contains H_2O molecules. The outflow velocity is $\sim 10 \text{ km s}^{-1}$. The outflow collimation reaches ~ 30 .

—The ejector rotation velocity is $v_{\text{rot}} \sim 1.1 \text{ km s}^{-1}$, and the rotation period is $T \sim 0.5 \text{ yr}$. The precession period reaches about 10 yr , and the precession angle is $\sim 30^\circ$. The precession angle decreases by a factor of 2 at a distance of $\sim 1 \text{ AU}$, and the delay of rotation is 3.3 yr . Precession forms the helical structure of the outflow.

—The bullets have comet-like head–tail structures. The emission of the structures is amplified in the surrounding envelope at velocity $v = 7.65 \text{ km s}^{-1}$ within a 0.5-km s^{-1} -wide maser window.

—The maser emission of the bipolar outflow is pumped by collisions with the ambient medium while the maser emission of the rings is associated with infrared radiation from the central body (IRC4).

—The outburst polarization results from pumping anisotropy. The degree of polarization depends on the radiation flux density: $P = (30 + 6.4 \times F) [\%]$, where F is in MJy.

REFERENCES

1. R. Bachiller, *Ann. Rev. Astron. Astrophys.* **34**, 111 (1998).
2. L. I. Matveenko, *Pis'ma Astron. Zh.* **7**, 100 (1981) [*Sov. Astron. Lett.* **7**, 54 (1981)].
3. L. I. Matveenko, P. D. Diamond, and D. A. Graham, *Pis'ma Astron. Zh.* **24**, 723 (1998) [*Astron. Lett.* **24**, 623 (1998)].
4. L. I. Matveenko, P. D. Diamond, and D. A. Graham, *Astron. Rev.* **80**, 592 (2000).
5. L. I. Matveenko, P. D. Diamond, and D. A. Graham, *IAU Symp. 206: Cosmic Masers: from Protostars to Blackholes*, Ed. by V. Migenes and M. J. Reid (2002), p. 96.
6. L. I. Matveenko, D. A. Graham, and P. D. Diamond, *Pis'ma Astron. Zh.* **14**, 1101 (1988) [*Sov. Astron. Lett.* **14**, 468 (1988)].

Translated by L. Matveyenko

RXTE Observations of the Strongly Absorbed Sources IGR J16318–4848 and IGR J16358–4726

M. G. Revnivtsev*

Max-Planck Institut fur Astrophysik, Karl-Schwarzschild-Str. 1, 85748 Garching, Germany
Space Research Institute, Russian Academy of Sciences, Profsoyuznaya ul. 84/32, Moscow, 117810 Russia

Received April 22, 2003

Abstract—We analyzed the RXTE observations of two strongly absorbed sources, IGR J16318–4848 and IGR J16358–4726. We were able to obtain the 3–25 keV spectra of the sources by taking into account the contribution of the Galactic diffuse background to the X-ray flux recorded with the RXTE/PCA spectrometer. The spectra of the sources are well described by a power-law decrease of the photon flux with energy with a photon index of ~ 1 and strong photoabsorption. The photoabsorption column density $n_{\text{H}}L$ for IGR J16318–4848 derived from the RXTE observation on March 14.1, 2003, is shown to be much higher than its value obtained by the XMM observatory on February 10.7, 2003. This result may suggest that the source has variable absorption that may depend on the orbital phase of the system. We point out that all of the three X-ray sources discovered by the INTEGRAL observatory in the region $(l, b) \sim (336, 0)$ (IGR J16318–4848, IGR J16320–4751, and IGR J16358–4726) have strong intrinsic photoabsorption and may be high-mass binaries. Their proximity to the region where the tangent to the Galactic spiral arm passes, i.e., to the region of enhanced concentration of young high-mass stars, can serve as an indirect confirmation of this assumption. If our assumption about the positions of the sources in the Norma spiral arm is valid, then we can roughly estimate their heliocentric distances: ~ 6 –8 kpc.
© 2003 MAIK “Nauka/Interperiodica”.

Key words: *RXTE observatory, strongly absorbed X-ray sources.*

INTRODUCTION

Several sources with strong photoabsorption in the X-ray spectrum were discovered in the first few months of the Galactic-plane survey with the INTEGRAL observatory: IGR J16318–4848 (Courvoisier *et al.* 2003; Murakami *et al.* 2003), IGR J16320–4751/AX J1631.9–4752 (Tomsick *et al.* 2003), and IGR J16358–4726 (Revnivtsev *et al.* 2003a, 2003b).

Shortly after its discovery, IGR J16318–4848 was observed by the XMM observatory (Schartel *et al.* 2003; de Plaa *et al.* 2003), which allowed it to be accurately localized and identified with its infrared and optical components (Foschini *et al.* 2003; Revnivtsev *et al.* 2003c). Analysis of the infrared and optical measurements of the companion star showed that the X-ray binary IGR J16318–4848 most likely contains a supergiant that is responsible for observational manifestations (strong photoabsorption inside the system and extremely intense fluorescent lines of neutral iron) similar to those in the system of the long-period pulsar GX301-2 (Revnivtsev *et al.* 2003c).

The XMM and CHANDRA observations of IGR J16320–4751 and IGR J16358–4726 (Rodriguez *et al.* 2003; Kouveliotou *et al.* 2003) have not yet allowed the optical companions of the X-ray sources to be accurately determined. However, in both cases, the most likely companions are bright, possibly high-mass stars.

In this paper, we analyze the RXTE observations of the sources IGR J16318–4848 and IGR J16358–4726.

ANALYSIS OF OBSERVATIONS AND RESULTS

The sources IGR J16318–4848 and IGR J16358–4726 were observed by the RXTE observatory on March 14.1 and 25.9, 2003, respectively. The effective exposure was 6.5 and 3.1 ks, respectively. Since the sources are located in a fairly crowded region of the sky, and since the field of view of the main RXTE instrument (PCA) is 1° , the RXTE orientation during the observations was chosen so as to best eliminate the possible contribution from known bright sources. Figure 1 shows a map of the region around the sources with the RXTE/PCA fields of view superimposed.

*E-mail: mikej@hea.iki.rssi.ru

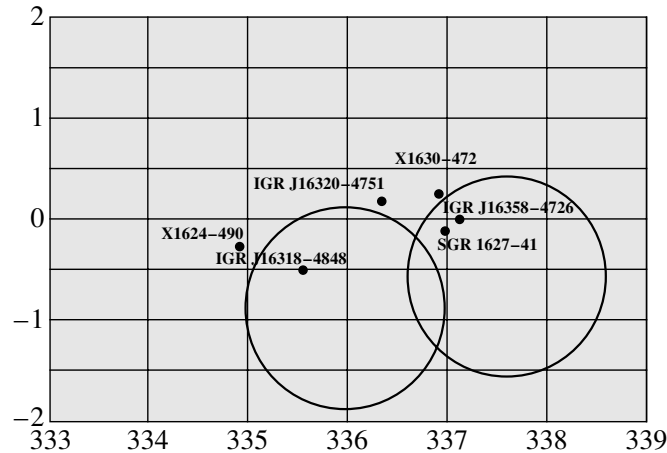


Fig. 1. The positions of known bright sources in the region of IGR J16318–4848 and IGR J16358–4726. The large circles indicate the edges of the RXTE/PCA field of view during the observations analyzed here.

To process the RXTE/PCA data, we used the standard FTOOLS/LHEASOFT 5.2 software package. Since the sources are relatively faint and since they were not located at the center of the field of view in both observations (which additionally decreased the number of photons recorded from these sources) we paid special attention to the correct allowance for the instrumental PCA detector background. For this purpose, we excluded from our analysis the data of the PCU0 detector, because the propane veto layer had been absent from it since May 2000, causing a significant deterioration of the instrumental noise subtraction. In addition, we used data only for the upper anode layer (LR1), because the systematic errors in the instrumental noise are smallest for this layer. To model the RXTE/PCA instrumental background, we used the L7_240 model.

The large contribution from the Galactic diffuse background (Galactic ridge emission) to the RXTE/PCA X-ray flux poses a serious problem for the observational data processing. Thus, for example, the flux from IGR J16318–4848 in the energy range 2–10 keV is ~ 0.1 – 0.2 mCrab (see, e.g., de Plaa *et al.* 2003; Revnivtsev *et al.* 2003b), while the total flux from the Galactic diffuse background within the PCA field of view is 3–5 mCrab in this region (Valinia and Marshall 1998; Revnivtsev *et al.* 2003b).

To allow for the contribution of the Galactic diffuse background, we used the results of the analysis presented by Valinia and Marshall (1998) and Revnivtsev *et al.* (2003), and the RXTE observations of a region close to IGR J16318–4848 and IGR J16358–4726; more specifically, the off-state observations of SGR 1627–41 (November 19–20, 2001). Since the spectrum of the Galactic diffuse background is constant, except for the slightly varying photoabsorption column density (Yamasaki *et al.* 1997; Valinia

and Marshall 1998; Tanaka 2002; Revnivtsev *et al.* 2003), we can use the RXTE/PCA spectrum in an empty field as a correction component to the observed RXTE/PCA spectra.

IGR J16318–4848. Figure 2 presents the spectrum of IGR J16318–4848 obtained after averaging the data of all observations. The complete

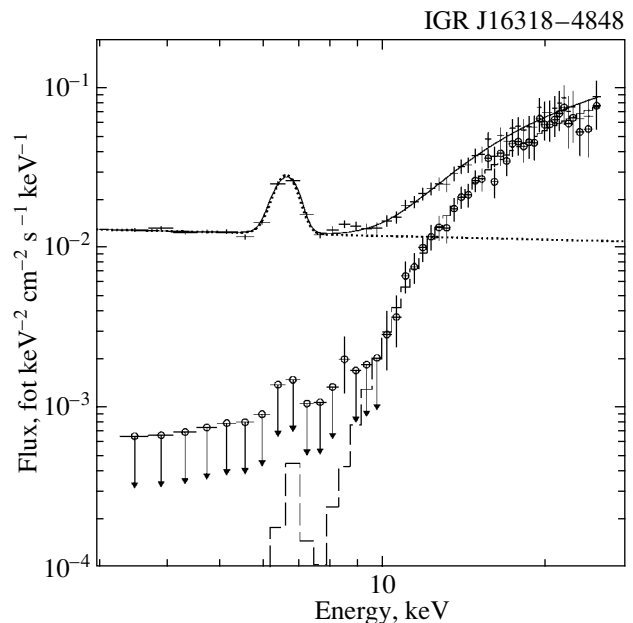


Fig. 2. The spectrum of IGR J16318–4848. The crosses indicate the observed spectrum; the open circles indicate the spectrum of IGR J16318–4848 reconstructed after an allowance made for Galactic ridge emission. The solid curve represents the model of the observed RXTE/PCA spectrum consisting of the diffuse background (dotted curve) and the model of the source proper (dashed curve).

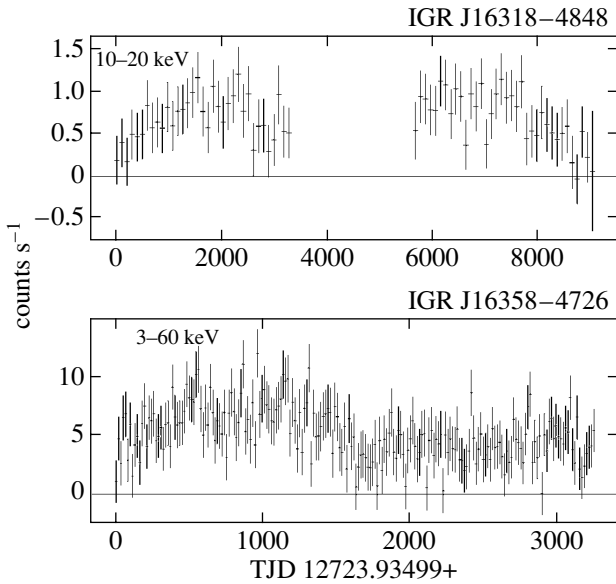


Fig. 3. The light curves of IGR J16318–4848 and IGR J16358–4726.

RXTE/PCA spectrum, which consists of the spectrum of the source itself and the spectrum of the Galactic diffuse background, is also shown in this figure. Note that in this case, the normalization of the source spectrum is a factor of 2.22 smaller than the real one, because the center of the PCA field of view was $\sim 0^{\circ}55$ away from IGR J16318–4848.

To fit the spectrum of the source, we used a simple power-law energy dependence of the photon flux density ($dN(E) \propto E^{-\alpha}dE$) with neutral photoabsorption (model *wabs* of the XSPEC package). This model was successfully used to describe the spectrum of IGR J16318–4848 as observed by the XMM and ASCA observatories (de Plaa *et al.* 2003; Schartel *et al.* 2003; Revnivtsev *et al.* 2003a). It is worth noting that despite the presence of very strong iron emission lines near 6–7 keV in the spectrum of the source (de Plaa *et al.* 2003; Revnivtsev *et al.* 2003c), the influence of the Galactic diffuse background does not allow these lines to be studied by using RXTE/PCA data. The diffuse background flux is more than a factor of 10 higher than the flux from IGR J16318–4848 at energies 6–7 keV (see Fig. 2), and it also contains lines near 6–7 keV. The spectral best-fit parameters are given in the table. The photoabsorption column density obtained exceeds that inferred from the XMM observations of February 10, 2003 (de Plaa *et al.* 2003; Matt and Guainazzi 2003).

Figure 3 shows the light curve of the source constructed from all observations with the Galactic diffuse background subtracted.

Analysis of the power spectrum for the derived light curve revealed no pulsations (Swank and Mark-

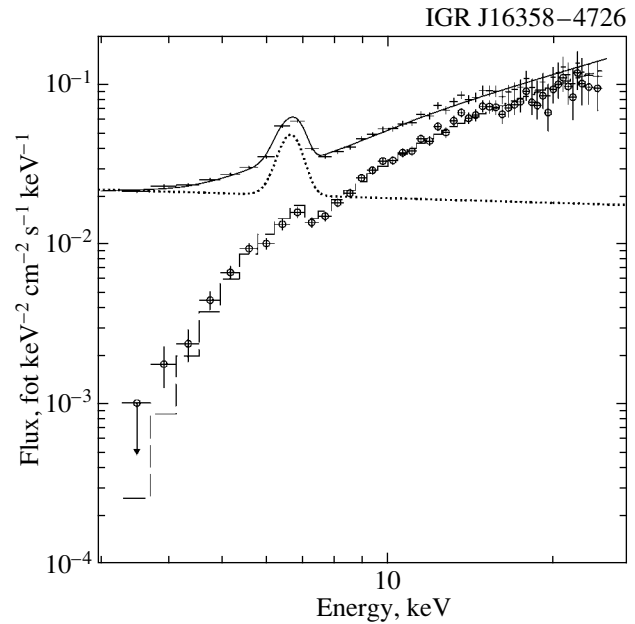


Fig. 4. The spectrum of IGR J16358–4726. The crosses indicate the observed spectrum, and the open circles indicate the spectrum reconstructed after an allowance made for the contribution of the Galactic diffuse background. The solid curve represents the model of the observed RXTE/PCA spectrum composed of the diffuse background model (dotted line) and the model of the source proper (dashed line).

wardt 2003); the 2σ upper limit on the possible pulse fraction of pulsations with frequencies 0.01 Hz–1 kHz in the energy range 10–20 keV is about 10–15%. The upper limit on the pulse fraction of pulsations with longer periods, as, for example, in the pulsar GX301–2 (670 s) or IGR J16358–4726 (5860 s, Kouveliotou *et al.* 2003) is even larger, ~ 20 –50%. At energies below ~ 10 keV, the light curve cannot be analyzed, because the source is weak compared to the Galactic diffuse background (see Fig. 2).

IGR J16358–4726. Figure 4 shows the spectrum of the source obtained by averaging the data of all observations. Just as in the case of IGR J16318–4848, the figure shows the complete RXTE/PCA spectrum, which also consists of the spectrum of the source under study and the spectrum of the Galactic diffuse background.

We used the same model as for IGR J16318–4848 to fit the spectrum of the source—a power-law decrease of the photon flux density with neutral photoabsorption. The spectral best-fit parameters are given in the table. These parameters agree well with the CHANDRA results (Kouveliotou *et al.* 2003).

As expected, the flux from the Galactic diffuse background in these observations was higher than

Spectral best-fit parameters for the sources

Parameter	IGR J16318–4848	IGR J16358–4726
Photoabsorption column density $N_{\text{H}}L$, 10^{22} cm^{-2}	310 ± 70	40 ± 10
Photon index α	1.0 ± 0.5	1.1 ± 0.2
Flux ^a (3–25 keV), $10^{-10} \text{ erg s}^{-1} \text{ cm}^{-2}$	1.1	5.4

^aThe observed fluxes from the sources were corrected for collimator transmittance.

that from IGR J16318–4848 (see Figs. 2 and 4), because the center of the PCA field of view was ~ 0.5 closer to the Galactic plane (Fig. 1). The normalization of the diffuse background spectrum determined when fitting the observed spectrum by the adopted model agrees well with the results of Valinia and Marshall (1998) and Revnivtsev *et al.* (2003).

The light curve of IGR J16358–4726 does not allow the pulsations with a period of 5.86 ks found by Kouveliotou *et al.* (2003) to be analyzed, because the duration of the observation being analyzed is only 3.1 ks. No pulsations or quasi-periodic flux oscillations are observed at higher frequencies. The upper limit on the possible pulse fraction of coherent pulsations at frequencies 0.01 Hz–1 kHz is ~ 10 –15%.

DISCUSSION

In previous sections, we analyzed the RXTE observations of two strongly absorbed sources, IGR J16318–4848 and IGR J16358–4726. Despite the faintness of the systems under study, the strong influence of the Galactic diffuse background, and the proximity of other bright sources, we managed to obtain the 3–25-keV spectra of the sources owing to the properly chosen observing strategy.

The spectra of the sources are well described by a power-law decrease of the photon flux density with energy ($dN(E) \propto E^{-\alpha} dE$) with neutral photoabsorption (model *wabs * power* of the XSPEC package). Because of the strong influence of the Galactic diffuse background, which contains a number of lines near 6–7 keV, the lines in the spectrum of the sources proper cannot be analyzed. The spectral parameters obtained agree well with the observations of other observatories, except IGR J16318–4848, for which the observed photoabsorption column density $n_{\text{H}}L$ exceeded that obtained by the XMM observatory (de Plaa *et al.* 2003; Matt and Guinazzi 2003).

Although obtaining the spectra of the sources in our case involved significant difficulties (because the contribution of the Galactic diffuse background must be taken into account), we believe that we have correctly determined the spectral parameters. The validity of our method is confirmed by the agreement between the spectral parameters of IGR J16358–4726

obtained here from the RXTE observations of March 25.9, 2003, and from the CHANDRA observation of March 24.2, 2003 (Kouveliotou *et al.* 2003).

Thus, we believe that the excess of the observed photoabsorption column density for IGR J16318–4848 above the XMM value may suggest that the source has variable absorption that may depend on the orbital phase of the system. A similar dependence is observed for a number of X-ray sources in high-mass binaries (see, e.g., GX301-2, Endo *et al.* 2002).

Interestingly, the three X-ray sources discovered by the INTEGRAL observatory in the sky region $(l, b) \sim (336, 0)$ (IGR J16318–4848, IGR J16320–4751, and IGR J16358–4726) have much in common. In particular, all of the three sources have strongly absorbed X-ray spectra (the absorption column densities $n_{\text{H}}L$ greatly exceed their interstellar values toward the sources; see, e.g., Dickey and Lockman 1990). All of the three sources have rather hard X-ray spectra (photon index $\alpha \sim 1$ –1.3) typical of pulsars or high-mass X-ray binaries. We showed that the optical/infrared companion for IGR J16318–4848 is a bright and, possibly, high-mass star (Foschini *et al.* 2003; Revnivtsev *et al.* 2003b). No unequivocal identification of the optical/infrared companions was made for the other two systems. However, they are most likely also bright stars, as in the case of IGR J16318–4848 (Rodríguez *et al.* 2003; Kouveliotou *et al.* 2003). Thus, we can assume that all of the three X-ray sources may be high-mass binaries. This assumption is also confirmed by the fact that the sources are located in the region $(l, b) \sim (336, 0)$, i.e., roughly in the region where the tangent to the Galactic spiral arm in Norma (the Norma arm) passes, i.e., in the region of enhanced concentration of high-mass young stars (see, e.g., Grimm *et al.* 2002). If our assumption that these systems are located in the spiral arm is correct, then we can roughly estimate the heliocentric distances to the sources as 6–8 kpc.

ACKNOWLEDGMENTS

I am grateful to Jean Swank and the RXTE planning team for the observations of IGR J16318–4848

and IGR J16358–4726 and to M. Gilfanov for valuable discussions. We used the data retrieved from the High Energy Astrophysics Science Archive at NASA's Goddard Space Flight Center.

REFERENCES

1. T. Courvoisier, R. Walter, and J. Rodriguez, IAU Circ. No. 8063 (2003).
2. J. M. Dickey and F. J. Lockman, *Ann. Rev. Astron. Astrophys.* **28**, 215 (1990).
3. T. Endo, M. Ishida, K. Masai, *et al.*, *Astrophys. J.* **574**, 879 (2002).
4. L. Foschini, J. Rodriguez, and R. Walter, IAU Circ. No. 8076 (2003).
5. H.-J. Grimm, M. Gilfanov, and R. Sunyaev, *Astron. Astrophys.* **391**, 923 (2002).
6. C. Kouveliotou, S. Patel, A. Tennan, *et al.*, IAU Circ. No. 8109 (2003).
7. G. Matt and M. Guainazzi, *Mon. Not. R. Astron. Soc.* (2003, in press).
8. H. Murakami, T. Dotani, and R. Wijnands, IAU Circ. No. 8070 (2003).
9. J. de Plaa, P. den Hartog, J. Kaastra, *et al.*, *Astronomer's Telegram* No. 119 (2003).
10. M. Revnivtsev, A. Lutovinov, and K. Ebisawa, *Astronomer's Telegram* No. 131 (<http://atel.caltech.edu>) (2003b).
11. M. Revnivtsev, M. Tuerler, M. Del Santo, *et al.*, IAU Circ. No. 8097 (2003a).
12. M. Revnivtsev, S. Sazonov, T. M. Gilfanov, and R. Sunyaev, *Pis'ma Astron. Zh.* (2003c, in press).
13. J. Rodriguez, J. Tomsick, L. Foschini, *et al.*, *astro-ph/0304139* (2003).
14. N. Schartel, M. Ehle, M. Breittellner, *et al.*, IAU Circ. No. 8072 (2003).
15. J. Swank and C. Markwardt, *Astronomer's Telegram* No. 128 (2003).
16. Y. Tanaka, *Astron. Astrophys.* **382**, 1052 (2002).
17. J. A. Tomsick, R. Lingenfelter, R. Walter, *et al.*, IAU Circ. No. 8076 (2003).
18. A. Valinia and F. Marshall, *Astrophys. J.* **505**, 134 (1998).
19. N. Yamasaki, T. Ohashi, F. Takahara, *et al.*, *Astrophys. J.* **481**, 821 (1997).

Translated by A. Dambis

A Massive Circumstellar Envelope around the Type-II_n Supernova SN 1995G

N. N. Chugai^{1*} and I. J. Danziger²

¹*Institute of Astronomy, Russian Academy of Sciences, Pyatnitskaya ul. 48, Moscow, 109017 Russia*

²*Osservatorio Astronomico di Trieste, via G.B. Tiepolo 11, 34131 Trieste, Italy*

Received May 21, 2003

Abstract—We model the interaction of the supernova SN 1995G with a dense circumstellar (CS) gas in a thin-shell approximation. A model fit to the observed bolometric light curve combined with data on the supernova expansion velocity gives estimates for the density, mass ($\approx 1 M_{\odot}$), and age (≈ 8 yr) of the CS envelope. The determined CS-envelope density is shown to be virtually independent of the assumed mass of the supernova envelope because of the high CS-gas density at which the forward shock wave is essentially radiative. The derived CS-envelope density is consistent with the H α luminosity and with the presence of distinct Thomson scattering in the red wing of this line. The mass of the CS envelope together with its expansion velocity and age indicate that the CS envelope was ejected by the presupernova eight years before the supernova explosion through violent energy release ($\sim 6 \times 10^{48}$ erg).

© 2003 MAIK “Nauka/Interperiodica”.

Key words: *supernovae, stellar evolution, circumstellar gas.*

1. INTRODUCTION

Type-II_n supernovae (SN II_n) with a narrow H α emission line, which were placed in a separate class by Schlegel (1990), explode in a very dense circumstellar (CS) environment. This is evidenced by the very presence of a strong CS H α line, the high bolometric luminosity, and the intense broad H α emission line powered by the shock interaction of the supernova with CS gas (Chugai 1990, 1992). An analysis of the optical effects of the CS interaction is an important diagnostic tool for the CS gas density around SN II_n. The use of this tool led to the detection of an unusually dense CS environment around SN 1987F (Chugai 1992), SN 1997ab (Salamanca *et al.* 1998), SN 1997cy (Turatto *et al.* 2000), and several other SN II_n. When the CS gas velocity is known, the mass loss rate can be estimated. For SN 1997ab with a measured CS gas velocity of $u \sim 90$ km s⁻¹, the mass loss rate is enormous, $\sim 10^{-2} M_{\odot}$ yr⁻¹ (Salamanca *et al.* 1998). The mechanism for such intense mass loss is unclear, because it exceeds the mass loss rate in the most extreme cases of a red supergiant superwind by at least an order of magnitude.

The problem of the mechanism of intense mass loss by SN II_n presupernovae has become even more pressing in connection with the recent results of the

study of SN 1994W. They show that the CS envelope in this case was produced by mass loss with an average rate of $\sim 0.2 M_{\odot}$ yr⁻¹ and an enormous kinetic luminosity that is two orders of magnitude higher than the radiative luminosity of a massive presupernova (Chugai *et al.* 2003). It was suggested there that such intense mass loss for SN 1994W was attributable to an explosive event about 1.5 yr before the supernova explosion. A characteristic feature of this supernova is the relatively high CS gas velocity ($u \approx 10^3$ km s⁻¹), which leads to serious energy problems for the superwind mechanism.

The idea of explosive mass ejection several years before the supernova explosion was first put forward by Weaver and Woosley (1979) in connection with a possible powerful Ne flash in a degenerate O/Ne/Mg core. Grasberg and Nadyozhin (1986) suggested an explosive ejection of the presupernova envelope approximately 50 days before the supernova explosion to account for the narrow lines in SN 1983K. However, at present, the explosive mass ejection by presupernovae is just a working hypothesis, especially since Woosley *et al.* (2002) recently questioned the reality of their explosive mass ejection mechanism. Thus, the study of signatures of the explosive mass ejection by presupernovae (high mass and energy of the CS envelope and young age) is of particular interest as evidence for as yet incomprehensible physical phe-

*E-mail: nchugai@inasan.rssi.ru

nomena in presupernovae on the eve of a SN IIn explosion.

It was already noted above that explosive mass ejection by presupernovae could take place in those SN IIn that show a high CS expansion velocity ($\sim 1000 \text{ km s}^{-1}$) and evidence of a high CS gas density in the form of CS subordinate hydrogen and metal absorption lines (Chugai *et al.* 2003). Apart from SN 1994W, several more SN IIn, including SN 1995G (Pastorello *et al.* 2002), belong to this type of supernovae. The latter supernova also has a peculiar light curve suggesting a significant role for the CS shock interaction in the supernova emission (Pastorello *et al.* 2002).

In this paper, we model the bolometric light curve of SN 1995G to extract information about the CS gas density. As will be clear below, our results allow us to determine the mass, energy, and age of the CS envelope and to give considerations about its origin. In Section 2, we briefly describe the model. In Section 3, we study the sensitivity of the model to parameters and demonstrate the uncertainty in choosing the parameters for SN 1997cy. In Section 4, we model the light curve of SN 1995G and determine the mass of the CS envelope and other parameters. The results and their relationship to the $H\alpha$ intensity and profile are discussed in Section 5.

This paper is essentially based on the photometry and spectra presented by Pastorello *et al.* (2002). Here, we took the Hubble constant to be $H_0 = 70 \text{ km s}^{-1} \text{ Mpc}^{-1}$.

2. THE MODEL

The model of the light curve used below was described previously (Chugai 2001). Here, we only briefly recall its essential properties. We are considering the expansion of a supernova in a CS envelope with given density and velocity distributions in the thin-shell approximation (Chevalier 1982a). We ignore the detailed structure of the interaction region, which consists of two shock waves, forward and reverse, with a density peak at the contact discontinuity. This structure can be described by a self-similar solution for a power-law density distribution of the supernova and CS gas in the adiabatic approximation with the CS gas velocity disregarded (Nadyozhin 1981, 1985; Chevalier 1982b). We are interested in the more general types of density distributions in the supernova and CS gas with a nonzero CS expansion velocity. In this case, the self-similar solution is inapplicable, and the dynamics of the thin shell should be calculated numerically.

The interaction of a supernova with its CS environment on a time scale longer than several days

depends weakly on the initial expansion stage. We assume the following: the interaction begins at the presupernova radius R_0 , the supernova expands freely ($v = r/t$), and its density distribution is a plateau with a power-law decrease in density outward ($\rho \propto v^{-9}$).

By numerically solving the equation of motion for the thin shell, we determine its radius $R(t)$ as well as the relative velocities of the supernova and CS gas flows. In combination with the gas densities, this allows us to calculate the kinetic luminosities of the forward and reverse shocks. These luminosities can be transformed into the X-ray luminosities of both shocks and eventually into the optical bolometric luminosities (Chugai 1992). The contribution of the luminosity supplied by the internal energy stored in the supernova during its explosion is calculated in an analytical approximation (Arnett 1980, 1982). In our model, the full light curve is a linear superposition of this luminosity and the interaction luminosity. This approach allows us to take into account the radiation of the initial internal energy at the early stage in a straightforward way.

To describe the CS gas density distribution, we specify the density ρ_0 at a radius of 10^{15} cm , or the density parameter $w = 4\pi r^2 \rho$ at this radius, and the index (s) in the power law ($\rho \propto r^{-s}$). The extent of the CS envelope is characterized by the outer radius R_b . With the mass (M) and energy (E) of the supernova envelope, we have five parameters; these are constrained by the light curve, the photospheric radius, the supernova expansion velocity, and the phase of the characteristic break in the light curve.

3. THE SENSITIVITY TO PARAMETERS AND SN 1997cy

The sensitivity of the model to parameter variations is demonstrated by models A1, A2, B, C, and D (Fig. 1) with their parameters presented in the table. Starting from the second column, the table gives the supernova mass (M), energy (E), the power-law index of the CS density distribution (s), the density parameter (w_0) and the density (ρ_0) at a radius of 10^{15} cm , the outer radius of the CS envelope (R_b), and the mass of the CS envelope (M_{cs}). The latter is the derivative of the density distribution. We take a CS velocity of 1000 km s^{-1} , a presupernova radius $R_0 = 1000 R_\odot$, and a ^{56}Ni mass of $0.003 M_\odot$ by analogy with the estimate for SN 1994W (Sollerman *et al.* 1998). Model A1 is taken as standard against which all the other models are compared. For all cases, Fig. 1 shows the bolometric light curves and the thin-shell velocities.

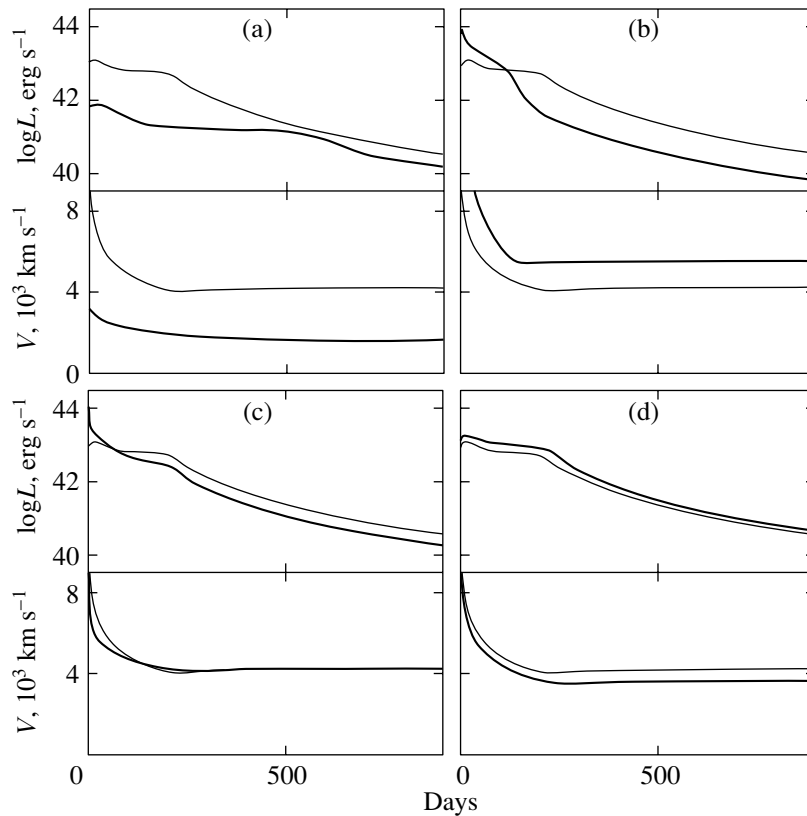


Fig. 1. Bolometric light curves and velocities of the thin shell for models A–D (table). Model A1 (thin line) is a template for models A2, B, C, D, which are shown in panels (a, b, c, and d), respectively.

We begin with a brief discussion of the general properties of the models. First, they all show a shoulder that reflects the overtaking of the CS shell boundary by the forward shock. Second, the luminosity is still high after that time. The source of this radiation is the inner shock, which is driven by the supersonic velocity jump between the outer supernova material and the thin shell. As the thin shell accelerates, the inner shock luminosity decreases. Note that the luminosity of the inner shock is lower in the case of a lower mass of the supernova envelope (model B). Finally, for most of the models, the contribution of the internal energy of the supernova to the luminosity is relatively small, except for model A2, which has a noticeable early bump during the first 50–100 days.

Let us consider the effects of parameter variations. The decrease in the supernova kinetic energy by an order of magnitude (model A2) reduces the early luminosity by more than an order of magnitude with a less pronounced luminosity decrease at the late epoch (Fig. 1a). The fivefold reduction in mass (model B) results in a substantially higher early luminosity due to the higher velocity of the outer shock (Fig. 1b). Still, model B shows a faster decay of the early luminosity because of the fast crossing of the CS envelope. Model C, with a steeper density distribution ($s = 2$)

for a similar mass of the CS shell gives, as expected, a higher early luminosity and faster decay (Fig. 1c). Model D, with twice as higher mass of the CS envelope, yields a higher luminosity and a lower velocity of the thin shell (Fig. 1d).

The above analysis implies that a combination of low mass and low energy can produce a fairly bright SN IIn phenomenon as a result of the efficient deceleration of the bulk of the supernova envelope. As an illustration of this assertion, let us consider the light curve of SN 1997cy (type IIn) studied by Turatto *et al.* (2000). In the paper cited, the proposed interaction model suggests an enormous supernova energy (3×10^{52} erg) and a large mass ($\sim 20M_{\odot}$). Although this model is plausible, we cannot rule out an alternative model with moderate energy and mass. This is demonstrated by models cy1 and cy2 (Fig. 2 and the table). The adopted velocity of the CS envelope is 10 km s^{-1} . Model cy1 with $M = 5M_{\odot}$ and $E = 2 \times 10^{51}$ erg provides satisfactory agreement with the data, while model cy2 with $M = 1.5M_{\odot}$ and $E = 10^{51}$ erg shows an even slightly better fit, because it better reproduces the luminosity drop at $t > 600$ days. The velocity of the thin shell is different in these models (Fig. 2), and this difference may be crucial in choosing

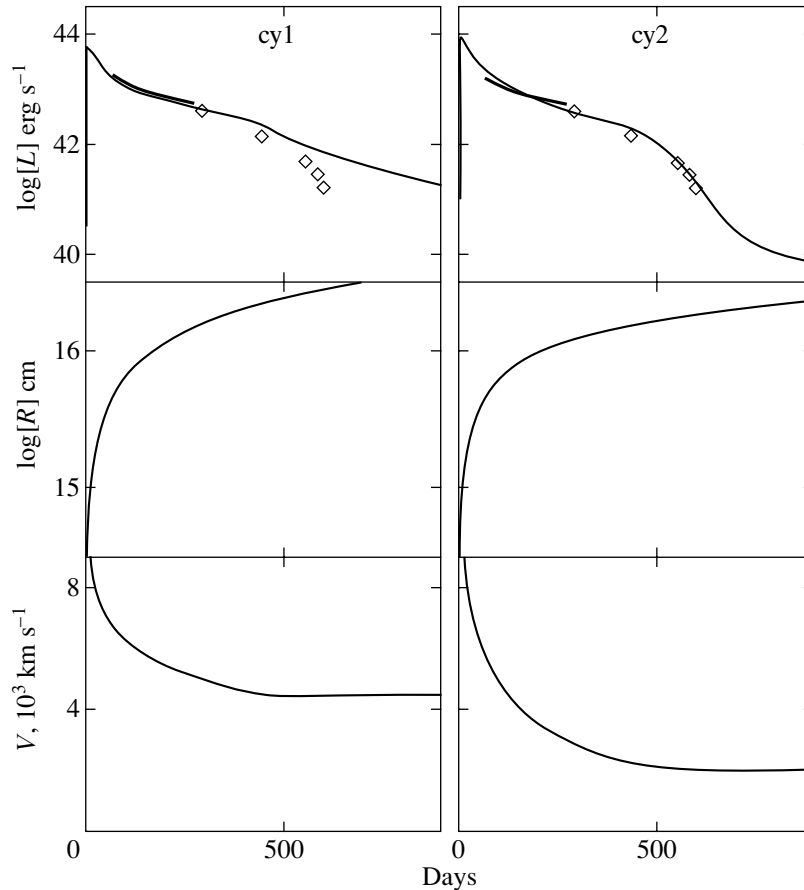


Fig. 2. Two models of the bolometric light curve for SN 1997cy (table). The observations (diamonds and the heavy line segment) were taken from Turatto *et al.* (2000). Modeling shows that the light curve can be reproduced for a moderate supernova energy.

between models based on the velocity information provided by the line profiles. Unfortunately, there is no straightforward procedure for determining the thin-shell velocity in SN 1997cy. Therefore, the uncertainty in choosing the mass and energy remains.

4. THE SN 1995G LIGHT CURVE AND THE MASS OF THE CS ENVELOPE

Let us briefly consider additional observational constraints imposed on the model apart from the bolometric light curve of SN 1995G. The energy distribution in the early spectra of SN 1995G provides estimates of the temperature and radius of the photosphere on days 2 and 36 (Pastorello *et al.* 2002). We believe that the photospheric radius at the early epoch is approximately equal to the radius of the thin shell. These arguments are based on the fact that the thin dense shell is optically opaque in the case of a very dense CS environment ($w \sim 10^{17} \text{ g cm}^{-1}$) for about one or two months (Chugai 2001). Thus, the first additional observational constraint on the model suggests that the early photospheric radius should be

approximately equal to the radius of the thin shell if the CS density is fairly high, i.e., $w \sim 10^{17} \text{ g cm}^{-1}$.

The next important constraint on the model is provided by the expansion velocity of the thin shell. Observational information about this velocity is contained in the line profiles, particularly in the maximum velocity of the broad component. Since Thomson scattering can contribute to the broad component at the early epoch (Chugai *et al.* 2003), to estimate the thin-shell velocity, we rely on the late nebular spectra of SN 1995G on days 265 and 561. In Fig. 3, the Fe II 5018 Å line is shown for both epochs (Pastorello *et al.* 2002). This line is free from blending, which makes it a reliable indicator of the broad-component velocity. The broad component is identified with the dense thin shell, which may be partially fragmented, at the boundary between the supernova and the CS gas as in SN 1994W (Chugai *et al.* 2003). The maximum velocity in the blue wing of the broad component is estimated by using the linear fitting of the line and continuum flux (Fig. 3). The derived maximum velocities are 3000 and 2700 km s⁻¹ on days 265 and

Model parameters

Model	M, M_{\odot}	$E, 10^{51}$ erg	s	$w_0, 10^{17}$ g cm $^{-1}$	$\rho_0, 10^{-15}$ g cm $^{-3}$	$R_b, 10^{16}$ cm	M_{cs}, M_{\odot}
A1	5	1	1	0.4	3.2	1	1
A2	5	0.1	1	0.4	3.2	1	1
B	1	1	1	0.4	3.2	1	1
C	5	1	2	2	16	1	1
D	5	1	1	0.8	6.4	1	2
cy1	5	2	1.8	1	8	2.3	1.8
cy2	1.5	1	1.3	1.1	9	1.7	4.1
G1	2	0.24	2	1.2	9.5	2.2	1.2
G2	10	0.6	2	1.1	8.7	2	1.1
G3	21	1	2	1.2	9.5	2	1.1

561, respectively, with a possible uncertainty of 10%. We attribute these velocities to the thin shell. Similar values (≈ 3000 km s $^{-1}$) are shown by the maximum velocity in the H α blue wing. However, in this case, Fe II emission lines may contribute to the blue-wing flux, which makes it difficult to estimate the maximum velocity.

The expansion velocity of the CS envelope estimated from narrow absorption lines is $u = 750$ km s $^{-1}$ (Pastorello *et al.* 2002). However, a slightly higher value of $u \approx 850$ km s $^{-1}$ is obtained from the infrared Ca II triplet emission lines (Pastorello *et al.* 2002, Fig. 10). Here, we adopt $u = 800$ km s $^{-1}$.

Finally, yet another constraint on the model is that after day 700, the light curve shows a more rapid decay, which can be interpreted as the result of the overtaking of the outer boundary of the CS envelope by the forward shock (Pastorello *et al.* 2002). This fact will be used to estimate the outer radius of the CS envelope.

Preliminary computations of a large set of models for SN 1995G reveal the following important feature: it turns out that within the empirical constraints, the model is insensitive to one of the two guiding supernova parameters, either mass or energy. Selecting the mass as the guiding parameter, we found that a fit is achievable for a wide range of masses. Two models with masses of $2M_{\odot}$ (model G1) and $10M_{\odot}$ (model G2), with other parameters given in the table, show an acceptable fit of the bolometric light curve, the photospheric radius, and thin-shell velocity (Fig. 4). Note that to achieve agreement with the photospheric radius at the first epoch, we added 20 days to the age of the supernova given by Pastorello *et al.* (2002). This means that the explosion of SN 1995G is assumed to have occurred 20 days earlier than the zero

point accepted in the cited paper. However, when some observational phase is mentioned in the text, we formally retain its day according to Pastorello *et al.* (2002). Models G1 and G2 confirm that the density and mass of the CS envelope do not depend on the adopted supernova mass (the table). The density at a radius of 10^{15} cm is $\approx 9 \times 10^{-15}$ g cm $^{-3}$, or, in terms of the hydrogen concentration for a normal abundance, $n \approx 4 \times 10^9$ cm $^{-3}$.

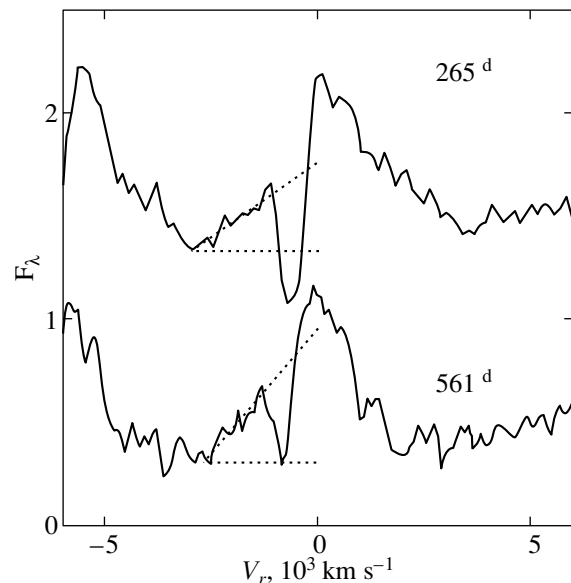


Fig. 3. The Fe II 5018 Å line in the SN 1995G spectra on days 265 and 561 (Pastorello *et al.* 2002). Both profiles reveal a narrow P Cyg component and a broad emission component. The latter is related to the dense shell at the supernova boundary. The dotted line indicates a fit to the blue part of the profile and to the continuum used to estimate the maximum velocity.

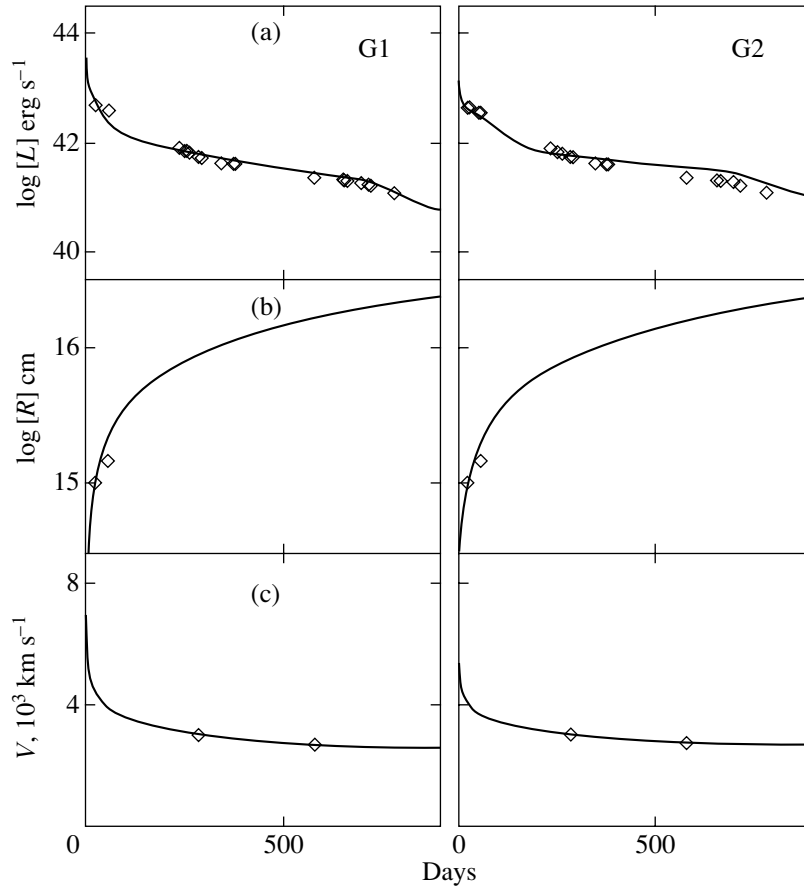


Fig. 4. Bolometric light curve of SN 1995G (upper panel), radius of the thin shell (middle), and velocity of the thin shell (lower panel) for two models G1 and G2, with different supernova masses (see table).

The fact that the CS gas density is independent of the adopted supernova mass has a simple explanation. For the high CS density required in the case of SN 1995G, both shock waves (forward and reverse) are essentially radiative for a long period (≈ 700 d), implying that for a given total radiated energy, the total dissipated kinetic energy in the shocks is constant. Since the forward shock dominates in the luminosity, the characteristic radiated energy must be $\sim 0.5M_{\text{CS}}(v-u)^2$. Given the observational constraints on the shell velocity (v) and the CS velocity (u), the total mass of the CS envelope must then be also constant in different models.

In both models, the kinetic energy is lower than the typical energy of core collapse supernovae (10^{51} erg). Although the question about the typical energy for SN IIIn is still open, it would be instructive to consider the case of a “standard” energy. Model G3 with energy $E = 10^{51}$ erg shows a satisfactory fit and again requires a similar CS shell density and mass given in Fig. 5 (table), thus confirming that these values are independent of the adopted supernova mass at least in the range $2-20 M_{\odot}$. Note that the latter assertion

can be reformulated in terms of the supernova energy as a guiding parameter. In that case, the derived CS density around SN 1995G is independent of the supernova energy, at least in the range $(0.24-1) \times 10^{51}$ erg.

The fact that the CS gas density depends weakly on the adopted supernova mass in the interaction model is of great importance in diagnosing the CS density around SN IIIn. In essence, the model of the bolometric light curve in combination with the velocity of the thin shell allows us to estimate of the CS density in the limit of a radiative forward shock wave. This technique was already used previously for SN 1987F under the assumption of the standard supernova energy (or mass) (Chugai 1992). It now becomes clear that in the limit of high CS density ($w \geq 10^{17}$ g cm $^{-1}$), the derived CS density is virtually independent of the adopted supernova mass, at least in the range $2 \leq M \leq 20 M_{\odot}$.

5. DISCUSSION

The CS gas density distribution found above has important implications for the interpretation of the

spectrum of SN 1995G. The similarity between the early spectra of SN 1995G and SN 1994W, in particular, the strong effect of Thomson scattering in the $H\alpha$ profile (Chugai *et al.* 2003), suggests that a substantial fraction of $H\alpha$ emission is radiated by the CS envelope. Is this picture consistent with the above CS density estimate?

On the second day (or day 22 with the explosion epoch adopted here), the $H\alpha$ luminosity of the CS envelope in the range $r_1 < r < r_2$ in our model ($\rho \propto r^{-2}$) is

$$L(H\alpha) = \frac{1}{4\pi r_1} \alpha_{32} h\nu_{23} (xXwN_A)^2 \left(1 - \frac{r_1}{r_2}\right), \quad (1)$$

where α_{32} is the effective recombination coefficient of the $H\alpha$ emission, $h\nu_{23}$ is the $H\alpha$ photon energy, x is the degree of ionization, X is the hydrogen mass fraction, and N_A is the Avogadro number. Substituting in Eq. (1) the values for day 2, more specifically, the inner radius r_1 equal to the radius of the photosphere 1.1×10^{15} cm (Pastorello *et al.* 2002), the outer radius $r_2 = R_b = 2 \times 10^{16}$ cm, $\alpha_{32} = 1.2 \times 10^{-13}$ cm³ s⁻¹ (for an electron temperature of 10^4 K), $w = 1.2 \times 10^{17}$ g cm⁻¹, we obtain $L(H\alpha) = 6.2 \times 10^{40} x^2$ erg s⁻¹ by assuming that $X = 0.7$. On the other hand, the observed $H\alpha$ luminosity on day 2 is $L(H\alpha) = 6.3 \times 10^{40}$ erg s⁻¹ (Pastorello *et al.* 2002). By analogy with SN 1994W, we assume that the contribution of the CS component in $H\alpha$ is at least half the total line luminosity (Chugai *et al.* 2003). Comparing the model and observed luminosity of the CS component, we thus conclude that both values agree if the average degree of ionization of the model CS envelope is $0.7 < x \leq 1$.

The optical depth of the CS envelope to Thomson scattering for the same epoch is $\tau_T = k_T w x / 4\pi r_1 \approx 2.6x$, which gives $1.8 < \tau_T < 2.6$ for the above range of the ionization degree. The presence of a strong red wing in $H\alpha$ on day 2 (Pastorello *et al.* 2002, Fig. 10) suggests significant Thomson scattering, so one expects $\tau_T > 1$. Moreover, the close similarity between this profile and the $H\alpha$ profile in SN 1994W on day 30 (Chugai *et al.* 2003) implies that the optical depth of the CS envelope in SN 1995G may be as large as $\tau_T \sim 2$, which is consistent with the above range of the Thomson optical depth.

To summarize, the density of the CS envelope derived from the interaction model agrees with both the $H\alpha$ line luminosity and with the presence of strong effects of Thomson scattering in this line.

In principle, analysis of CS absorption lines could provide additional information about the CS density. However, this approach would require a rather complex model of the ionization and excitation in the CS envelope. Simple considerations based, for instance,

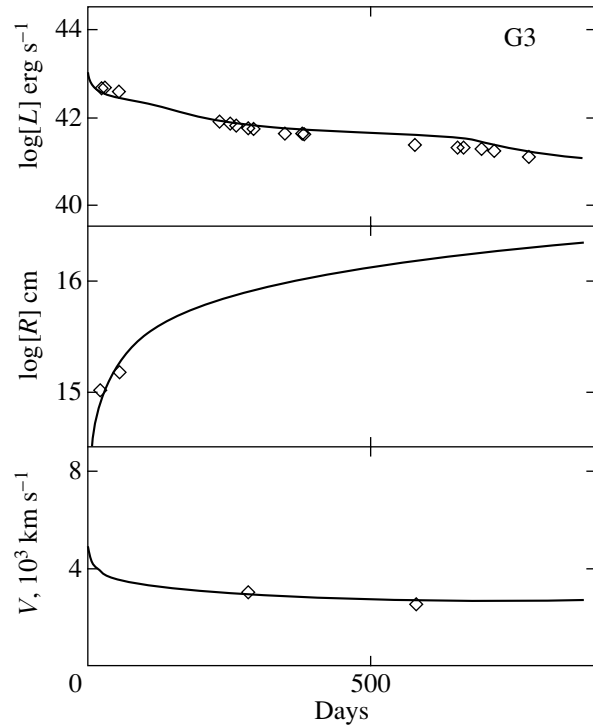


Fig. 5. The same as Fig. 4 but for model G3.

on Fe II absorption give a rough lower limit (Sollerman *et al.* 1998). The requirement that an absorption line with an optical depth τ be present in the spectrum is $\tau > 1$. For an envelope of size r with a velocity dispersion on the line of sight of the order of the expansion velocity v (greater than the thermal velocity), the latter condition is

$$\tau \approx \sigma(\nu)n_1r \approx \sigma_0 n_1 r \lambda_{12}/v > 1, \quad (2)$$

where $\sigma_0 = (\pi e^2/m_e c) f_{12} = 0.0265$ cm² s⁻¹ is the frequency-integrated absorption cross section $\sigma(\nu)$, f_{12} is the oscillator strength, n_1 is the concentration at the lower transition level, and λ_{12} is the wavelength. For the Fe II 5018 Å absorption ($f_{12} = 0.01$), assuming that the excitation temperature of the lower level on day 2 is equal to the photospheric temperature of 8800 K (Pastorello *et al.* 2002) and taking r to be equal to the photospheric radius (1.1×10^{15} cm), we obtain a lower limit for the hydrogen concentration (assuming a solar Fe abundance $n > 3 \times 10^7$ cm⁻³), in qualitative agreement with the density found from the light-curve analysis.

The outer boundary of the CS envelope (2×10^{16} cm) combined with the CS expansion velocity 800 km s⁻¹ implies an age for the CS envelope of $t_{cs} \approx 8$ yr, which is close to the estimate of the time at which intense mass loss begins (≈ 12 yr before the supernova explosion) found by Pastorello *et al.* (2002). The mass of the CS envelope ($1M_\odot$) combined with

the age thus suggests an average mass loss rate $\dot{M} \sim 0.1 M_{\odot} \text{ yr}^{-1}$, an enormous value. The estimated total kinetic energy of the CS envelope is $E_{\text{CS}} \approx 6 \times 10^{48}$ erg, and the average kinetic luminosity of the mass loss is then $E_{\text{CS}}/t_{\text{CS}} \approx 2.4 \times 10^{40}$ erg s⁻¹. This value is almost two orders of magnitude higher than the typical radiative luminosity of a massive presupernova ($\approx 10^5 L_{\odot}$). Thus, the mass loss certainly cannot be attributed to the superwind.

Therefore, we suggest that the mass ejection in the SN 1995G presupernova was triggered by some powerful energy release on the hydrodynamic time scale approximately eight years before the main supernova explosion. Indeed, we reproduce here the arguments used in the case of SN 1994W to conclude that the CS envelope around SN 1994W was lost as a result of an explosive event ~ 1.5 yr before the supernova explosion (Chugai *et al.* 2003). It was assumed there that the explosive mass ejection was triggered by a flash of Ne nuclear burning in a degenerate O/Ne/Mg core. This assumption follows the original hypothesis of Weaver and Woosley (1979) concerning the behavior of presupernovae with initial masses of $\approx 11 M_{\odot}$. A similar possibility may also occur in the case of SN 1995G. Note that the age of the CS envelope around SN 1995G (~ 8 yr) lies within the range of the phase for the Ne burning in massive stellar cores 1–10 years before the supernova explosion (Heger 1998).

If the initial mass of the SN 1995G presupernova was actually close to $11 M_{\odot}$, then, given a neutron-star mass of $1.4 M_{\odot}$, the mass of the supernova ejecta cannot exceed $10 M_{\odot}$. In that case, our interaction model predicts a supernova kinetic energy of $\leq 6 \times 10^{50}$ erg (the table). This value is lower than the value of 1.5×10^{51} erg adopted for SN 1994W (Chugai *et al.* 2003). It may well be that the differences between the supernova energies and the ages of the CS shells around SN 1995G and SN 1994W (8 and 4 yr, respectively) are presumably related to slight differences between their initial masses or evolution histories.

If the mass ejection of the SN 1995G presupernova was explosive in nature, then the CS envelope expansion regime must be close to a free expansion ($u \propto r$) law, at least in the outer layers. In this respect, the increase in the velocity derived from CS Fe II absorption lines between days 330 and 560 (Pastorello *et al.* 2002) is in qualitative agreement with the possible free expansion CS kinematics.

The envelope ejection with a mass of $\sim 1 M_{\odot}$ and a kinetic energy of $\sim 6 \times 10^{48}$ erg must be accompanied by an optical flash eight years before the explosion of SN 1995G. In a simple analytical model of the light

curve (Chugai 1991), assuming that the presupernova radius is $100 < R_0 < 1000 R_{\odot}$, we estimated the absolute magnitude of this event at maximum as $-12.5 > M_V > -13.5$ mag with a duration of the light curve of 80–120 days. For a distance of 63 Mpc, the apparent magnitude of the maximum for this flash is $21.8 > V > 20.8$ mag. The only available image of the host galaxy NGC1643 close to the assumed time of the presupernova flash is a UK Schmidt plate taken December 12, 1982, 13 years before the SN 1995G explosion. Therefore, this image does not constrain the presupernova flash history. Inspection of this plate reveals no objects brighter than 20.5 mag in the *J* band.

6. CONCLUSIONS

We modeled the bolometric light curve and expansion dynamics of SN 1995G in a dense CS environment. As a result, we obtained the density and mass of the CS envelope, which do not depend on the adopted mass of the supernova envelope. The derived mass of the CS envelope combined with the CS gas velocity leads us to conclude that the CS envelope was ejected through an energetic hydrodynamic process eight years before the explosion of SN 1995G. This mass ejection may have been triggered by a powerful thermonuclear flash in the degenerate O/Ne/Mg core of the presupernova, by analogy with the earlier hypothesis proposed for SN 1994W.

ACKNOWLEDGEMENTS

We thank the UK Schmidt Unit for providing the scanned images of Schmidt plates around NGC1643. The studies by N. Chugai were supported by the Russian Foundation for Basic Research (project no. 01-02-16295).

REFERENCES

1. W. D. Arnett, *Astrophys. J.* **237**, 541 (1980).
2. W. D. Arnett, *Supernovae: A Survey of Current Research*, Ed. by M. J. Rees and R. J. Stoneham (Reidel, 1982), p. 221.
3. R. A. Chevalier, *Astrophys. J.* **259**, 302 (1982a).
4. R. A. Chevalier, *Astrophys. J.* **258**, 790 (1982b).
5. N. N. Chugai, *Pis'ma Astron. Zh.* **16**, 1066 (1990) [*Sov. Astron. Lett.* **16**, 457 (1990)].
6. N. N. Chugai, *Pis'ma Astron. Zh.* **17**, 495 (1991) [*Sov. Astron. Lett.* **17**, 400 (1991)].
7. N. N. Chugai, *Astron. Zh.* **69**, 125 (1992) [*Sov. Astron.* **36**, 63 (1992)].
8. N. N. Chugai, *Mon. Not. R. Astron. Soc.* **326**, 1448 (2001).
9. N. N. Chugai, S. I. Blinnikov, P. Lundqvist, *et al.*, *Mon. Not. R. Astron. Soc.* (2003, in press).

10. E. K. Grasberg and D. K. Nadyozhin, *Pis'ma Astron. Zh.* **12**, 168 (1986) [*Sov. Astron. Lett.* **12**, 68 (1986)].
11. A. Heger, *The Presupernova Evolution of Rotating Massive Stars*, *Ph. D. Thesis*, MPA, 1120 (1998).
12. D. K. Nadyozhin, Preprint No. 1 (Inst. Theor. Experiment. Phys., Moscow, 1981).
13. D. K. Nadyozhin, *Astrophys. Space Sci.* **112**, 225 (1985).
14. A. Pastorello, M. Turatto, S. Benetti, *et al.*, *Mon. Not. R. Astron. Soc.* **333**, 27 (2002).
15. I. Salamanca, R. Cid-Fernandes, G. Tenorio-Tagle, *et al.*, *Mon. Not. R. Astron. Soc.* **300**, L17 (1998).
16. E. Schlegel, *Mon. Not. R. Astron. Soc.* **244**, 269 (1990).
17. J. Sollerman, R. J. Cumming, and P. Lundqvist, *Astrophys. J.* **493**, 933 (1998).
18. M. Turatto, T. Suzuki, P. Mazzali, *et al.*, *Astrophys. J.* **534**, L57 (2000).
19. T. A. Weaver and S. E. Woosley, *Bull. Am. Astron. Soc.* **11**, 724 (1979).
20. S. E. Woosley, A. Heger, and T. A. Weaver, *Rev. Mod. Phys.* **74**, 1015 (2002).

Translated by N. Chugai

Diffusive Propagation of Fast Particles in the Presence of a Moving Shock Wave

I. S. Petukhov*, S. I. Petukhov, S. A. Starodubtsev, and V. E. Timofeev

*Yu.G. Shafer Institute of Cosmophysical Research and Aeronomy, Siberian Branch,
Russian Academy of Sciences, pr. Lenina 31, Yakutsk, 677891 Russia*

Received May 6, 2003

Abstract—Based on an analytical model, we determined the temporal dynamics of the spectral shape and spatial distribution of the particles that were impulsively (in time) injected with a specified spectrum in the vicinity of a moving plane shock front. We obtained a condition to determine the influence of the shock front on the particle propagation, where the spatial diffusion coefficient of the particles plays a major role. Diffusive shock acceleration is shown to strongly affect low-energy particles (the intensity maximum coincides spatially with the shock front; hard and soft spectral regions are formed in the spectrum) and weakly affect high-energy particles (the time at which the intensity reaches its maximum is well ahead of the shock arrival time; the spectral shape does not change). In events accompanied by a significant increase in the turbulence level, the influence of the shock front on high-energy particles can change from weak to strong. This change shows up in the spatial distribution and spectral shape of the particles. The dynamics of the particle intensity, calculated with the diffusion coefficients that were determined in accordance with the quasi-linear theory for measured turbulence levels, qualitatively corresponds to the observed solar energetic-particle intensity. © 2003 MAIK “Nauka/Interperiodica”.

Key words: *cosmic rays, nonthermal radiation, solar energetic particles, shock waves, diffusive shock acceleration.*

INTRODUCTION

Solar energetic particles (SEPs) in gradual events are generated by shock waves (see, e.g., Reames (1999) and references therein). The SEP generation region is mainly bounded by the solar corona, as suggested by the fluxes of protons with energies from 470 MeV to 21 GeV whose maximum occurs at the instant the shock wave in the solar atmosphere reaches heights of $5\text{--}10R_{\odot}$ (Kahler 1994). This finding is also confirmed by the following phenomenon commonly observed in interplanetary space: the time at which the intensity of SEPs with kinetic energies above 10 MeV reaches its maximum is well ahead of the shock arrival time. Changes in the SEP acceleration efficiency reflect the spatial dependence of the shock intensity and the background Alfvén turbulence level—the main factors of the diffusive shock acceleration mechanism, which are at a maximum near the Sun and decrease with increasing heliocentric distance (Denskat and Neubauer 1982). Model calculations of the diffusive shock acceleration of particles under typical conditions of the solar corona indicate that the time of shock passage through the

solar atmosphere is long enough for the particle spectrum that corresponds to the observed SEP parameters to be formed (Berezhko *et al.* 2001a, 2001b).

The interaction of charged particles (which can be superthermal solar-wind plasma ions, SEPs left in interplanetary space from preceding perturbations, or SEPs accelerated by the same shock in the solar corona) with an interplanetary shock front can give rise to new populations of particles. Particle beams with a soft spectrum can emerge in the segment of the shock front with a quasi-perpendicular magnetic field due to drift acceleration (see, e.g., Decker 1981). A spectrum of the accelerated particles (ESP events) can be formed in the quasi-parallel segment of the shock front through diffusive shock acceleration (see, e.g., Lee 1983). The relative contribution from each of the above sources to the new populations of particles in specific events is determined by the amplitude of the injected-particle flux, its energy and time dependences, and the Alfvén turbulence level. For example, the calculations based on the self-consistent stationary (Lee 1983) and nonstationary (Berezhko *et al.* 1998) theories of the diffusive shock acceleration of solar-wind protons and the generation of Alfvén turbulence are in satisfactory agreement with the

*E-mail: petukhov@ikfia.ysn.ru

measurements (Kennel *et al.* 1986; Berezhko *et al.* 1998).

Recently, a black-box model has been used to describe the SEP propagation in interplanetary space in the presence of a shock wave. In this model, the complex processes of particle interaction with the shock front and their injection from the perturbation region are replaced with a fictitious source that lies at the front and supplies particles to the preshock region (Kallenroude and Wibberenz 1997; Lario *et al.* 1998; Ng *et al.* 1999). The approach developed is useful in statistically analyzing events and allows the typical time profiles of the SEP intensity and anisotropy to be determined for the period preceding the arrival of a perturbation. This information is valuable for prediction purposes, because it allows the SEP impact limits to be determined under various conditions (Lario *et al.* 1999). A drawback of the method, as well as all of the black-box models, is the difficulty of using the parameters of the source to study the contribution of various processes to the formation of the observed SEP intensity and anisotropy.

Lee and Ryan (1986) used a different approach to analyzing the generation of SEPs in gradual events. A study of the analytical solution to the diffusive transport equation for the chosen law of shock motion and diffusion coefficients indicates that: (1) in the time of shock passage through the solar corona (~ 100 min), the maximum energy in the accelerated-particle spectrum reaches 0.1–1 GeV; (2) in interplanetary space, the maximum energy changes only slightly; and (3) the computed time profiles of the SEP intensity for the Earth's orbit are similar to its observed time profiles. Thus, the results obtained by Lee and Ryan (1986) confirm the close relationship between the diffusive shock acceleration of particles and SEP events.

Toptygin (1983) also calculated an analytical model that described the temporal dynamics of the spectrum for the particles that were accelerated by a plane shock wave. Note that the solutions obtained are qualitatively similar. The quantitative difference between the solutions is attributable to the different geometries of space and to the adopted law of shock motion and particle diffusion coefficients.

A drawback of the two models is that the particle diffusion coefficients do not depend on energy.

As a continuation of previous studies, we analyze here the temporal dynamics of the particle spectrum in the presence of a plane shock wave for energy-dependent and time-varying diffusion coefficients. The results are important for studying the effects of an interplanetary shock front on the properties of the SEPs that are generally recorded at the Earth's orbit and, thus, for determining the properties of the SEPs being formed in the solar atmosphere.

THE MODEL

A SEP event from the formation of a shock wave to its arrival at the Earth's orbit can be arbitrarily divided into two stages: the first stage (~ 1 h in duration) is the SEP generation in the solar corona; the second stage (~ 1 day in duration) is the SEP propagation in interplanetary space in the presence of a shock wave. When considering the second stage of the event, to which we restrict our analysis here, we assume that it begins with the injection of particles whose spectrum formed during the first stage.

Let us determine the phase-space distribution of fast charged particles for a given particle flux injected continuously (in time), starting from a time t_0 to a plane shock front that moves in unbounded space. To solve the problem, we choose a coordinate system whose origin coincides with the traveling shock front and whose x axis is directed opposite to the shock velocity. The solution of the transport equation in the diffusion approximation

$$\frac{\partial f_i}{\partial t} = k_i \frac{\partial^2 f_i}{\partial x^2} - u_i \frac{\partial f_i}{\partial x} \quad (1)$$

with zero initial and boundary conditions for $x \rightarrow \pm\infty$ and conditions for joining the solutions at the shock front defines the particle distribution in the presence of a shock wave (for more detail, see, e.g., Berezhko *et al.* 1988). Here, f_i is the isotropic part of the particle distribution function; p is the particle momentum; $u_1 = V_s - w$ and $u_2 = u_1/\sigma$ are the flow velocities in the chosen coordinate system; k_i is the particle diffusion coefficient; V_s and w are the shock and flow velocities, respectively, which are assumed to be constant; and σ is the gas compression ratio at the shock front. The subscripts 1 and 2 denote the functions and parameters pertaining to the preshock ($x < 0$) and postshock ($x > 0$) regions, respectively.

The general solution of the problem in space with a plane geometry and a dependence of the particle diffusion coefficients only on the momentum can be represented as two analytical relations: (1) the particle distribution function at the shock front that depends on the injected particle flux and (2) the particle distribution function in space that depends on the particle distribution function at the front. Using the method of generations (see Section 16.3 in the monograph by Berezhko *et al.* 1988), we can write the particle distribution function at the front $f_0(p, t)$ as

$$f_0(p, t) = \frac{3\sigma}{u_1(\sigma - 1)} \int_{p_{\min}}^p \frac{1}{4\pi p'^3} \left(\frac{p}{p'}\right)^{-q} \quad (2)$$

$$\times \frac{t_k^{3/2}}{\sqrt{2\pi d_k^2}} dp' \int_{t_0}^t (t - t')^{-3/2} \exp \left[\frac{t_k^2}{d_k^2} - \frac{t_k(t - t')}{2d_k^2} \right]$$

$$-\frac{t_k^3}{2d_k^2(t-t')}] J_{\text{inj}}(p', t') dt',$$

where $q = 3\sigma/(\sigma - 1)$; J_{inj} is the injected-particle flux density and the following notation is used:

$$t_k = \frac{3\sigma}{u_1^2(\sigma - 1)} \int_{p'}^p (\kappa_1(p'') + \sigma k_2(p'')) \frac{dp''}{p''}$$

is the mean time and

$$d_k^2 = \frac{6\sigma}{u_1^4(\sigma - 1)} \int_{p'}^p (\kappa_1^2(p'') + \sigma^3 k_2^2(p'')) \frac{dp''}{p''}$$

is the variance. In writing expression (2), we took into account the fact that the injected-particle spectrum is bounded from low momenta by p_{min} .

The particle distribution function $f_i(x, p, t)$ in the preshock and postshock regions is defined by the solution of Eq. (1) under zero initial and boundary conditions for $x \rightarrow \pm\infty$ and the boundary condition $f(x=0, p, t) = f_0(p, t)$. For the model adopted, this function can be represented as a convolution with the standard Green function of Eq. (1):

$$f_i(x, p, t) = \frac{(-1)^i x}{\sqrt{4\pi\kappa_i}} \exp\left[\frac{u_i x}{2\kappa_i}\right] \int_{t_0}^t (t-t')^{-3/2} \quad (3)$$

$$\times \exp\left[-\frac{u_i^2(t-t')}{4\kappa_i} - \frac{x^2}{4\kappa_i(t-t')}\right] f_0(p, t') dt',$$

where x is the distance from the front.

For impulsive (in time) particle injection,

$$J_{\text{inj}}(p', t') = N_{\text{inj}}(p') \delta(t' - t_0),$$

expression (2) takes the form

$$f_0(p, t) = \frac{3\sigma}{u_1(\sigma - 1)} \int_{p_{\text{min}}}^p \frac{N_{\text{inj}}(p')}{4\pi p'^3} \left(\frac{p}{p'}\right)^{-q} \quad (4)$$

$$\times \frac{t_k^{3/2}}{\sqrt{2\pi d_k^2 t^3}} \exp\left[\frac{t_k^2}{d_k^2} - \frac{t_k t}{2d_k^2} - \frac{t_k^3}{2d_k^2 t}\right] dp',$$

where $N_{\text{inj}}(p')$ is the differential spectrum of the injected particles per unit front area, and $\delta(t' - t_0)$ is the delta function.

For the injection of a monoenergetic particle beam and constant diffusion coefficients related by $k_1/k_2 = \sigma^2$, solution (4) is identical to the solution obtained by Topygin (1983).

Relations (3) and (4) define the dynamics of the particle distribution function in space and at the shock front, respectively, in events with time-independent diffusion coefficients.

It is well known from direct measurements (Wanner and Wibberenz 1993; Starodubtsev 2000) and theoretical analyses (Ng and Reames 1994) that sufficiently intense SEP fluxes can themselves change the turbulence level of MHD waves during an event. Based on numerical models, Ng *et al.* (1999) studied the self-consistent dynamics of the SEP ion flux and turbulence.

We can evaluate the possible manifestations of changes in the diffusion coefficients during an event in the dynamics of the particle flux in terms of a simplified analytical model. Let us assume that the particles propagate in two stages: at the first stage, the particles impulsively injected at a time t_0 propagate in a time interval (t_0, t_*) with the same diffusion coefficients; at the second stage, the diffusion coefficients abruptly change at a time t_* in the entire space, and the particle propagation continues in a time interval (t_*, t) with new diffusion coefficients. Such a simplification in analyzing SEP events can be used because, as follows from measurements, the condition $\Gamma t \gg 1$, where Γ is the wave growth rate and t is the duration of the SEP event, is satisfied for typical conditions in interplanetary space.

In this approach, the first stage is described by relations (3) and (4) as above. When considering the second stage, it is convenient to separate the particles into two populations according to the following criterion: whether or not they reached the shock front after t_* . The spatial distribution of the population-1 particles (i.e., those which have not yet reached the shock front) in each of the half-spaces is defined by the solution of the transport equation (1) for zero boundary conditions and a given initial (for the second stage) distribution $f_i(x, p, t_*)$

$$f_i(x, p, t) = \frac{1}{\sqrt{4\pi k_i(t-t_*)}} \exp\left[-\frac{u_i^2(t-t_*)}{4k_i}\right] \quad (5)$$

$$\times \int_a^b f(x', p, t_*) \exp\left[\frac{u_i(x-x')}{2k_i}\right]$$

$$\times \left(\exp\left[-\frac{(x'-x)^2}{4k_i(t-t_*)}\right] - \exp\left[-\frac{(x'+x)^2}{4k_i(t-t_*)}\right]\right) dx',$$

where $f_i(x, p, t_*)$ is the spatial particle distribution in the corresponding half-space at the end of the first stage

$$a = \begin{cases} -\infty, & i = 1 \\ 0, & i = 2, \end{cases} \quad b = \begin{cases} 0, & i = 1 \\ \infty, & i = 2. \end{cases}$$

The population-1 particle flux incident on the shock front is specified by distribution (5) and is

$$J_{\text{inj},i} = 4\pi p^2 k_i \left. \frac{\partial f_i}{\partial x} \right|_{x=0} = \frac{4\pi p^2}{\sqrt{4\pi k_i(t-t_*)^3}} \quad (6)$$

$$\begin{aligned} &\times \exp \left[-\frac{u_i^2(t-t_*)}{4k_i} \right] \int_a^b (-1)^i x' f_i(x', p, t_*) \\ &\times \exp \left[-\frac{u_i x'}{2k_i} \right] \exp \left[-\frac{x'^2}{4k_i(t-t_*)} \right] dx'. \end{aligned}$$

Thus, at the second stage, particles of both populations are present in each of the half-spaces, with the spatial distribution of the population-1 and population-2 particles being described by relations (5) and (2), (3), respectively. In this case, in the internal integration of expression (2), the injected particle flux is the sum of the fluxes defined by expressions (6) for the integration range (t_*, t) .

RESULTS AND DISCUSSION

In our illustrative calculations shown in Figs. 1 and 2, we used $w = 400 \text{ km s}^{-1}$, $V_s = 700 \text{ km s}^{-1}$, and $\sigma = 3.5$. We also assumed that the impulsive injection of protons with the following differential power-law momentum spectrum took place at time t_0 , which was taken as zero:

$$N_{\text{inj}} = N_0(p/mc)^{-5} H(p - p_{\text{min}}),$$

where N_0 is the normalization constant, H is the Heaviside function, and $p_{\text{min}} = 0.014mc$ ($\varepsilon_{\text{min}} = 92 \text{ keV}$). The preshock diffusion coefficient was taken in the form $k_1 = k_{10}\varepsilon/1 \text{ MeV (cm}^2 \text{ s}^{-1})$. Figure 1 shows the results of our calculations for three values of the diffusion coefficient: (a, b) $k_{10} = 4.2 \times 10^{19}$, (c, d) $k_{10} = 2.1 \times 10^{20}$, (e, f) $k_{10} = 1.1 \times 10^{21}$. The postshock diffusion coefficient was taken in the form $k_2 = k_1/10$ in all of our calculations.

In Figs. 1a, 1c, and 1e, the proton intensity $J = p^2 f$ at the Earth’s orbit is plotted against time for six energies: 1—0.6, 2—1.6, 3—3.8, 4—9.3, 5—22.7, and 6—55.2 MeV. In Figs. 1b, 1d, and 1f, the proton distribution function at the shock front $f_0(p, t)$ calculated using relation (4) is plotted against kinetic energy (in MeV). The proton distribution function at the shock front in Figs. 1b, 1d, and 1f is shown for three times: 1— $t = 0.05t_e$, 2— $t = 0.5t_e$, and 3— $t = t_e$, where $t_e = r_e/V_s$ is the time of shock arrival at the Earth’s orbit, and for the values of $t_e = 59.5 \text{ h}$, $r_e = 1 \text{ AU}$.

As we see from the results presented in Fig. 1, two variants of intensity dynamics are possible for particles of different energies: in the first variant, the intensity peaks at the shock arrival time (curves 1–4 in Fig 1a; curves 1 and 2 in Fig. 1c); in the second variant, the intensity after its rapid increase is either nearly constant or decreases until the arrival of the shock front (the remaining curves in Figs. 1a, 1c, and 1e).

The results presented in Figs. 1b, 1d, and 1f show that the particle interaction with the shock front causes the spectral shape to change in the energy range only in the first variant of intensity dynamics. Note the different patterns of change in the spectral shape: the spectrum is harder than the injected-particle spectrum at low energies (the region between marks A and B in Fig. 1b) and softer at high energies (the region between marks B and C).

The boundary of the energy range in the spectrum of the injected particles that underwent a significant change through their interaction with the shock front is defined by the relation

$$t = t_k - \sqrt{2d_k^2}, \tag{7}$$

which is a corollary of the limit theorem in the probability theory for our problem (for more detail, see Berezhko *et al.* 1988). Here, t is the duration of the process; t_k and d_k^2 are the mean time it takes for a particle to execute k cycles and the variance, respectively. Using the above expressions for the mean time and the variance (after formula (2)), as well as the values of the quantities from (7) adopted in the calculation shown in Fig. 1b, we obtain for $t = t_e$

$$\begin{aligned} \varepsilon_*/1 \text{ MeV} &= \frac{r_e u_1^2 / V_s k_{10}}{\frac{3\sigma(1+0.1\sigma)}{2(\sigma-1)} - \sqrt{\frac{3\sigma(1+0.01\sigma^3)}{\sigma-1}}} \\ &\approx 2.6 \frac{r_e u_1^2}{V_s k_{10}} \approx 12. \end{aligned} \tag{8}$$

In Fig. 1b, the above energy range highlighted by a horizontal line with an arrow is in satisfactory agreement with the calculations. It is easy to verify that relation (7) and the consequent relations similar to (8) are also in reasonable agreement with all of the calculations shown in Figs. 1b, 1d, and 1f.

The efficiency of the particle interaction with a plane shock front (the diffusive shock acceleration efficiency) is known to be determined by the acceleration time $t_{\text{acc}} \approx k_1/u_1^2$ (Berezhko *et al.* 1988). After a lapse of time t , the shock wave will significantly affect those particles for which the condition $t_{\text{acc}} < t$ or, at $t = t_e$, $u_1^2 r_e / k_1 V_s \geq 1$ is satisfied, where the boundary value of the dimensionless combination of parameters, to within a numerical factor, matches expression (8).

Our calculations presented in Fig. 2 illustrate the influence of changes in the diffusion coefficients on the intensity dynamics and the particle distribution function at the shock front. The corresponding curves in Figs. 1 and 2 coincide until the time $t_* = 0.5t_e =$

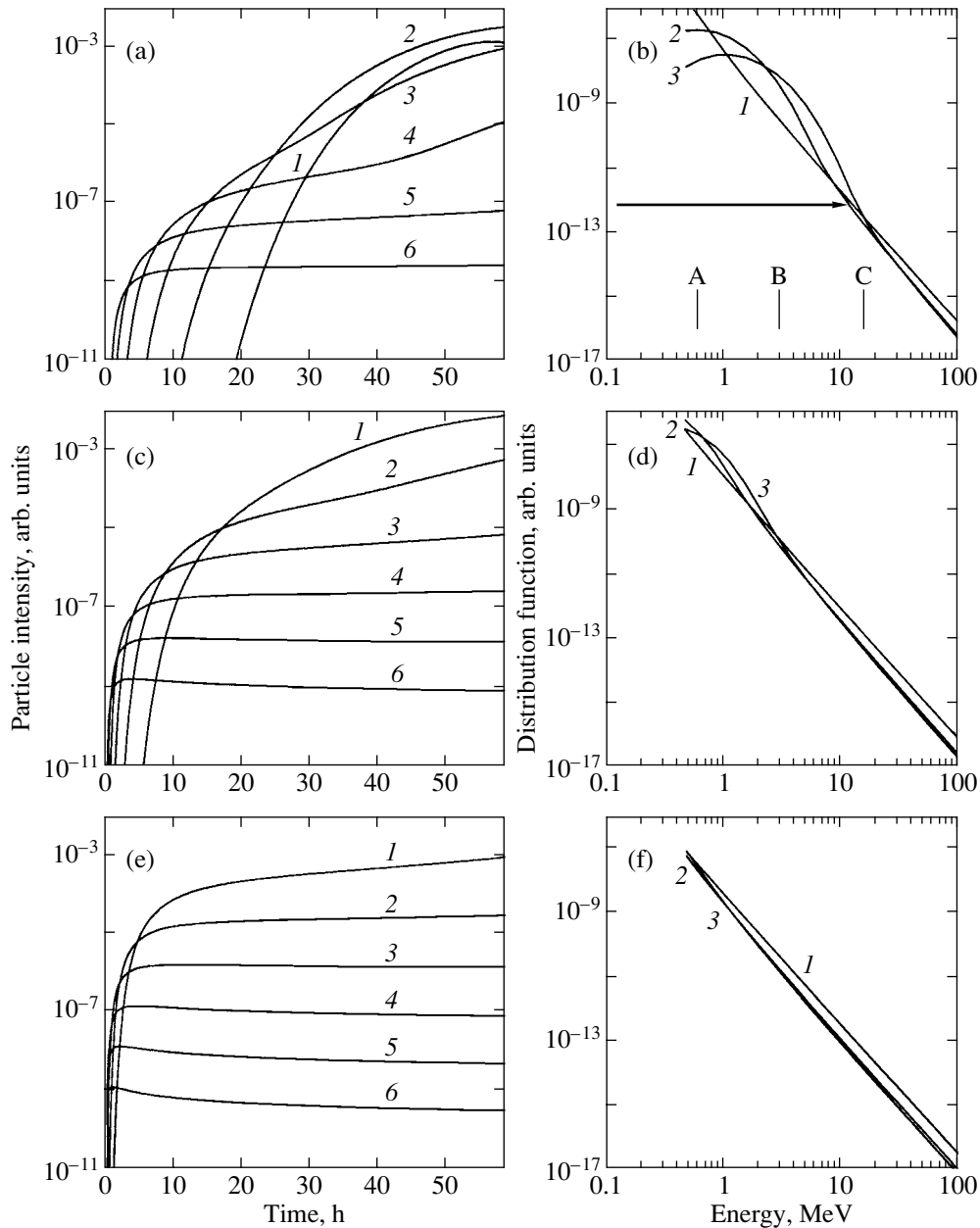


Fig. 1. Particle intensity versus time for six energies (1–6 in a, c, e) at a fixed point of the preshock region and the particle distribution function at the shock front versus energy for three times (1–3 in b, d, f). The chosen times are: 1— injection time; 2—30 h after injection; 3—60 h after injection—for the adopted parameters, coincides with the arrival time of the shock front to the fixed point. The particle diffusion coefficient is specified as $k_1 = k_{10}(\varepsilon/1\text{MeV cm}^2 \text{ s}^{-1}$, where: $k_{10} = 4.2 \times 10^{19}$ (a, b); $k_{10} = 2.1 \times 10^{20}$ (c, d); $k_{10} = 1.1 \times 10^{21}$ (e, f).

30 h; the subsequent difference in dynamics is attributable to a tenfold decrease in the diffusion coefficients. Comparison indicates that changes in the diffusion coefficients have different effects on the intensity dynamics. This difference results from the formation of hard and soft spectral regions in the injected-particle spectrum (curve 2 in Fig. 2b). Changes in the diffusion coefficients weakly affect the dynamics of particles with energies in the hard spectral region

(curves 1 and 2 in Fig. 2a in comparison with similar curves in Fig. 1a). At the same time, the intensity dynamics significantly changes for particles with energies in the soft spectral region (curves 3–6 in Fig. 2a, curves 2–4 in Fig. 2c, and curve 2 in Fig. 2e in comparison with similar curves in Fig. 1). The weak influence of changes in the diffusion coefficients on the behavior of curves 1 in Figs. 2c and 2e stems from

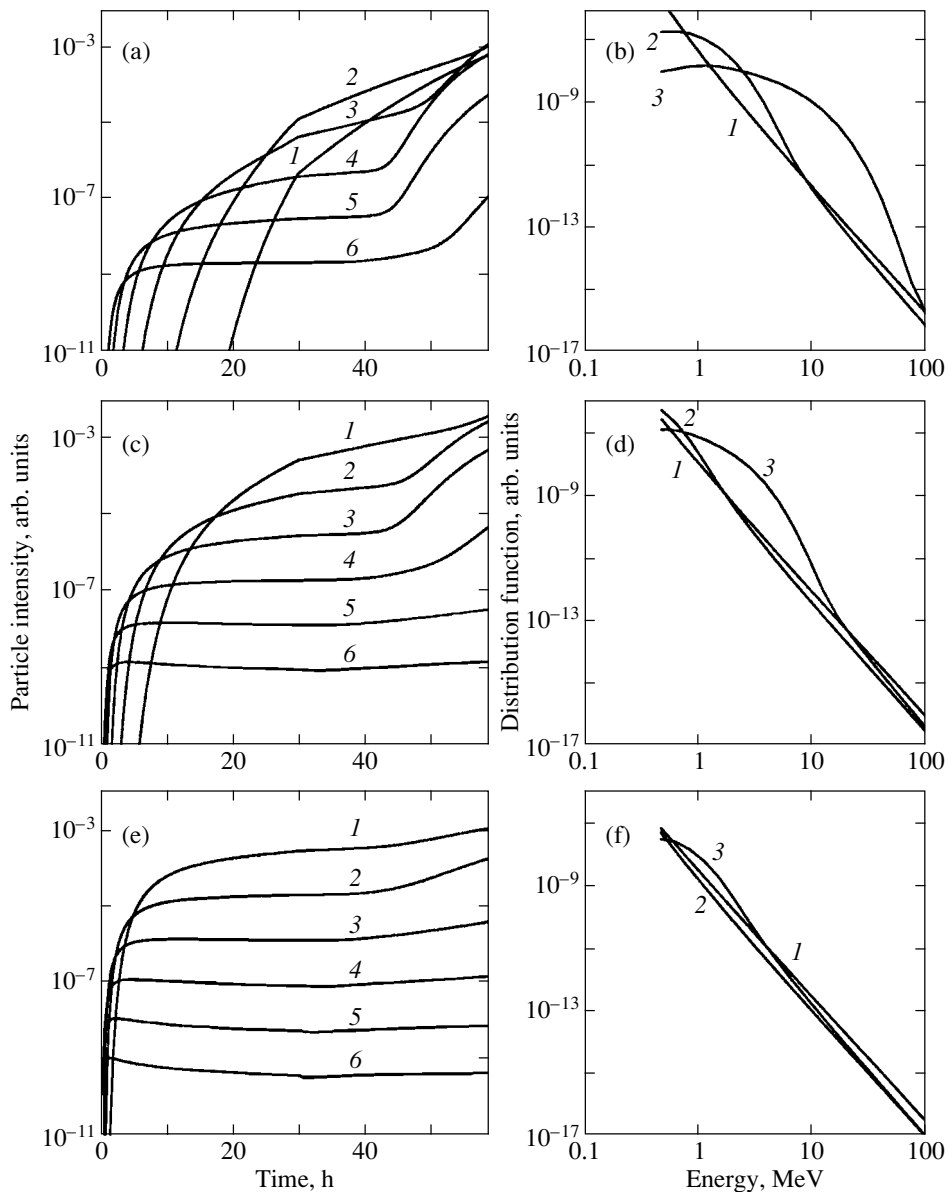


Fig. 2. The same as Fig. 1, but the preshock diffusion coefficient 30-h after particle injection decreases by a factor of 10.

the fact that the amplitude of the injected-particle spectrum at energies close to ϵ_{\min} can only decrease.

Thus, in events with variable diffusion coefficients, a third variant of intensity dynamics is possible. This variant is actually a combination of the two previously considered variants: in the first part of the event, the intensity rapidly reaches its maximum and subsequently changes only slightly (the second variant of dynamics), while in the second part, the decrease in the diffusion coefficients is followed by a significant increase in the intensity up to the shock front (the first variant of dynamics).

Figures 3a, 3c, 3e and 3b, 3d, 3f show the results of our calculations and measurements for the

SEP events of May 2 and August 24, 1998, respectively. The curves 1–9 in Figs. 3a and 3b indicate the SEP intensity as a function of time recorded at the Earth’s orbit in nine energy channels: 1—0.047–0.065; 2—0.112–0.187; 3—0.31–0.58; 4—1.95–4.75; 5—27–41; 6—41–58; 7—58–88; 8—88–180; and 9—180–300 MeV. The curves shown in the same figures and composed of symbols represent our calculations for the energies that correspond to the middle of the energy channel. The vertical solid line in Figs. 3a and 3b corresponds to the shock arrival time. The curves in Figs. 3c and 3d indicate the SEP distribution function at the shock front: the dashed and solid lines represent our calculations for the injection time and the time of shock arrival

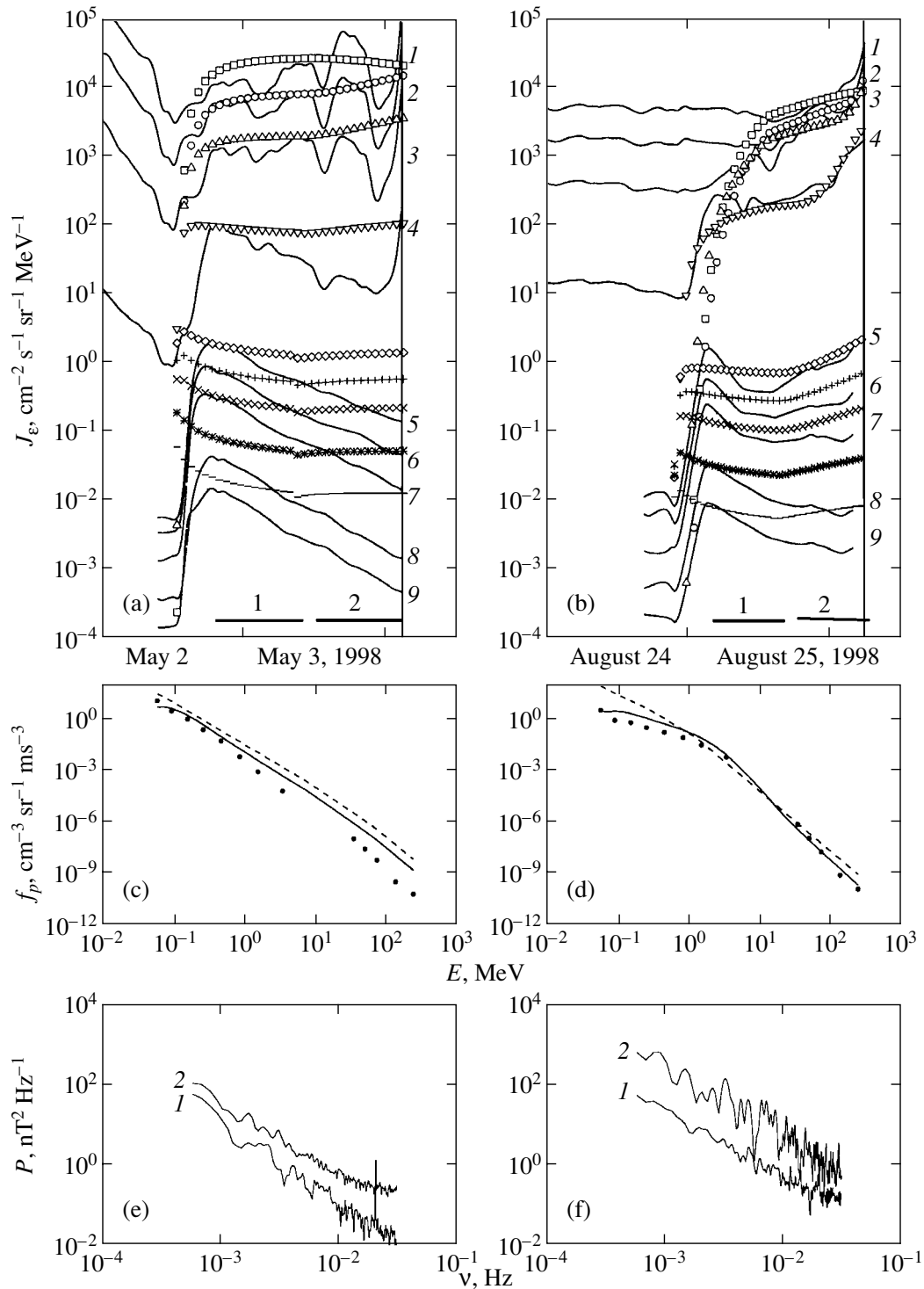


Fig. 3. The SEP intensity in the event of May 2, 1998, recorded at the Earth's orbit in nine energy channels (solid curves 1–9 (a)) versus time. Curves made of symbols represent the calculated intensity of the particles with energies coincident with the middle of the corresponding energy channel. (c) Particle distribution function at the shock front versus energy: dashed and solid lines in the calculations correspond to the injection time and the time of shock arrival at the Earth's orbit, respectively; dots represent the measurements at the time of shock arrival at the Earth's orbit. (e) IMF power spectral density (1, 2) measured at the Earth's orbit during the two time intervals marked in (a) by the corresponding horizontal lines. (b, d, f) The same for the SEP event of August 24, 1998.

at the Earth's orbit, respectively; the dots represent the measurements at the Earth's orbit. The curves 1 and 2 in Figs. 3e and 3f indicate the power spectral density of the interplanetary magnetic field (IMF) determined for the two time intervals marked by the horizontal lines in Figs. 3a and 3b.

The measurements were obtained from two spacecraft: ACE: (i) 1-h SEP flux measurements (curves 1–4 in Figs. 3a and 3b) from the EPAM/LEMS30 experiment; (ii) 1-h solar-wind measurements from the SWEPAM experiment; (iii) 1-h and 16-s IMF measurements from the MAG experiment; and Interball-2: 1-h proton flux measurements with the 10K-80 spectrometer (curves 5–9 in Figs. 3a and 3b).

In our calculations, we used the following measured parameters. For the May 2 event, the preshock solar-wind velocity was $w = 500 \text{ km s}^{-1}$; the shock velocity according to the propagation time of the perturbation $V_s = 1070 \text{ km s}^{-1}$ (as the perturbation, we took the shock wave recorded at the beginning of May 4 rather than the indistinct perturbation that arrived at the Earth's orbit at the end of May 3); the gas compression ratio at the shock front $\sigma = 4$; and the preshock IMF strength $B = 6 \text{ nT}$. For the August 24 event $w = 400 \text{ km s}^{-1}$, $V_s = 1300 \text{ km s}^{-1}$, $\sigma = 3$, and $B = 6 \text{ nT}$.

The diffusion coefficient used in our calculations was determined in accordance with the quasi-linear theory (Lee 1983). Given the numerical values, the expression for this coefficient in the preshock region can be represented as

$$k_1 = \frac{3.6 \times 10^{11}}{P(\nu_0)} \left(\frac{B}{5 \text{ nT}} \right) \left(\frac{\varepsilon}{1 \text{ MeV}} \right)^{\frac{3-\alpha}{2}} (\text{cm}^2 \text{ s}^{-1}), \quad (9)$$

where $P(\nu) = P(\nu_0)(\nu/\nu_0)^{-\alpha}$ is the IMF power spectral density, and $\nu_0 = 2.2 \times 10^{-3}(B/5\text{nT}) \times (w/400 \text{ km s}^{-1})$ (Hz) is the frequency of the Alfvén waves that resonantly interact with protons whose energy is 1 MeV. In the May 2 event, as follows from Fig. 3e: $\nu_0 = 3.3 \times 10^{-3} \text{ Hz}$, $\alpha = 1.9$, $P(\nu_0) = 1 \text{ nT}^2 \text{ Hz}^{-1}$, which gives $k_1 = 4.3 \times 10^{21} \times (\varepsilon/1 \text{ MeV})^{0.55} (\text{cm}^2 \text{ s}^{-1})$. According to the measured IMF power spectrum (curve 2 in Fig. 3e), the diffusion coefficient in the second half of the event decreased by a factor of 3. In accordance with the data for the August 24 event shown in Fig. 3f, $\nu_0 = 2.6 \times 10^{-3} \text{ Hz}$, $\alpha = 1.5$, $P(\nu_0) = 6 \text{ nT}^2 \text{ Hz}^{-1}$, which gives $k_1 = 0.72 \times 10^{21} (\varepsilon/1\text{MeV})^{0.75} (\text{cm}^2 \text{ s}^{-1})$; the latter decreased by a factor of 10 in the second half of the event. As regards the postshock particle diffusion coefficient, we assumed that $k_2 = k_1/10$ in both events.

As follows from the results presented in Figs. 3a, 3c, and 3e, the SEP event of May 2 occurred against the background of a low turbulence level, even when the latter tripled in the second half of the event. As a result, there are no manifestations of diffusive shock acceleration in the temporal dynamics of the SEP intensity. The local low-energy SEP intensity variations (curves 1–3 in Fig. 3a) are probably attributable to the large-scale magnetic clouds from preceding perturbations that crossed the Earth's orbit at that time. In general, the calculations and the measurements for this event are in qualitative agreement. The plane geometry of space adopted in our calculations is responsible for the difference between the calculated and measured temporal behaviors of the particle intensity.

The diffusive shock acceleration mechanism determines the low-energy SEP dynamics for the August 24 event (curves 1–4 in Fig. 3b) because of the higher turbulence level (curves 1 and 2 in Fig. 3f). Our calculations and the measurements in this energy range are in satisfactory agreement. The cause of the significant increase in SEP intensity at the shock front in the channel of minimum recordable energy 47–65 keV remains unclear. In the case of diffusive shock acceleration, the amplitude of the spectrum at these energies is determined by the spectral shape at lower energies, about which we know nothing. Our calculations for the spectrum of the particles injected at the beginning of the event specified in the energy range 30–47 keV by extrapolation yield a much lower intensity amplitude than the measured amplitude. Besides, adding another injection source of the particles left in interplanetary space from preceding perturbations (curves 1–4 for August 24 in Fig. 3b and their extrapolation down to an energy of 30 keV) increases the intensity amplitude only slightly. The significant increase in amplitude at the shock front may result from a manifestation of the drift acceleration mechanism (see, e.g., Decker 1981).

The intensity of high-energy SEPs exhibits an interesting behavior (curves 5–9 in Fig. 3b). According to relation (7), which defines the energy boundary of the particles that were strongly affected by diffusive shock acceleration, we obtain $\varepsilon_* \approx 3 \text{ MeV}$ for the parameters adopted in the August 24 event. Nevertheless, in a range of energies above ε_* , whose width depends on the diffusion coefficient and the shape of the particle spectrum in this energy range, weak manifestations of diffusive shock acceleration are possible; more specifically, there is a small increase in intensity as the shock front is approached and a softening of the spectrum. These manifestations are present in the intensity dynamics of the August 24 SEP event up to an energy of 300 MeV. This may also be the reason why the intensity of the SEPs with energies

up to 500–700 MeV increased at the shock front in the event of November 6, 2001. Thus, a significant decrease in the preshock spatial diffusion coefficient of the particles during the event intensifies the diffusive shock acceleration process. Real-time measurements of the IMF power spectrum can be used to predict increases in the intensity of high-energy SEPs until the shock arrival, which is of considerable interest in space-weather problems.

In general, we may conclude that our calculations and the measurements are in qualitative agreement. The agreement is better for particles whose behavior is determined by acceleration and poorer for particles whose dynamics are dominated by propagation.

CONCLUSIONS

Our studies of the interaction of fast particles with a moving shock front and comparison of our calculations with SEP intensity measurements in interplanetary space have led us to the following conclusions:

The SEP generation region is bounded by the solar corona. The pattern of the subsequent SEP interaction with an interplanetary shock front is mainly determined by the preshock spatial diffusion coefficient of the particles. The strong influence of diffusive shock acceleration causes the shape of the energy spectrum for low-energy SEPs to change—hard and soft spectral regions are formed. The peak of the low-energy SEP intensity coincides with the shock front.

High-energy SEPs weakly interact with the shock front: their spectral shape does not change, and the time at which the intensity reaches its maximum in interplanetary space is well ahead of the shock arrival time.

The energy boundary of the division of protons into low- and high-energy SEPs according to the pattern of their interaction with the shock front for typical interplanetary conditions corresponds to approximately 1 MeV.

In events accompanied by a significant rise of the IMF power spectrum, both variants of temporal dynamics can manifest themselves in the high-energy SEP intensity: the first and second intensity peaks occur at the beginning of the event and at the shock arrival, respectively.

The particle intensity dynamics calculated in terms of the diffusion approximation with the diffusion coefficients calculated by using the quasi-linear theory for the measured IMF power spectrum qualitatively agrees with the observed SEP intensity. Real-time measurements of the IMF power spectral density during an event can be used to predict increases in the intensity of high-energy SEPs until the shock arrival.

ACKNOWLEDGMENTS

We wish to thank the ACE EPAM, SWEPAM, and MAG data preparation team and the ACE Science Center for providing ACE data, which are accessible at <http://www.srl.caltech.edu/ACE/ASC/level2/index.html>. This study was supported in part by the Russian Foundation for Basic Research (project nos. 01-02-17278, 02-02-16096, 03-02-06897-mak, and 03-02-96026-r2003arktika) and the Council for Grants of the President of Russia for State Support of Leading Scientific Schools of Russia (grant no. NS-422.2003.2).

REFERENCES

1. E. G. Berezhko, V. K. Elshin, G. F. Krymsky, and S. I. Petukhov, *Generation of Cosmic Rays by Shock Waves* (Nauka, Novosibirsk, 1988) [in Russian].
2. E. G. Berezhko, S. I. Petukhov, and S. N. Taneev, *Pis'ma Astron. Zh.* **24**, 151 (1998) [*Astron. Lett.* **24**, 122 (1998)].
3. E. G. Berezhko, S. I. Petukhov, and S. N. Taneev, *Izv. Ross. Akad. Nauk, Ser. Fiz.* **65**, 339 (2001).
4. E. G. Berezhko, S. I. Petukhov, and S. N. Taneev, *Proceedings of the 27th ICRC, Hamburg, Germany* **8**, 3215 (2001).
5. R. B. Decker, *J. Geophys. Res.* **86**, 4537 (1981).
6. K. U. Denskat and F. M. Neubauer, *J. Geophys. Res.* **87**, 2215 (1982).
7. S. W. Kahler, *Astrophys. J.* **428**, 837 (1994).
8. M. B. Kallenroude and G. Wibberenz, *J. Geophys. Res.* **102**, 22 311 (1997).
9. C. F. Kennel, F. V. Coroniti, F. L. Scarf, *et al.*, *J. Geophys. Res.* **91**, 11 917 (1986).
10. D. Lario, B. Sanahuja, and A. M. Heras, *Astrophys. J.* **509**, 415 (1998).
11. D. Lario, B. Sanahuja, and A. M. Heras, *ESA Workshop on Space Weather, ESTEC, Noordwijk, Netherlands, 1998*, **WPP-155**, 343 (1999).
12. M. A. Lee, *J. Geophys. Res.* **88**, 6109 (1983).
13. M. A. Lee and J. M. Ryan, *Astrophys. J.* **303**, 829 (1986).
14. C. K. Ng and D. V. Reames, *Astrophys. J.* **424**, 1032 (1994).
15. C. K. Ng, D. V. Reames, and A. J. Tylka, *Geophys. Res. Lett.* **26**, 2145 (1999).
16. D. V. Reames, *Space Sci. Rev.* **90**, 413 (1999).
17. S. A. Starodubtsev, *Phys. Chem. Earth C* **25**, 133 (2000).
18. I. N. Toptygin, *Cosmic Rays in Interplanetary Magnetic Fields* (Nauka, Moscow, 1983) [in Russian].
19. W. Wanner and G. Wibberenz, *J. Geophys. Res.* **98**, 3513 (1993).

Translated by V. Astakhov

Highly Accurate Determination of the Coordinates and the Earth's Rotation Parameters Involving the Svetloe VLBI Observatory

A. M. Finkelstein*, A. V. Ipatov, S. G. Smolentsev,
V. G. Grachev, I. A. Rakhimov, and Z. M. Malkin

Institute of Applied Astronomy, Russian Academy of Sciences, nab. Kutuzova 10, St. Petersburg, 191187 Russia

Received April 22, 2003

Abstract—We present the results of our processing of the first observations of extragalactic radio sources obtained with the eight-element International VLBI Network, which includes the Svetloe Russian Radio Astronomy Observatory equipped with a Mark 3A recording terminal. Our observations and their processing yielded highly accurate coordinates (in meters) of the Svetloe Observatory in the ITRF 2000 system: $X = 2730173.854 \pm 0.002$, $Y = 1562442.668 \pm 0.004$, $Z = 5529969.069 \pm 0.007$. We also show that including the Svetloe Observatory in the International Network led to an appreciable improvement in the accuracy of determining the Earth's rotation parameters (microarcseconds for the coordinates of the pole and nutation angles, microseconds for Universal Time): $X_p = -154683 \pm 77$, $Y_p = 361809 \pm 59$, $UT1-UTC = -325162.9 \pm 2.5$, $\Delta\psi = -53147 \pm 114$, $\Delta\varepsilon = -2286 \pm 47$. © 2003 MAIK "Nauka/Interperiodica".

Key words: *radio interferometry, International Terrestrial Reference Frame, Earth's rotation parameters.*

INTRODUCTION

The Svetloe Radio Astronomy Observatory, the first observatory of the Russian continuously operating Quasar radio-interferometric network, is located in the Priozersk District of the Leningrad Region. It was created primarily for regular VLBI observations in programs of astrometry, geodynamics, and space geodesy (Finkelstein 2001; Gubanov and Finkelstein 2001). Svetloe is a specialized radio-interferometric station equipped with all of the necessary tools for VLBI observations of extragalactic radio sources.

By the end of 2002, the observatory was equipped with the only recording terminal—a Canadian S2 terminal with video converters, designed at the Institute of Applied Astronomy, Russian Academy of Sciences. Using this terminal, we have carried out observations under several programs together with VLBI stations of China, Canada, and Australia equipped with similar terminals, as well as with the other Quasar network observatory located in the Cossack village Zelenchukskaya, Karachaevo-Cherkessian Republic. At the end of 2002, in accordance with agreement between the Russian Academy of Sciences and NASA, a Mark 3A recording terminal was installed at the observatory, and from the beginning of

2003, it was incorporated into the International VLBI Service (IVS) for Geodesy and Astrometry. A number of large and long-term international astrometric and geodynamic VLBI programs, developed together with the Institute of Applied Astronomy, Russian Academy of Sciences, are being implemented within the IVS framework.

In this paper, we report the first results of one such programs that allowed us to radically improve the three-dimensional coordinates of the Svetloe Observatory, to significantly refine its position in the IVS network, and to estimate its influence on the accuracy of determining the Earth's rotation parameters.

INSTRUMENTATION OF THE OBSERVATORY

The main element of the instrumentation at the Svetloe Observatory is a new-generation, fully steerable radio telescope (Fig. 1) with a homologous mirror (Finkelstein *et al.* 2002). The quasi-parabolic mirror of the radio telescope has a diameter of 32 m and a focal length of 11.4 m. The secondary mirror, fixed to the supports of the primary mirror near the prime focus, is a modified hyperboloid of revolution with a diameter of 4 m.

The radio telescope has two modes of motion: fast (1.5 s^{-1} in azimuth and 0.8 s^{-1} in elevation) and slow (1.5 s^{-1} in azimuth and 0.8 s^{-1} in elevation), which

*E-mail: amf@quasar.ipa.nw.ru



Fig. 1. The radio telescope of the Svetloe Observatory.

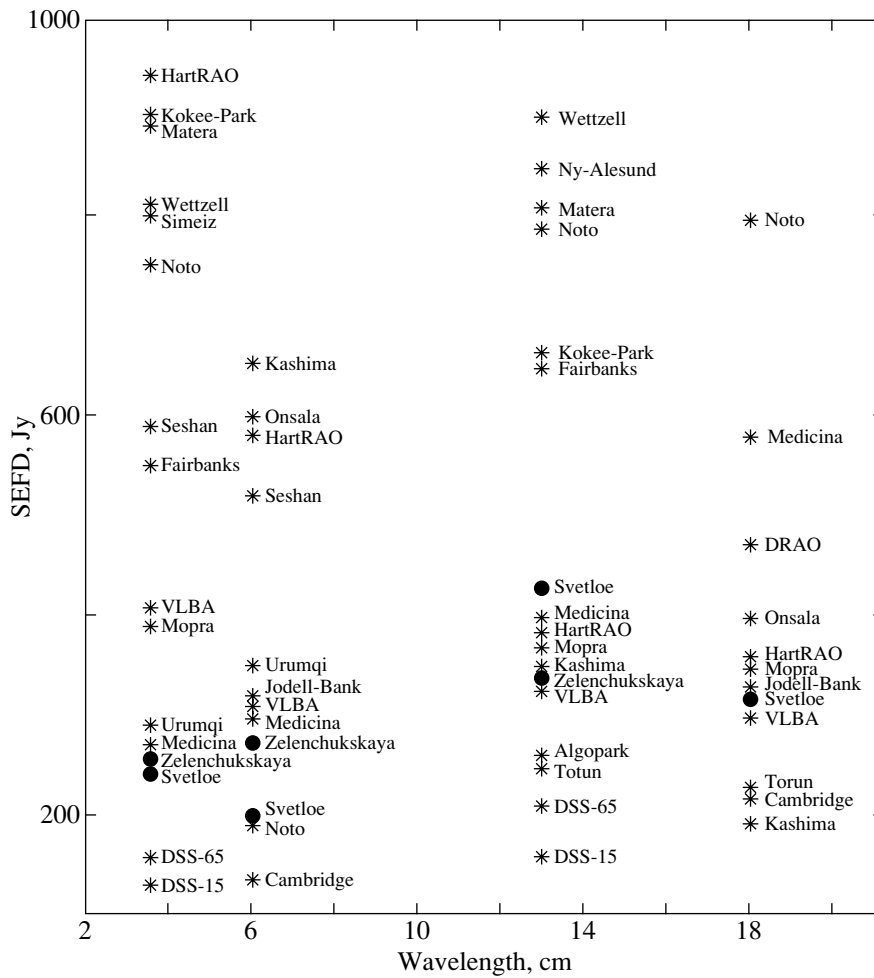


Fig. 2. SEFD values for the radio telescopes of the IVS network.

makes it possible not only to track radio sources but also to quickly repoint the antenna from one source to another. This is necessary for the carrying out of any astrometric or geodynamic program. A cable system

rotates the antenna by $\pm 270^\circ$ in azimuth from the central position northward and in the elevation range (from -5° to $+90^\circ$), which allows us to optimize var-

ious programs of observations of many radio sources located at widely differing hour angles.

The radio telescope is equipped with five low-noise cooled HEMT (High Electron Mobility Transistor) receivers for wavelengths of 1.35, 3.5, 6.0, 13, and 18/21 cm, which allow observations in two orthogonal circular polarizations to be carried out (Ipatov *et al.* 1994; Ivanov *et al.* 1997). To achieve a noise temperature of the radio telescope–radiometer system of ~ 50 K, some of the input circuits of all bands are cooled down to 20 K. Closed-cycle microcryogenic systems are used to cool the low-noise devices of all bands down to 20 K. Figure 2 compares the system equivalent flux densities (SEFD) in the above bands of the Svetloe Observatory with those of other VLBI stations (including the second station of the Quasar Network, the Zelenchukskaya Observatory). This comparison shows that by this parameter, Svetloe ranks among the world's best VLBI stations.

The illumination system consists of horn feeds arranged in a circle with a diameter of 3.6 m. The working band is rapidly changed by rotating the remotely controlled secondary mirror, an asymmetric subdish, through an appropriate angle around the radio telescope axis.

S/X-band receivers (3.5/13 cm) with a common feed (Fig. 3) are used to implement astrometric, geodynamic, and geodesic programs with efficient suppression of ionospheric effects. The working intermediate frequency ranges of these cryoelectronic radiometers are 130–480 MHz and 130–890 MHz for the 13- and 3.5-cm bands, respectively. The noise temperature at the cryostat flange is 15 K, and the total noise temperature of the radio telescope–radiometer system does not exceed 50 K in the S-band and 70 K in the X-band for elevations larger than 20° (Fig. 4).

The signal from the radiometer outputs is fed through the phase-stable coaxial lines connecting the focal cabin of the radio telescope with the technical building to the input of a 14-channel Mark 3A recording terminal. The coaxial lines include amplifiers to adjust the nonuniformity of the transmission coefficient. The frequencies are converted to the video band by synchronized local oscillators with frequencies of 2020 and 8080 MHz for 13 and 3.5 cm, respectively.

The Mark 3A recording terminal performs the following functions: amplification and separation of the intermediate-frequency signal, conversion of the signal to the video frequency, clipping the output signals at a zero level and feeding the clipped signals to the recording system, measurement of the power of the received intermediate-frequency signal, and phase control. Information is recorded on magnetic tape by a Honeywell 24-track tape recorder; one tape

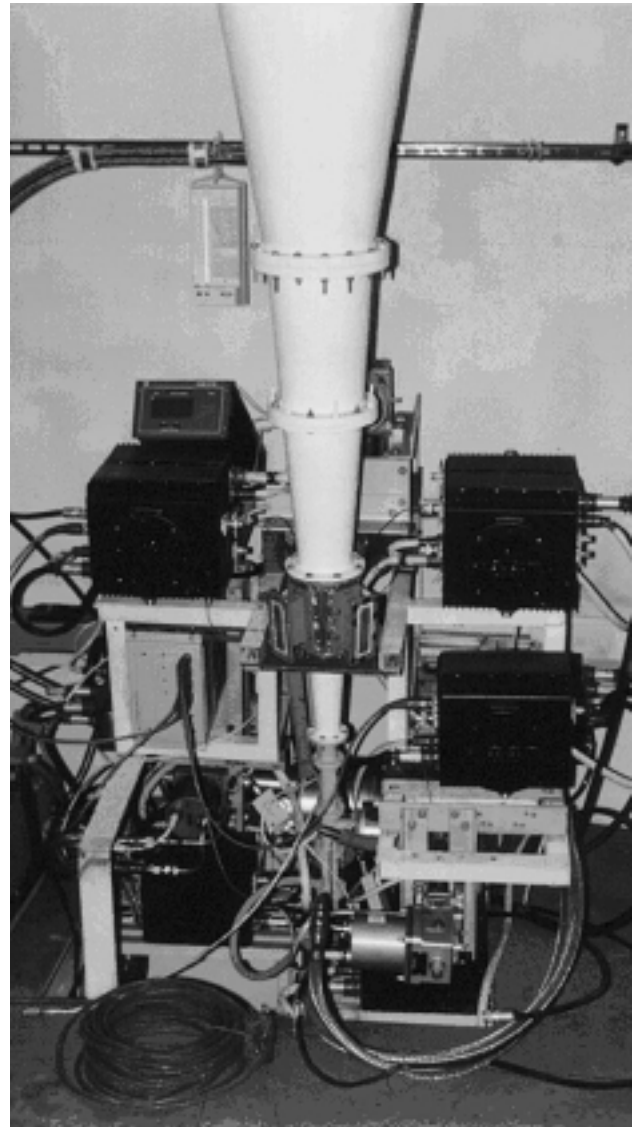


Fig. 3. S/X-band (3.5/13 cm) receivers of the Svetloe Observatory.

records an 18–24-hour observational session, depending on the time required for repointing the telescope from one source to another.

The Svetloe VLBI station has a high-quality time–frequency synchronization system (Vytov *et al.* 1997). It includes four hydrogen maser frequency standards with long-term stability not worse than $(3-5) \times 10^{-15}$; one of the standards is always operational, while any other standard can be activated within one hour and can reach nominal technical parameters within another 24 hours. Comparison and time referencing relative to Moscow time and Coordinated Universal Time is made with an rms error of (30–50) ns by using the receivers of the GPS and GLONASS satellite navigation systems.

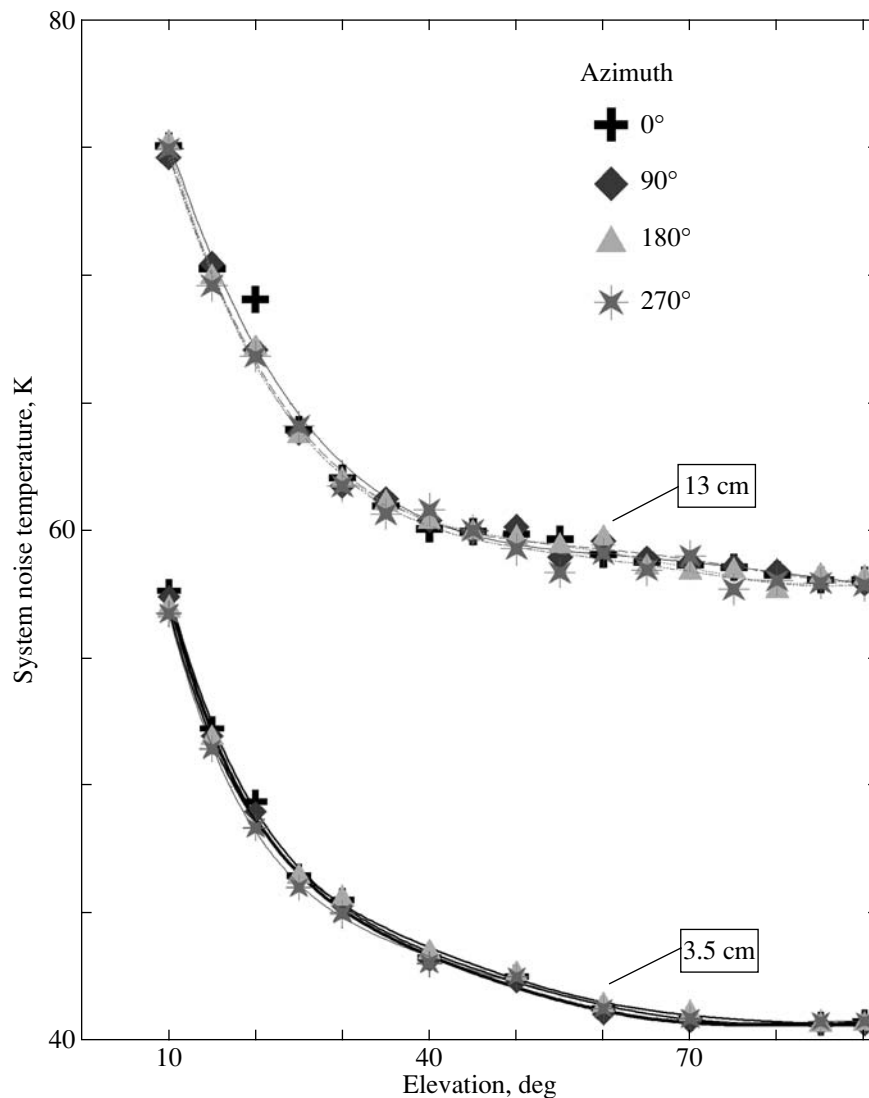


Fig. 4. Noise temperature of the radio telescope—radiometer system at the Svetloe Observatory.

The phase calibration of the system, which uses a picosecond pulse generator, consists of two main units: a pulse generator of harmonics based on a semiconductor diode and a square signal shaper with a frequency of 1 MHz from a harmonic signal with a frequency of 5 MHz fed from the hydrogen oscillator of the station. The delay in the propagation of the 5-MHz reference signal in the cable system is measured by means of a phase comparator, using the direct and delayed signals from the phase calibration oscillator fed into its comparison inputs.

The control system of meteorological parameters (atmospheric pressure, wind direction and strength, temperature, and humidity) is a high-precision software-hardware automated measurement system. The sampling rate of the measurements by this system for automatic writing to a log file of the observational

session is regulated over a wide range by a control program in the Windows 98 environment.

All of the systems of the radio telescope were combined into a single complex using a central computer with special-purpose software that allows observations to be carried out in a completely automated mode. The central computer not only controls the process of observations proper but also writes the results of the commands performed by the equipment of the radio telescope and the operational information (meteorological and metrological information, operator's comments, etc.) to a log file together with the results of the observations, which considerably facilitates antenna control and the data correlation process.

The Mark IV Field System, Version 9.5.17 (FS), which is the international standard for VLBI (Himwich 1996, 2000) and is installed on radio telescopes



Fig. 5. Locations of the IVS network observing stations involved in the experiment.

with various control systems, forms the basis for this software. Although FS provides a ready-to-use interface to the various recording systems (Mark 3–5, VLBA, S2, K4), it does not contain modules for controlling the antenna and specific equipment of the radio telescope. Therefore, it was supplemented with a station-oriented interface for controlling the antenna, a receiving complex, and a radiometric recording system. The software for this interface was developed in the Linux environment using specific commands in the SNAP language (used in standard FS) and completely integrated into the FS environment for observations in both VLBI and single-dish mode (Mikhailov 2000).

OBSERVATIONS AND RESULTS

At the beginning of December 2002, the Mark 3A VLBI terminal was installed at the Svetloe Observatory. On December 12, we performed, in cooperation with NASA experts, test VLBI observations of the radio sources 0552+398, 0923+392 and 1606+106 in the S/X bands together with the 20-m radio telescope in Wettzell (Germany) and the 20-m radio telescope in Ny-Alesund (Norway). The successful correlation processing carried out at the Max Planck Institut für Radioastronomie in Bonn (Germany) allowed us to reconcile and refine several technical parameters of the instruments important for subsequent joint observations.

The first regular VLBI observations at the Svetloe Observatory were carried out from 18^h29^m50^s UT March 6, 2003, through 15^h52^m53^s UT March 7, 2003, under a program for determining the Earth's rotation parameters (experiment R4061) within the intercontinental VLBI network. The latter consists of

eight globally distributed stations (Fig. 5) that formed 28 interferometric baselines with lengths of from 990 km (Wettzell–Matera) to 11064 km (Kokee–Fortaleza). The size of the network was 82° in latitude and 170° in longitude. Table 1 lists the stations, their locations, and the distribution of scans.

The total number of program radio sources was 36; 29 of them were observed at the Svetloe Observatory. The total number of planned scans at the Svetloe Observatory was 132; for technical reasons, we completed only 116 of them. Each of the radio sources was observed on the network, on average, nine times with durations from 1.5 to 12.5 min; thus the total number of scans was 1398. The tapes were processed on the correlator at the US Naval Observatory, Washington, D.C.; 2373 radiointerferometric delays were processed, 2060 of which were used in the analysis.

The mean error of a single observation (radio-interferometric delay obtained on a single baseline) was 18.4 ps (5.5 mm), and while mean error of the ionospheric correction from the S/X-band observations was 8.7 ps (2.6 mm). In the correlation processing, we simultaneously determined the fringe rate with a mean error of 20.8 fs s⁻¹.

The secondary processing of the observations was performed in order to improve the coordinates of the Svetloe radio telescope and to calculate the Earth's rotation parameters for the epoch of the observations.

When improving the coordinates, we used the conventional and GPS measurements on the local geodesic network of the observatory (Kazarinov and Malkin, 1997) as *a priori* data. The geocentric coordinates of the radio telescope (the point of intersection of the axes) obtained using the OCCAM/GROSS

Table 1. Stations involved in the experiment

Station	Location	Distance from Svetloe, km	Number of scans
Algonquin Park	Canada	6256	192
Fortaleza	Brazil	8428	104
Gilmore Creek	USA, Alaska	5854	219
Kokee Park	USA, Hawaii	9561	168
Matera	Italy	2374	183
Ny-Alesund	Norway, Spitsbergen	2133	199
Svetloe	Russia	—	132
Wetzell	Germany	1655	201

Table 2. Coordinates of the Svetloe station determined in the experiment

Processing center	X , m	Y , m	Z , m
Institute of Applied Astronomy GSFC	$2\,730\,173.854 \pm 0.002$	$1\,562\,442.668 \pm 0.004$	$5\,529\,969.069 \pm 0.007$
	$2\,730\,173.851 \pm 0.003$	$1\,562\,442.664 \pm 0.002$	$5\,529\,969.063 \pm 0.006$

Table 3. Baseline lengths determined in the experiment

Baseline Svetloe	Number of observations	Length, m	Error, m
Algonquin Park	57	6 255 567.630	0.005
Fortaleza	31	8 428 008.668	0.010
Gilmore Creek	62	5 853 689.130	0.005
Kokee Park	35	9 561 115.418	0.008
Matera	75	2 373 640.095	0.003
Ny-Alesund	67	2 133 122.998	0.003
Wetzell	73	1 654 774.855	0.002

Table 4. The Earth's rotation parameters as determined from experimental data

Number of stations	X_p , μas	Y_p , μas	UT1–UTC, ms	$\Delta\psi$, μas	$\Delta\varepsilon$, μas	σ_0 , ps	C_{max}
8 (all stations)	$-154\,683 \pm 77$	$361\,809 \pm 59$	$-325\,162.9 \pm 2.5$	$-53\,147 \pm 114$	-2286 ± 47	17	0.63
7 (without Svetloe)	$-154\,724 \pm 84$	$361\,833 \pm 64$	$-325\,159.3 \pm 2.9$	$-53\,097 \pm 122$	-2292 ± 50	20	0.66

Note: X_p , Y_p are the coordinates of the pole; UT1–UTC is the Universal Time; $\Delta\psi$, $\Delta\varepsilon$ are the nutation angles; σ_0 is the error of the unit weight; and C_{max} is the maximum correlation between the Earth's rotation parameters.

package developed at the Institute of Applied Astronomy, Russian Academy of Sciences (Titov and Zarraoa 1997; Malkin *et al.* 2000) are presented in Table 2. For comparison, this table also gives the coordinates obtained at the leading western VLBI processing center—the NASA Goddard Space Flight Center (Petrov 2003). Table 3 lists the baselines between the Svetloe radio telescope and other radio

telescopes of the VLBI network, determined from the experimental results.

The coordinates were obtained in the International Terrestrial Reference Frame ITRF 2000 for the epoch 2003.18 (March 7, 2003) relative to the reference stations included in this system. The coordinates of the Gilmore Creek station were corrected for the displacement of the station during a strong earthquake

in Alaska in November 2002, when the station was displaced by 6 cm.

The coordinates and velocities of the reference stations in the ITRF 2000 catalog contain errors for this network at a level of 2 mm (for the epoch 1997.0) and 0.3 mm yr^{-1} , respectively. Therefore, the processing was performed with different sets of reference stations. The errors of the coordinates and the baselines listed in Tables 2 and 3 correspond to the discrepancy between the results obtained in different processing variants.

In general, the results of the determination of the coordinates for the Svetloe Observatory and the network baselines show a high degree of accuracy in the observations and processing.

The main goal of the IVS program under discussion was to determine the Earth's rotation parameters. For this reason, we estimated the coordinates of the pole X_p , Y_p , the Universal Time UT1–UTC, and the nutation angles $\Delta\psi$ and $\Delta\epsilon$ from the VLBI observations with and without the Svetloe Observatory (Table 4).

We see from our results that even the first inclusion of the Svetloe Observatory in the IVS network significantly improved the accuracy of the results.

Twenty sessions of the R4 program have been scheduled for 2003, which will allow us to further improve the accuracy of determining the Earth's rotation parameters. Five sessions of the T2 program planned for the same period, aimed at improving the coordinates of the network stations, will allow us to begin the determination of the tectonic motions of the Svetloe Observatory.

ACKNOWLEDGMENTS

We wish to thank our American colleagues, C. Ma and E. Himwich (Goddard Space Flight Center, NASA) and B. Corey (Haystack Observatory,

Massachusetts Institute of Technology) for their fruitful collaboration in VLBI technology and space geodesy. This was crowned with the installation of the Mark 3A terminal at the Svetloe Observatory and its inclusion in the IVS network.

REFERENCES

1. A. M. Finkelshtein, *Nauka Ross.* **5**, 20 (2001).
2. A. Finkelstein, A. Ipatov, and S. Smolentsev, in *Fourth APSGP Workshop*, Ed. by H. Cheng and Q. Zhihan (Shanghai Sci. and Technic., Shanghai, 2002), p. 47.
3. V. S. Gubanov and A. M. Finkelstein, *Tr. IPA RAN* **6**, 3 (2001).
4. E. Himwich, in *Technical Workshop for APT and APSG* (Communication Research Lab., Kashima, 1996), p. 149.
5. E. Himwich, in *IVS 2000 General Meeting*, Ed. by N. Vandenberg and K. Baver (NASA, Washington, 2000), p. 86.
6. A. V. Ipatov, I. A. Ipatova, and V. V. Mardyshkin, in *Progress and Future Observational Possibilities*, Ed. by T. Sasao (Terra Sci., Tokyo, 1994), p. 200.
7. D. V. Ivanov, A. V. Ipatov, I. A. Ipatova, *et al.*, *Tr. IPA RAN* **2**, 242 (1997).
8. A. S. Kazarinov and Z. M. Malkin, *Tr. IPA RAN* **2**, 286 (1997).
9. Z. Malkin, A. Voinov, and E. Skurikhina, *ASP Conf. Ser.* **216**, 632 (2000).
10. A. G. Mikhailov, in *Proceedings of the Conference: Astrometry, Geodynamics, and Celestial Mechanics at the Threshold of the XXI Century* (IPA RAN, St. Petersburg, 2000), p. 358 [in Russian].
11. L. Petrov, <http://gemini.gsfc.nasa.gov/pet/discussion/svetloe/> (2003).
12. O. Titov and N. Zarraoa, *Commun. IAA* **69** (1997).
13. A. V. Vytov, E. T. Zhukov, Ya. L. Laguzova, and S. G. Smolentsev, *Tr. IPA RAN* **2**, 276 (1997).

Translated by G. Rudnitskii

Models and Theoretical Spectrum for the Free Oscillations of Saturn

T. V. Gudkova* and V. N. Zharkov

*Schmidt Joint Institute of Physics of the Earth, Russian Academy of Sciences,
ul. Bol'shaya Gruzinskaya 10, Moscow, 123810 Russia*

Received May 6, 2003

Abstract—We constructed new models of Saturn with an allowance made for a helium mass fraction of ~ 0.18 – 0.25 in its atmosphere. Our modeling shows that the composition of Saturn differs markedly from the solar composition; more specifically, during its formation, the planet was ~ 11 – 15 planetary masses short of the hydrogen–helium component. Saturn, as well as the other giant planets, must have been formed according to Schmidt's scenario, through the formation of embryonic nuclei, rather than according to Laplace's scenario. The masses of the embryonic nuclei themselves lie within the range $(3.5$ – $8) M_{\oplus}$. We calculated a theoretical free-oscillation spectrum for our models of Saturn, each of which fits all of the available observational data. The results of our calculations are presented graphically and in tables. Of particular interest are the diagnostic potentialities of the discontinuity gravitational modes related to density jumps in the molecular envelope of Saturn and at the interface between its molecular and metallic envelopes. When observational data appear, our results can be used both to identify the observed modes and to improve the models themselves. We discuss some of the cosmogonical aspects associated with the formation of the giant planets. © 2003 MAIK "Nauka/Interperiodica".

Key words: *Solar system—planets, interior-structure models, free oscillations.*

INTRODUCTION

The Galileo space probe that plunged into the atmosphere of Jupiter reliably determined the helium mass fraction $Y_1 = 0.234 \pm 0.005$ in the planetary atmosphere on the assumption that the heavy-element mass fraction was $Z = 0.019$ (Von Zahn and Hunten 1996; Von Zahn *et al.* 1998). This value is appreciably higher than the corresponding Voyager estimate $Y_1 = 0.19$ (Gautier *et al.* 1981). Therefore, the authors of the experiment to determine the helium abundance in the atmosphere of Saturn from Voyager data (Conrath *et al.* 1984) reconsidered their results (Conrath and Gautier 2000), especially since the previous estimate of the helium abundance in the atmosphere of Saturn was actually too low ($Y_1 = 0.06$ – 0.11).

An important boundary condition in constructing an interior-structure model for Saturn is the helium abundance in its atmosphere. A new estimate of the helium abundance in the atmosphere of Saturn ($Y_1 = 0.18$ – 0.25) (Conrath and Gautier 2000) makes the construction of new interior-structure models for the planet a pressing problem. In 2004, the Cassini–Huygens spacecraft will place an artificial satellite in orbit around Saturn and will drop a probe into the atmosphere of Titan. As a result, the science

of Saturn and its satellite Titan is expected to be developed further. In contrast to Jupiter (Gudkova and Zharkov 1999b), the free-oscillation spectrum of Saturn has not yet been studied in detail. Based on our new models of the planet, we carry out such a study in the second part of our paper.

Saturn is a convective, adiabatic, gaseous–liquid planet (Hubbard *et al.* 1974).

The first modern models of Saturn were constructed in 1974 (Zharkov *et al.* 1974a, 1974b). The methods for constructing models of the giant planets are described in detail in these papers and in a book by Zharkov and Trubitsyn (1980).

The materials of the protoplanetary gas–dust cloud from which a planetary model is constructed can be subdivided by their volatility into three groups: (1) gases (H_2 , He, Ne, ...), the G component; (2) ices (H_2O , CH_4 , NH_3), the I component; and (3) rocks (oxides, iron, and iron compounds), the R component. The materials in each group are taken in solar proportion. The outer envelopes of Saturn consist of the G component with an admixture of the IR component, while its core consists of an IR mixture. The currently available data do not allow us to raise and solve the question of whether the IR core of the planet is separated into an inner R core and an outer I core. Therefore, in our models, the core consists of an IR mixture. In the modern models of Saturn, a helium-rich layer produced by helium

*E-mail: gudkova@uipe-ras.scgis.ru

sedimentation over the evolutionary history of the planet overlies an IR core.

The 1974 models of Saturn are characterized by two jumps in the radial density profile. The first density jump is related to the molecular–metallic phase transition of hydrogen at a pressure $P = 3$ Mbar. The second, deeper jump corresponds to the interface between the metallic hydrogen envelope and the IR core and is attributable to the change in chemical composition.

The interior-structure models improve with improving equations of state and observational data. The 1974 models of Saturn had the same composition for the outer molecular and inner metallic envelopes. The appreciable change in the observed gravitational moment J_4 from $(-10.1 \pm 0.7) \times 10^{-4}$ (Dollfus 1970) to $(-9.17 \pm 0.38) \times 10^{-4}$ (Null *et al.* 1981) suggested an increase in the weight of the inner part of the molecular envelope compared to its outer part. Gudkova *et al.* (1988) and Zharkov and Gudkova (1991) introduced a two-layer molecular envelope whose inner part was made heavier by the IR component and whose outer part was enriched with the I component. The composition of the latter was determined from data on the atmospheric composition. The assumption that conditions arise in the inner molecular envelope for the dissolution of the IR component in it with increasing pressure and temperature served as a physical underpinning for this subdivision. As the observational data improve and the observational base expands, the molecular envelope may in the future have to be subdivided into a larger number of layers.

Modern models of Saturn consist of five layers: a two-layer molecular envelope, a metallic hydrogen envelope, and a two-layer core (Gudkova and Zharkov 1988, 1996, 1997; Zharkov and Gudkova 1991). At present, there are several uncertainties in the interior-structure models of Saturn:

(1) In principle, the mass of the IR core can range widely (from 0 to $20M_{\oplus}$) (Gudkova and Zharkov 1997; Guillot 1999).

(2) The hydrogen metallization pressure ranges from 1.5 to 3 Mbar.

Hydrogen and helium comprise most of the planet. One of the principal uncertainties is the equation of state for the hydrogen–helium mixture. An important model parameter is the pressure at which the transition to monoatomic metallic hydrogen occurs in Saturn. It depends on many factors and cannot yet be reliably determined. Since the first studies (Zharkov *et al.* 1974a, 1974b), this pressure has been assumed to be 3 Mbar. Currently, there is evidence that this transition in Jupiter and Saturn can occur at a lower pressure (Sumon *et al.* 1995). These authors predict

a new type of phase transition in hydrogen—a plasma phase transition. According to their estimates, this transition must occur in hydrogen at high temperatures and pressures of ≈ 1.7 Mbar.

Having analyzed the experimental data, Weir *et al.* (1996) and Nellis *et al.* (1998) showed that the properties of liquid hydrogen at high pressures and temperatures significantly differ from the properties of crystalline hydrogen at high pressures. They found that, depending on the (P, T) path of hydrogen compression, there comes a time when the dissociation of molecular hydrogen, accompanied by a rapid increase in electrical conductivity, begins. Even at 10% dissociation, the electrical conductivity of liquid hydrogen acquires values characteristic of liquid metals. Metallization terminates in the pressure range $\sim 1.5 - 2$ Mbar. According to these results, the pressure of the phase transition to a univalent metallic state in the models of Jupiter and Saturn was lowered from 3 to 1.5–2 Mbar.

In Jupiter and Saturn, the molecular envelopes that border the metallic envelopes contain an appreciable amount of the metallized admixtures present in the IR component. Metallized admixtures can cause the hydrogen metallization pressure to decrease.

(3) A radiative zone could exist. Recently, based on careful opacity calculations for the compositions characteristic of the outer envelopes of the giant planets, Guillot *et al.* (1994a) have suggested that these adiabatic molecular envelopes near the surface contain thin radiative zones where heat is transferred by radiation. Models of the giant planets with thin radiative zones near the surface were constructed by Guillot *et al.* (1994b). Including a thin radiative layer in an adiabatic model does not change the density distribution in the planet (due to the change in chemical composition) but does lower the temperature distribution in the deep interiors.

Galileo probe measurements show that the temperature profile in Jupiter is nearly adiabatic down to a level of 20 bar (Seiff *et al.* 1996).

Gudkova *et al.* (1995) compared the differences between the models with different equations of state for hydrogen (a discontinuous or continuous phase transition) and between the convective and radiative–convective models by using seismological criteria.

Previously, a set of models that fitted all of the observational data were constructed for Saturn (Gudkova and Zharkov 1996, 1997; Guillot 1999). However, without imposing additional constraints, preference can hardly be given to a particular model. At present, expanding the observational data base for Saturn is still a pressing problem. It would be most promising to record and identify the eigenmodes of Saturn. These data would provide new information

on the planetary interiors, much as helioseismology contributed enormously to our understanding of the solar interior structure. This would raise the problem to the level of helioseismology.

In the case of recording the eigenmodes to identify the oscillations and obtaining information about the planetary interiors from the observed acoustic modes, the theoretical acoustic oscillation spectrum of the planet must be studied first.

Marley and Porko (1993) considered the problem of using the rings of Saturn to record some of its modes. An overview of the seismological studies for Jupiter and Saturn carried out before 1993 was given by Lognonne and Mosser (1993).

Vorontsov *et al.* (1989) showed that, in contrast to helioseismology, in Jovian seismology, the asymptotic theories cannot be used to study the high-frequency acoustic spectrum. The spectrum turned out to be very sensitive to the properties of Jupiter's core and to density jumps in the planetary interiors. Advances in helioseismology (Vorontsov and Zharkov 1988), which made it possible to study the internal structure of the Sun in the statement of the inverse problem, affect the progress of Jovian and Saturnian seismology.

The free-oscillation spectrum of Jupiter and Saturn can be divided into the low- and high-frequency regions. The high-frequency acoustic oscillations were discussed by Bercovici and Schubert (1987), Mosser *et al.* (1988), Vorontsov *et al.* (1989), Lee (1993), and Provost *et al.* (1993). The high oscillation frequencies are presented in the form of an echelle diagram (in helioseismology, an echelle diagram is commonly used to compare the theoretical and observed solar oscillation frequencies). The shape of these curves for Jupiter turns out to be very sensitive to the core size and structure. The recording of high-frequency oscillations and their comparison with predictions of various models would undoubtedly give unique information about the central structure of Jupiter.

In studying the high-frequency free-oscillation spectrum of Saturn, we must supplement the model of its interior structure, which is constructed from the center to a $P = 1$ bar level, with an atmospheric model for pressures below 1 bar. The influence of the troposphere on the free-oscillation periods was investigated in detail by Mosser *et al.* (1994).

Vorontsov *et al.* (1976), Vorontsov and Zharkov (1981a, 1981b), and Vorontsov (1981) calculated the free-oscillation spectrum for the 1974 model of Saturn and studied all of the rigid-body and differential rotation effects by using the perturbation theory.

Here, we constructed new models of Saturn and calculated the free-oscillation spectra for them. All of the rotation effects were considered in detail by

Vorontsov and Zharkov (1981b). They developed a second-order perturbation theory to determine the influence of all of the rotation effects—the Coriolis forces, the centrifugal forces, and the ellipticity—on the free oscillations of a gaseous–liquid planet. The perturbation theory was constructed by taking into account the interaction of various oscillation modes due to multiplet splitting because of the planetary rotation and their overlapping. Below, we do not calculate the second-order corrections. These calculations are laborious, and it makes sense to accurately calculate them only when observational data are available.

THE INTERIOR STRUCTURE OF SATURN

Observational Data

The following observational data are used to construct models of the giant planets: the mass of the planet; the mean density; the gravitational moments J_2 , J_4 , and J_6 ; and the rotation period. Data on the atmospheric chemical composition of the planet and its surface temperature (T_1 at $P = 1$ bar) are used as the boundary conditions.

Helium is currently believed to have been slightly differentiated from outer solar layers into deeper zones during the lifetime of the Sun. The protosolar helium abundance $Y_0 = 0.270 \pm 0.005$ (Bahcall and Pinsonneault 1995) is taken as a boundary condition in constructing interior-structure models for Jupiter and Saturn. It is slightly higher than the current helium abundance in the solar atmosphere, $Y = 0.24$, that was estimated by helioseismological methods.

In comparison with the solar abundance, the atmosphere of Saturn is enriched with carbon by a factor of 2–7 and with nitrogen by a factor of 2 or more (Gautier and Owen 1989). In our models, we assume an enrichment with CH_4 and NH_3 by a factor of 4. There are no data on the oxygen abundance in the atmosphere of Saturn. Gudkova and Zharkov (1996) constructed models of Saturn enriched with ices by a factor of 4, with CH_4 and NH_3 by a factor of 4, and with H_2O by a factor of 10 compared to the solar abundances. Gudkova and Zharkov (1997) constructed water-depleted models of Saturn by analogy with Jupiter's models, whose water content was 0.2 of the solar value. In these papers, the helium abundance in the outer envelope was taken to be equal to the value obtained after the Voyager data processing, $Y_1 = 0.06$. By analogy with the increased helium abundance in the Jovian atmosphere, as derived from Galileo data, in comparison to Voyager data we took a trial value of $Y_1 = 0.10$, which was within the error limits.

In the Introduction, we noted that Conrath and Gautier (2000) reanalyzed the Voyager data and obtained a helium abundance in the atmosphere of Saturn ($Y_1 \approx 0.18\text{--}0.25$) that was much higher than that used previously ($Y_1 \approx 0.06\text{--}0.11$).

Saturn exhibits noticeable differential rotation. The model gravitational moments are calculated by assuming rigid-body rotation. Therefore, the model gravitational moments are compared with those obtained by subtracting the corrections for differential rotation ΔJ_2 and ΔJ_4 from the observed moments of J_2 and J_4 . For Saturn, $\Delta J_2 = 8 \times 10^{-5}$ and $\Delta J_4 = -2 \times 10^{-5}$ (Hubbard and Stevenson 1984).

The model moments J_{2n}^{ri} were calculated by using integral formulas of the fifth-approximation figure theory (Zharkov and Trubitsyn 1975). In general form, these formulas are

$$J_{2n}^{ri} = \int_0^1 \chi_{2n}(\beta) d\beta,$$

where $\beta = r/R$ is the dimensionless radius, and R is the radius of the planet. Dividing both sides by J_{2n}^{ri} (Zharkov and Trubitsyn 1974; Efimov *et al.* 1977), we introduce the functions g_{2n}

$$\int_0^1 g_{2n}(\beta) d\beta = 1,$$

where $g_{2n}(\beta) = \chi_{2n}(\beta)/J_{2n}^{ri}$.

Figure 1 shows the functions $g_{2n}(\beta)$ for Saturn (Sa8). The model itself is discussed below. The functions $g_{2n}(\beta)$ have a simple physical meaning: they are the relative densities of the gravitational moment J_{2n}^{ri} , and the quantity $g_{2n}(\beta)d\beta$ gives the relative contribution to J_{2n}^{ri} from the region of the planet located in the interval $[\beta, \beta + \Delta\beta]$. The plots of $g_{2n}(\beta)$ show the contributions of various planetary interior zones to J_{2n}^{ri} .

Models

Let us denote the mass fractions of hydrogen, helium, and the IR component by X , Y , and Z , respectively, so that $X + Y + Z = 1$ for each envelope of the planetary model. The subscripts on X , Y , and Z will indicate to which envelope the corresponding mass fraction pertains (the layers are numbered from the surface: (1) the outer hydrogen–helium molecular envelope, (2) the inner hydrogen–helium molecular envelope, (3) the metallic hydrogen–helium envelope, (4) the layer of settled helium (if present), and (5) the IR core). In constructing our models, we used the composition of the condensate IR2 = (NH₃, H₂O + R),

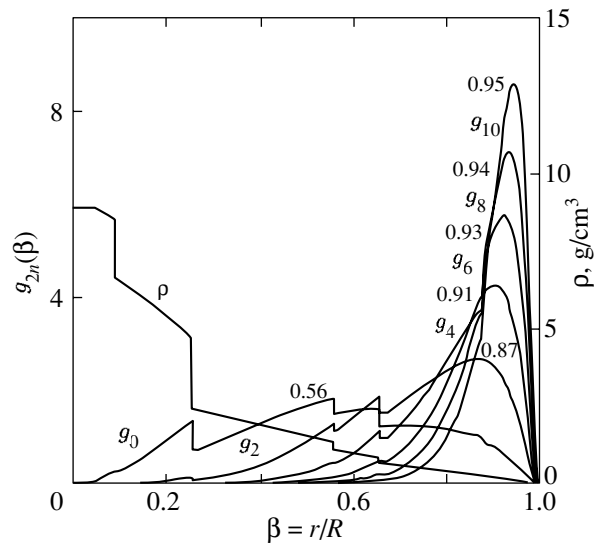


Fig. 1. Functions of the relative density of the gravitational moments $g_{2n}(\beta) = \chi_{2n}(\beta)/J_{2n}$ and the density distribution $\rho(\beta)$ for model Sa8 of Saturn. Numbers indicate the values of β at the maxima of the functions $g_{2n}(\beta)$.

$I/R = 2.2$, by assuming that carbon was in the gas phase, most likely in the form of CO. Since the helium abundance in the planetary atmosphere is uncertain, we calculated the models of Saturn with helium abundances $Y_1 = 0.06, 0.12, 0.18,$ and 0.25 . The pressure of the molecular–metallic phase transition of hydrogen with a density jump was varied between 1.5 and 3 Mbar.

We used four parameters to control the models: the mass of the planet, the gravitational moments J_2 and J_4 , and the total helium abundance in the planet Y_0 . The total helium abundance in the planet Y_0 was taken to be solar. The value of Y_0 lies within the range 0.25–0.29. The condition for the conservation of total solar helium abundance in the planet imposes constraints on the structure and composition of the outer core, which consists of the IR component settled to the core over the helium evolution time, and on the helium mass fraction in the inner molecular and metallic hydrogen–helium envelopes.

Tables 1–3 give the following model parameters for Saturn: the helium abundances in the envelopes $Y_1, Y_2,$ and Y_3 ; the total helium abundance in the planet Y_0 ; the IR mass fractions in the envelopes (Z_2, Z_3, Z_4); the pressure at the interface between the molecular hydrogen–helium layer and the metallic envelope P_m ; the pressure at the interface between the inner and outer molecular layers P_{1-2} ; the mass of the planetary core, which consists of an IR embryo and settled helium M_c ; the mass of the settled helium M_{He} (in Earth masses); the gravitational moments J_4 and

Table 1. Parameters of the models for Saturn ($Y_1 = Y_2 = Y_3$; $M_{\text{IR}} = 0.95 M_{\oplus}$ (Sa1–Sa9); $M_{\text{IR}} = 4.76 M_{\oplus}$ (Sa10–Sa15))

Model	Y_0	Y_1	Z_{2-4}	P_{1-2}	P_m	M_{He} in core	M_c (IR+He)	$-J_4 \times 10^4$	$J_6 \times 10^5$	$\Delta M/M$
Sa1	0.275	0.06	0.27	0.18	3.0	16.23	23.03	9.16	8.91	14.4
Sa2	0.276	0.06	0.23	0.12	2.0	16.95	22.82	9.20	9.02	12.5
Sa3	0.278	0.06	0.20	0.10	1.5	17.59	22.94	9.18	9.01	11.2
Sa4	0.276	0.12	0.29	0.42	3.0	12.54	18.61	9.05	8.84	14.3
Sa5	0.278	0.12	0.25	0.38	2.0	13.19	18.53	9.02	8.82	12.5
Sa6	0.277	0.12	0.23	0.40	1.5	13.38	18.32	8.98	8.77	11.4
Sa7	0.277	0.18	0.34	0.94	3.0	8.28	13.49	9.10	9.05	14.1
Sa8	0.276	0.18	0.31	1.01	2.0	8.44	13.18	9.08	9.03	12.6
Sa9	0.274	0.18	0.30	1.15	1.5	8.44	13.00	9.07	9.02	11.7
Sa10	0.271	0.12	0.25	0.29	3.0	12.02	20.78	9.20	9.02	14.8
Sa11	0.278	0.12	0.20	0.19	2.0	13.20	21.25	9.24	9.10	12.7
Sa12	0.276	0.12	0.18	0.19	1.5	13.28	20.95	9.16	9.01	11.6
Sa13	0.273	0.18	0.29	0.73	3.0	7.92	15.92	9.17	9.11	14.5
Sa14	0.273	0.18	0.25	0.73	2.0	8.25	15.76	9.15	9.09	12.8
Sa15	0.275	0.18	0.23	0.82	1.5	8.55	15.86	9.12	9.06	11.7

Table 2. Parameters of the models for Saturn ($Y_1 = Y_2$; $Y_3 = 0.25$; $M_{\text{IR}} = 0.95 M_{\oplus}$)

Model	Y_0	Y_1	Z_{2-4}	P_{1-2}	P_m	M_{He} in core	M_c (IR+He)	$-J_4 \times 10^4$	$J_6 \times 10^5$	$\Delta M/M$
SB1	0.274	0.06	0.27	0.20	3.0	13.08	18.87	9.09	8.82	14.5
SB2	0.280	0.06	0.23	0.17	2.0	12.13	16.70	9.02	8.76	12.5
SB3	0.276	0.06	0.22	0.24	1.5	10.51	14.42	8.84	8.53	11.6
SB4	0.272	0.12	0.30	0.48	3.0	9.58	14.63	8.98	8.77	14.5
SB5	0.274	0.12	0.27	0.53	2.0	8.61	12.75	8.88	8.67	12.8
SB6	0.279	0.12	0.25	0.62	1.5	8.41	12.16	8.82	8.61	11.5
SB7	0.275	0.18	0.35	1.02	3.0	6.47	10.90	9.07	9.03	14.2
SB8	0.274	0.18	0.33	1.19	2.0	5.88	9.73	9.04	9.00	12.8
SB9	0.270	0.18	0.34	1.49	1.5	5.17	8.79	9.00	8.97	12.2

J_6 , at $J_2 = J_{2\text{obs}}$; and the mass of the hydrogen–helium component that was lost during the formation of the planet $\Delta M/M$ (and that did not enter into its composition). The relationship between the model values of J_4 and the total helium abundance in the planet Y_0 is shown in Fig. 2, with the model values of J_2 satisfying the observational data.

Parameters of the homogeneous (in helium) models for Saturn ($Y_1 = Y_2 = Y_3$) are given in Table 1. In our models, we took the IR abundance in the inner molecular envelope to be equal to the IR abundance in the metallic zone, $Z_2 = Z_3$. The IR2 abundance in the inner molecular and metallic envelopes, $Z_2 = Z_3$, was varied between 0.18 and 0.34 to satisfy the

Table 3. Parameters of the models for Saturn ($Y_2 = Y_3 = 0.25$; $M_{IR} = 0.95M_{\oplus}$)

Model	Y_0	Y_1	Z_{2-4}	P_{1-2}	P_m	M_{He} in core	M_c (IR+He)	$-J_4 \times 10^4$	$J_6 \times 10^5$	$\Delta M/M$
Sc1	0.279	0.06	0.30	0.53	3.0	7.12	11.12	8.70	8.34	14.3
Sc2	0.275	0.06	0.27	0.55	2.0	6.92	10.42	8.65	8.29	12.8
Sc3	0.276	0.06	0.25	0.57	1.5	7.20	10.55	8.63	8.26	11.7
Sc4	0.278	0.12	0.32	0.75	3.0	6.51	10.53	8.85	8.63	14.2
Sc5	0.282	0.12	0.28	0.76	2.0	7.00	10.67	8.81	8.60	12.4
Sc6	0.272	0.12	0.28	0.88	1.5	6.47	9.93	8.76	8.56	11.9
Sc7	0.279	0.18	0.36	1.17	3.0	5.55	9.63	9.04	9.00	14.1
Sc8	0.279	0.18	0.33	1.26	2.0	5.77	9.56	9.03	8.99	12.5
Sc9	0.274	0.18	0.33	1.44	1.5	5.53	9.20	9.02	8.99	12.0

gravitational potential J_4 . The selection of models of this type is illustrated by Fig. 2a. The figure shows the models that satisfy the gravitational moment J_2 . The models enclosed in the square highlighted by solid lines also satisfy the gravitational moment J_4 and the total helium abundance in the planet Y_0 .

For $Y_1 = 0.06, 0.12$, and 0.18 , we considered two more types of models. Since the helium abundance in the atmosphere of Saturn was assumed to be lower than its solar value, the helium abundance in the inner envelopes must be slightly higher ($Y_1 = Y_2, Y_3 > Y_{1,2}$ (Table 2) and $Y_2 = Y_3 > Y_1$ (Table 3)). The values of Y_2 and Y_3 were taken to be equal to 0.25 , which is slightly higher than the abundance of helium that can dissolve in metallic hydrogen ($Y \approx 0.21$; Hubbard *et al.* 2002). However, these models may be considered to be extreme. The parameters of the model with Y_2 and $Y_3 < 0.25$ lie between their values for the models in Table 1 and Tables 2 and 3. At present, it is not possible to give preference to a particular model.

In the models with similar values of J_4 and Y_0 , decreasing the hydrogen metallization pressure P_m (3, 2, 1.5 Mbar) slightly reduces the IR abundance from the second to the fourth layers ($Z_2 = Z_3 = Z_4$) and decreases the mass of the hydrogen–helium component lost during the formation of the planet.

If all of the hydrogen–helium component entered into the composition of the planet, then its mass would be

$$Mq_R = \frac{Z_{\text{H}_2\text{-He}}}{Z_R},$$

where Mq_R is the mass of the R component in the planet; Z_R and $Z_{\text{H}_2\text{-He}}$ are the cosmic abundances of the R and $\text{H}_2 + \text{He}$ components, respectively; and M

is the mass of the planet. The mass of the hydrogen–helium component that entered into the composition of the planet is $q_{\text{H}_2\text{-He}}M$. Thus,

$$\Delta M = q_R M \frac{Z_{\text{H}_2\text{-He}}}{Z_R} - q_{\text{H}_2\text{-He}}M,$$

or

$$\frac{\Delta M}{M} = q_R \frac{Z_{\text{H}_2\text{-He}}}{Z_R} - q_{\text{H}_2\text{-He}}.$$

We see from Tables 1–3 that Saturn was $\sim 11\text{--}15$ planetary masses short compared to the solar composition. Thus, this planet must have been formed according to Schmidt’s scenario, through the formation of embryonic nuclei, rather than according to Laplace’s scenario. The masses of the embryonic IR nuclei for Saturn lie within the range $(3.5\text{--}8) M_{\oplus}$ ($M_{\oplus} = 5.974 \times 10^{27}$ g is the Earth’s mass).

Some uncertainty in the choice of models remains. Most of the models under consideration fit all of the available observational data. The trial models with a reduced pressure, $P_m = 2, 1.5$ Mbar, are schematically shown in Fig. 3.

The Cassini–Huygens space mission in 2004 may give answers to some of the questions concerning the interior-structure models.

FREE OSCILLATIONS OF SATURN

The Models

We chose models Sa5, Sa7, Sa8, Sa9, Sa14, and Sa8a from the large set of models constructed in the first part of our paper. They differ in core structure, in pressure of the hydrogen transition to the metallic state, and in helium abundance in the hydrogen–helium envelope (Sa8a is similar to Sa8 but the transition to the metallic state is continuous for it). Parameters of these models (the pressure at the interface

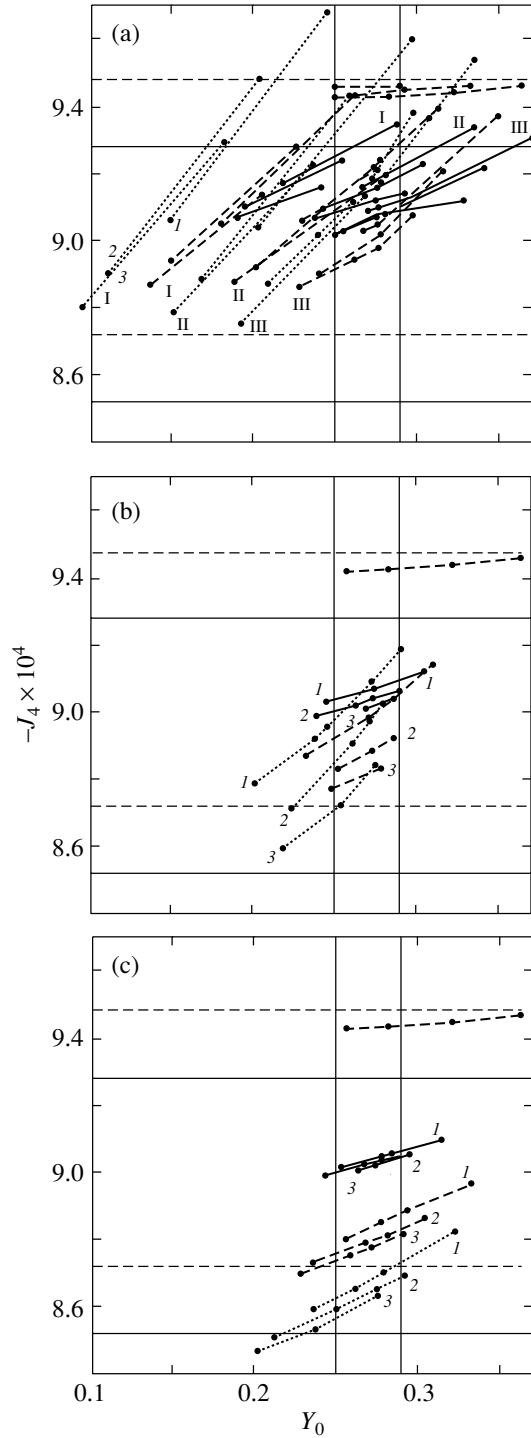


Fig. 2. Relations between the model values of J_4 and the total helium abundance in the planet Y_0 for various models of Saturn (with $J_2 = J_{2\text{obs}}$): (a) $Y_1 = Y_2 = Y_3$; (b) $Y_1 = Y_2$; $Y_3 = 0.25$; (c) $Y_2 = Y_3 = 0.25$; $M_{q(1R)} = 0.1$ (I), 0.05 (II), 0.01 (III); $P_m = 3$ (1), 2 (2), and 1.5 Mbar (3); $Y_1 = 0.06$ (dotted lines), $Y_1 = 0.12$ (dashed lines), $Y_1 = 0.18$ (solid lines), and $Y_1 = 0.25$ (dash-dotted lines). The horizontal lines indicate the scatter in the observed values of J_4 with (solid lines) and without (dashed lines) an allowance made for differential rotation; the vertical lines indicate the range of the presumed solar helium abundance.

between the molecular hydrogen–helium layer and the metallic envelope P_m , the discontinuity boundaries β_i , the densities ρ for them, and the characteristic frequency ν_0) are given in Table 4.

The distributions of density ρ , gravity g , temperature T , and speed of sound c along the dimensionless radius for models Sa5 and Sa8 are shown in Fig. 4. The distribution of relative mass $q = M(r)/M$ is shown in Fig. 5.

When the high-frequency free-oscillation spectrum is studied, the interior-structure model of Saturn must be supplemented with an atmospheric model for pressures below 1 bar.

We used the pressure–temperature profile from Appleby and Hogan (1984) to construct a seismic model of the atmosphere. The altitude and density were calculated for plane-parallel atmospheric layers with a homogeneous composition by using the van der Waals equation of state. At a 1-bar level, we imposed the requirement that the pressure, the density, and the speed of sound be continuous.

Methods of Calculation

Long-period oscillations. We calculated the free oscillations in the zeroth approximation. In this approximation, a nonrotating planet is spherical in shape. For free oscillations, the components of the displacement vector $u = (u, v, w)$, the dilatation $\Delta = \text{div}u$, and the perturbation of the gravitational potential ψ can be written in spherical coordinates (r, θ, φ) as (Alterman *et al.* 1959)

$$\begin{aligned} u &= U(r)S_n^m(\theta, \varphi), & \Delta &= X(r)S_n^m(\theta, \varphi), \\ v &= V(r)\frac{\partial}{\partial\theta}S_n^m(\theta, \varphi), & \psi &= P(r)S_n^m(\theta, \varphi), \\ w &= \frac{V(r)}{\sin\theta}\frac{\partial}{\partial\varphi}S_n^m(\theta, \varphi), \end{aligned}$$

where the factor $e^{i\sigma t}$ is omitted.

In this case, the problem reduces to a boundary-value eigenvalue problem for a homogeneous system of four linear ordinary differential equations (Alterman *et al.* 1959):

$$\begin{aligned} \dot{y}_1 &= -\frac{2}{r}y_1 + \frac{1}{K}y_2 + \frac{n(n+1)}{r}y_0, & (1) \\ \dot{y}_2 &= -\left(\sigma^2\rho + \frac{4\rho g}{r}\right)y_1 + \frac{n(n+1)\rho g}{r}y_0 - \rho y_4, \\ \dot{y}_3 &= 4\pi G\rho y_1 + y_4, \\ \dot{y}_4 &= -\frac{4\pi G\rho n(n+1)}{r}y_0 + \frac{n(n+1)}{r^2}y_3 - \frac{2}{r}y_4, \end{aligned}$$

where

$$y_0 = \frac{1}{r\sigma^2} \left(gy_1 - \frac{1}{\rho}y_2 - y_3 \right).$$

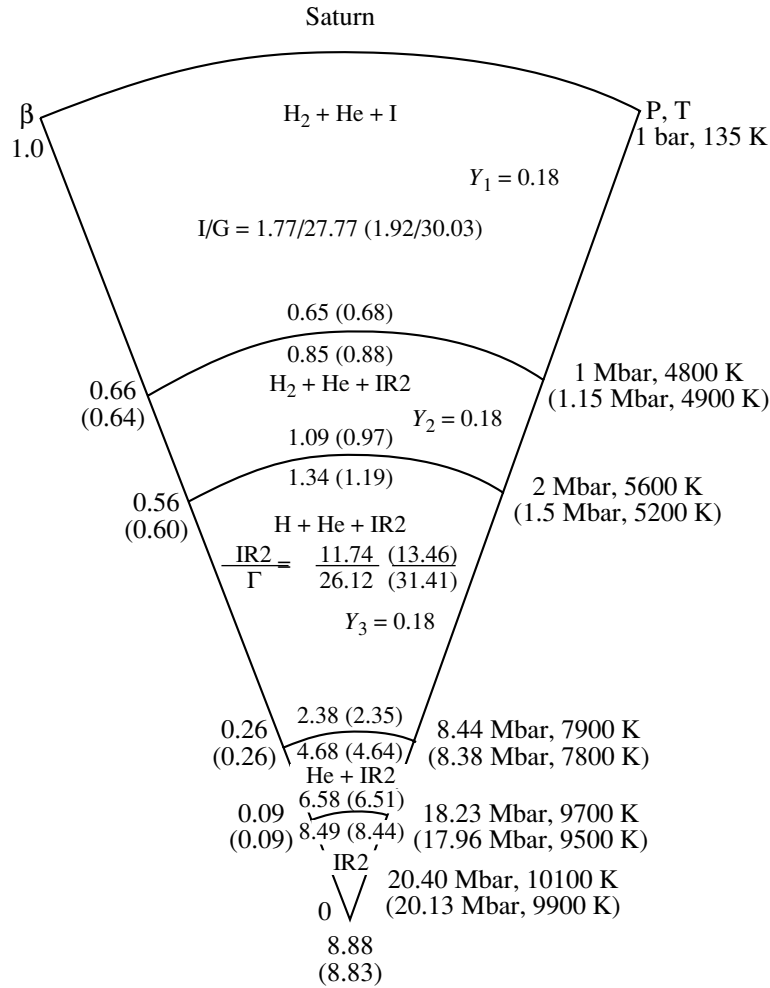


Fig. 3. A scheme of models Sa8 (2 Mbar) and Sa9 (1.5 Mbar) for Saturn. The values in parentheses correspond to model Sa9. The pressure P , temperature T , and density ρ (g cm^{-3}) are given at the interface (relative radius β) and at the center. The $I(IR)/G$ ratios and the helium abundances in the envelopes are also given. The numerical values of the G , I , and R components are in Earth masses.

All of the quantities must be finite at the coordinate origin; the boundary conditions at the surface are

$$y_4 + \frac{n+1}{R}y_3 = 0, \quad y_2 = 0 \quad (r = R),$$

where R is the radius of the planet, $K = \frac{1}{\rho} \frac{\partial P}{\partial \rho}$ is the adiabatic modulus of compressibility, $y_1 = U$, $y_2 = KX$, $y_3 = P$, $y_4 = \dot{P} - 4\pi G\rho U$, and $y_0 = V$.

The problem reduces to dimensionless variables and can be solved by numerical integration using the fourth-order Runge–Kutta iteration method. The interior-structure models are represented by 150 points with a dense grid near the surface. At any other point, the density ρ , the gravity g , and the adiabatic modulus of compressibility K can be determined by linear interpolation. To remove the singular point $r = 0$, we expanded the two linearly independent regular solutions in its vicinity into a power

series of $\beta = r/R$ (Vorontsov and Zharkov 1978). We calculated two linearly independent solutions from the center of the planet and two from its surface. They were then joined at an arbitrary surface.

The oscillations are classified by three indices (l, m, n). In the zeroth approximation, the structure of the theoretical free-oscillation spectrum is determined by the adiabatic structure of the planet and by the presence of radial density discontinuities. The free-oscillation spectrum consists of fundamental oscillation modes as well as acoustic and gravitational modes.

For an oscillation with a degree l , ${}_0S_l$ denotes the fundamental tone, and ${}_nS_l$ denotes the acoustic overtone with a radial order n . For nonradial oscillations ($l \neq 0$), at each l there are also four gravitational modes (by the number of density discontinuities in the model) with maximum amplitudes at the density discontinuities. Since the model structure is adiabatic

Table 4. Parameters of the models for Saturn

Parameters	Sa5	Sa7	Sa8	Sa9	Sa14
P_m , Mbar	2.0	3.0	2.0	1.5	2.0
β :					
IR/He+IR	0.09	0.09	0.09	0.09	0.16
He+IR/H+He+IR	0.29	0.26	0.26	0.26	0.27
H+He+IR/H ₂ +He+IR	0.56	0.49	0.56	0.60	0.56
H ₂ +He+IR/H ₂ +He+I	0.78	0.67	0.66	0.64	0.70
ρ , g cm ³ :					
at center	9.09	9.00	8.88	8.83	9.51
IR/He+IR	8.70/6.63	8.61/6.78	8.49/6.58	8.44/6.51	8.05/6.02
He+IR/H+He+IR	4.23/2.01	4.77/2.46	4.68/2.38	4.64/2.35	4.44/2.19
H+He+IR/H ₂ +He+IR	1.22/0.98	1.61/1.29	1.34/1.09	1.19/0.97	1.26/1.02
H ₂ +He+IR/H ₂ +He+I	0.53/0.43	0.83/0.63	0.85/0.65	0.88/0.68	0.70/0.57
ν^a , μHz	112	113	113	113	113

^a The values were corrected for the troposphere (Mosser *et al.* 1994).

throughout the volume, the possible gravitational oscillations are exhausted by these four modes.

For a spherical nonrotating planet, the spectrum is degenerate in m , and all of the $(2l + 1)$ frequencies $n\sigma_l^m$ for fixed l and n and different m are equal. In the case of slow rotation, each eigenfrequency is a multiplet of $2l + 1$ lines. In the first approximation, for rigid-body rotation, we take into account only the Coriolis forces; the free-oscillation eigenfrequencies (l, n) (and, accordingly, periods T) are defined by the relation (Pekeris *et al.* 1961; Backus and Gilbert 1961)

$$\sigma^m(l, n) = \sigma_0(l, n) + m\tau(l, n)\Omega, \quad -l \leq m \leq l, \quad (2)$$

where

$$\tau(l, n) = \frac{\int_0^R \rho r^2 (2UV + V^2) dr}{\int_0^R \rho r^2 [U^2 + l(l+1)V^2] dr} \quad (3)$$

and Ω is the angular velocity of the planet.

To study the oscillation pattern in more detail, we determined the kinetic energy ${}_0E_{k_l}$ from the calculated eigenfunctions. The corresponding functional is (Zharkov *et al.* 1968)

$${}_0E_{k_l} = \int_0^R \rho r^2 [U^2 + l(l+1)V^2] dr. \quad (4)$$

High-frequency acoustic oscillations. The high-frequency acoustic oscillation modes may be considered as a superposition of internal acoustic waves trapped in the planetary interiors. As the frequency increases, the reflection of these waves from outer layers of the planet is accompanied by their penetration into higher atmospheric layers. At even higher frequencies, the acoustic waves penetrate through the tropopause and escape into the upper atmosphere. Therefore, as the frequency increases, the atmospheric structure not only begins to significantly affect the free-oscillation frequencies but also places an upper limit on the frequencies of the oscillations that can be actually observed. The expected upper limit for the acoustic oscillation frequencies of Saturn is ≈ 2 mHz (Mosser *et al.* 1994).

Low-degree oscillations are of paramount interest in studying the theoretical oscillation spectrum. The detection of such oscillations is most likely, because they can be recorded when Saturn is observed as a star (without spatial resolution).

An echelle diagram is used to present the numerically calculated oscillation frequencies.

According to the asymptotic theory, the acoustic-mode frequencies $\nu_{n,l}$, to a first approximation, are proportional to the characteristic frequency ν_0 :

$$\nu_{n,l} \approx \left(n + \frac{1}{2}\right) \nu_0. \quad (5)$$

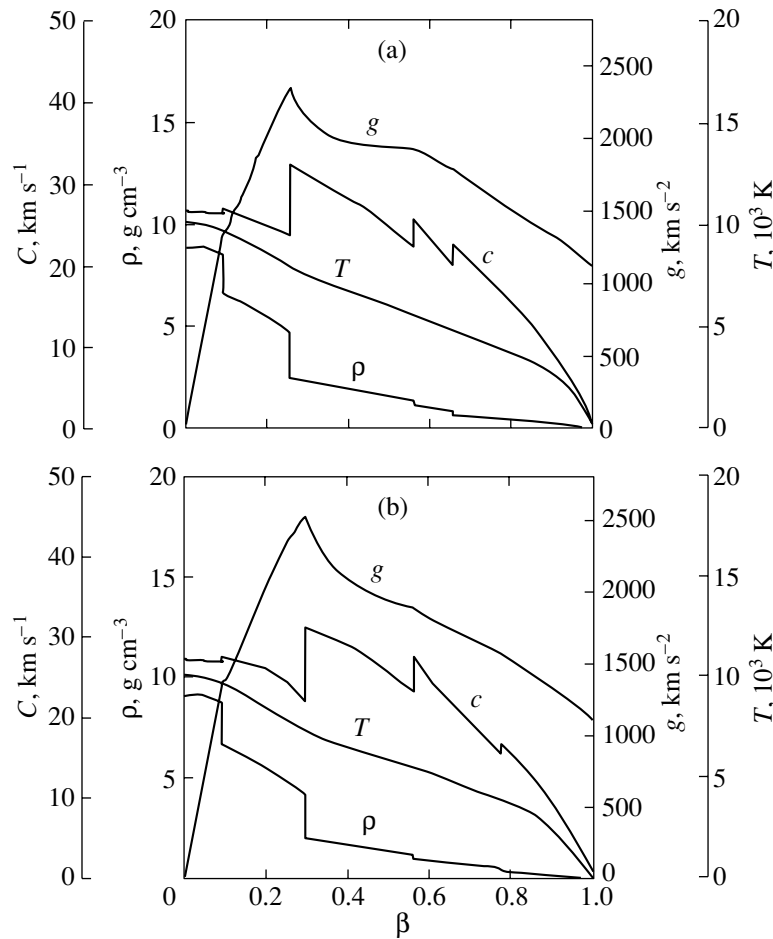


Fig. 4. Distributions of density (g cm^{-3}), gravity g (cm s^{-2}), temperature T , and speed of sound c (km s^{-1}) along the dimensionless radius $\beta = r/R$ for two extreme cases, models Sa8 (a) and Sa5 (b).

The asymptotic approximation holds for low degrees l and large radial orders n ($n \gg l$). To a first approximation, the frequencies of the oscillations with equal values of $n + l/2$ coincide; at a fixed l , the frequencies are equidistant in n with an interval of ν_0 ; and the frequencies with odd l are midway between the frequencies with even l .

The characteristic frequency (equidistance) is defined by the formula

$$\nu_0 = \left[2 \int_0^R dr/c(r) \right]^{-1}, \quad (6)$$

where $c(r)$ is the speed of sound. The quantity ν_0 is the reciprocal of twice the sound travel time from the center to the surface of the planet: $\nu_0 = 1/(2\tau_{a0})$, $\tau_{a0} = \tau_a$ at $r = 0$, where $\tau_a = \int_r^R dr/c(r)$ is the acoustic depth. The acoustic depth is plotted against the relative radius of the planet in Fig. 5. It follows from Fig. 5 that the wave path in a $0.1R$ -thick outer layer contributes 40% to τ_{a0} . Since Saturn is an

adiabatic planet, the speed of sound squared is given by the formula

$$c^2 = \frac{dP}{d\rho}, \quad (7)$$

where P and ρ are the model pressure and density, respectively.

The characteristic frequency ν_0 is an important integrated model parameter. It is useful for a tentative, rough comparison of predictions of a particular model with acoustic-oscillation data by comparing the theoretical and observed values of ν_0 . The observed oscillation patterns make it possible to directly determine ν_0 , which corresponds to the equidistance of the modes with the same degrees but different radial orders: $\nu_0 \approx \nu_{n+1,l} - \nu_{n,l}$. The determination of ν_0 from observations would impose severe constraints on the interior-structure models. For the interior-structure models of Saturn used here, the characteristic frequency is 112–113 μHz .

For the giant planets, relation (5), which is a corollary of the asymptotic approximation, can hold only

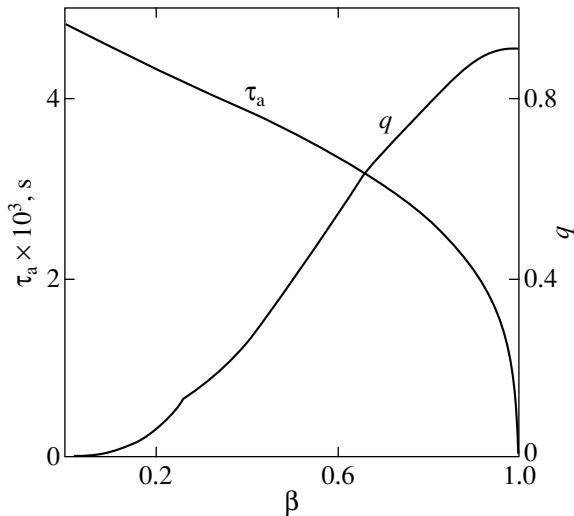


Fig. 5. Acoustic depth τ_a and relative mass $q = M(r)/M$ versus relative radius β for model Sa8.

qualitatively, because these planets have cores. The core plays an important role in the seismology of Saturn, because it causes a sharp discontinuity in the distributions of density and speed of sound. A seismological study of the giant planets could reveal the core size and structure.

The Free-Oscillation Spectra for Saturn

Figure 6 shows the radial displacement component of the fundamental mode ${}_0U_l(\beta)$ for various l from 2 to 10 and the kinetic-energy function ${}_0E_{k_l}$. The amplitudes of the radial displacement component are normalized to unity, and $\int_0^R E_{k_l}(\beta)d\beta = 1$ for the kinetic energy at all l . As l increases, the oscillations are displaced toward the surface, and the oscillation period is mainly determined by the structure of the outer regions. We see that, essentially, even the fundamental mode for $l = 2$ does not penetrate the core.

The acoustic-oscillation periods for model Sa8 of Saturn at $l \leq 8$ for the fundamental tone and overtones with radial orders from 1 to 7 are given in Table 5.

The acoustic-oscillation frequencies calculated for model Sa8 of Saturn are plotted against the degree $l \leq 15$ for the fundamental mode and overtones with radial orders from 1 to 20 in Fig. 7. Since, as was noted above, the upper limit for the acoustic-oscillation frequencies is ≈ 2 mHz, modes with frequencies above 2 mHz cannot exist.

A characteristic feature of the models under study is the presence of density discontinuities. These density discontinuities are responsible for the presence of gravitational modes with maximum amplitudes at

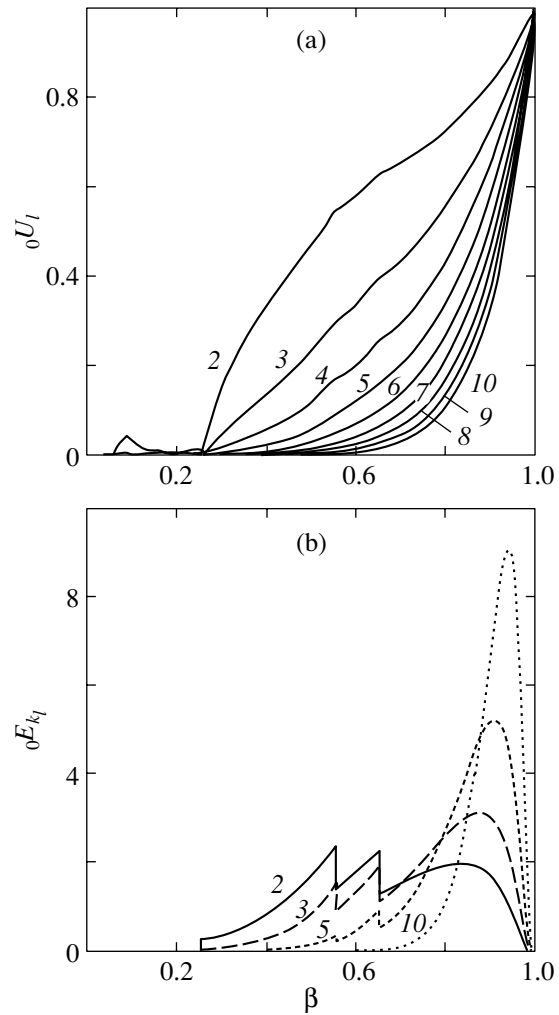


Fig. 6. Radial displacement component ${}_0U_l(\beta)$ for $l = 2-10$ (a) and kinetic energy ${}_0E_{k_l}$ for $l = 2, 3, 5, 10$ (b) versus relative radius β for model Sa8.

the discontinuity boundaries for nonradial oscillations. Since the model is adiabatic, all of the possible gravitational modes are exhausted by these so-called discontinuity modes. The modern models of Saturn being studied here have four jumps in the radial distribution of the material parameters. The first density jump is related to changes in chemical composition at the interface between the outer and inner molecular layers, while the second jump is related to the molecular–metallic phase transition of hydrogen, which may be accompanied by changes in chemical composition; the deeper third and fourth jumps are also related to changes in chemical composition—at the interface between the IR core and the metallic envelope as well as at the interface between the outer and inner cores. Therefore, the free-oscillation spectrum calculated for the modern models contains four gravitational modes for each l . The oscillation periods of the gravitational modes are given in Table 6.

Table 5. The acoustic-oscillation periods of Saturn (min) for model Sa8

<i>n</i>	<i>l</i>								
	0	1	2	3	4	5	6	7	8
0			173.2	131.9	113.0	100.9	92.18	85.44	80.01
1	85.22	69.49	59.01	52.35	47.73	44.38	41.85	39.86	38.24
2	51.17	43.53	38.52	35.67	33.52	31.74	30.24	28.97	27.91
3	36.63	33.49	30.10	27.82	26.34	25.19	24.20	23.33	22.55
4	28.88	26.78	24.99	23.33	22.06	21.09	20.30	19.62	19.00
5	24.54	22.57	21.19	20.03	19.06	18.25	17.55	16.96	16.45
6	21.11	19.65	18.48	17.47	16.67	16.05	15.50	14.99	14.52
7	18.45	17.35	16.36	15.58	14.82	14.23	13.79	13.41	13.04

The periods of the gravitational modes for $l \leq 8$ for model Sa8 are plotted against l in Fig. 8.

As we see from Table 6 and Fig. 8, the oscillation periods related to the third density jump (the outer-core boundary) are systematically shorter than the periods pertaining to the fourth density jump (the inner-core boundary). The reason is that the period

of the gravitational mode depends on the radius of the discontinuity boundary and on the density at this boundary. If two layers separated by a discontinuity are extended enough, then the frequency of the gravitational mode can be roughly estimated as (Landau and Lifshitz 1959)

$$\sigma_d \approx \sqrt{l \frac{g_d (\rho_- - \rho_+)}{r_d (\rho_- + \rho_+)}}$$

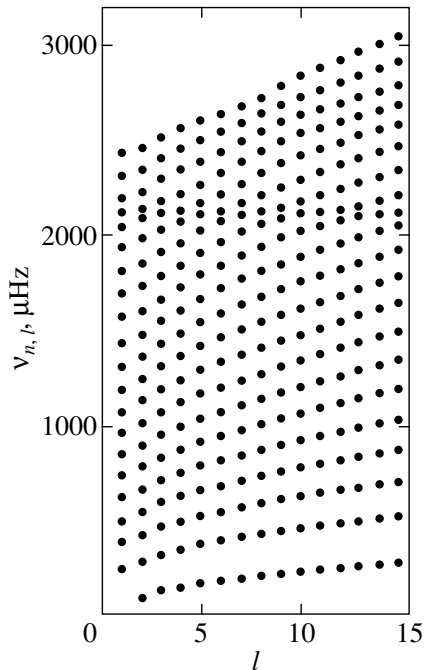


Fig. 7. Acoustic-oscillation frequencies for model Sa8 of Saturn versus degree $l \leq 15$ for the fundamental tone and overtones with radial orders from 1 to 20.

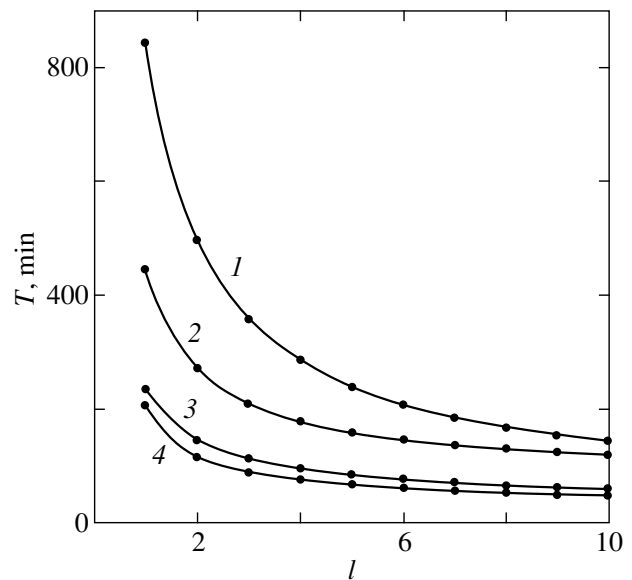


Fig. 8. The periods of the gravitational modes related to density discontinuities versus degree l : (1) $\beta = 0.64-0.78$; (2) $\beta = 0.56-0.614$; (3) $\beta = 0.26-0.29$; (4) $\beta = 0.09-0.16$.

Table 6. The oscillation periods of gravitational modes (min)

Degree	Sa5	Sa7	Sa8	Sa8a	Sa9	Sa14
$l = 1$		643.3	845.1	845.1	1321	862.7
		425.6	445.9	—	437.2	483.7
		205.7	206.7	206.7	207.0	197.2
		240.8	235.9	235.9	234.7	220.6
$l = 2$	541.7	381.5	497.1	497.1	768.8	508.5
	314.4	264.8	274.1	—	265.8	299.8
	114.6	114.2	114.9	114.9	115.1	106.2
	140.1	148.5	145.2	145.2	144.4	136.0
$l = 3$	394.0	279.6	360.0	360.0	549.2	369.8
	243.6	206.9	210.9	—	201.5	232.9
	88.94	89.32	89.77	89.77	89.91	84.30
	108.5	115.3	112.8	112.8	112.2	105.5
$l = 4$	316.0	225.9	286.6	286.6	430.3	296.2
	207.2	178.2	179.4	—	168.8	199.1
	75.49	76.04	76.37	76.37	76.47	72.45
	91.88	97.73	95.72	95.72	95.19	89.47
$l = 5$	268.4	193.0	240.8	240.8	355.7	251.1
	184.6	160.7	160.7	—	149.3	178.5
	66.79	67.38	67.63	67.63	67.71	79.38
	81.31	86.58	84.83	84.83	84.38	64.48
$l = 6$	236.6	171.0	209.7	209.7	304.4	220.8
	168.6	148.3	148.3	—	136.2	164.2
	60.56	61.15	61.36	61.36	61.43	58.63
	73.84	78.69	77.12	77.12	76.71	72.23
$l = 7$	213.9	155.1	187.1	187.1	267.0	199.3
	156.4	138.8	139.2	—	126.7	153.3
	55.82	56.39	56.58	56.58	56.64	54.11
	68.19	72.71	71.26	71.26	70.88	66.79
$l = 8$	196.9	143.2	169.9	169.9	238.5	183.2
	146.5	130.9	132.1	—	119.5	144.5
	52.05	52.60	52.76	52.76	52.82	50.50
	63.70	67.96	66.59	66.59	66.24	62.45
$l = 9$	183.7	133.9	156.5	156.5	216.1	170.7
	138.4	124.2	126.2	—	113.6	137.1
	48.95	49.49	49.64	49.64	49.68	47.52
	60.01	64.05	62.75	62.75	62.42	58.86
$l = 10$	173.0	126.4	145.6	145.6	198.0	160.7
	131.4	118.4	121.3	—	108.8	130.6
	46.35	46.87	47.01	47.01	47.05	45.02
	56.91	60.75	59.52	59.52	59.21	55.84

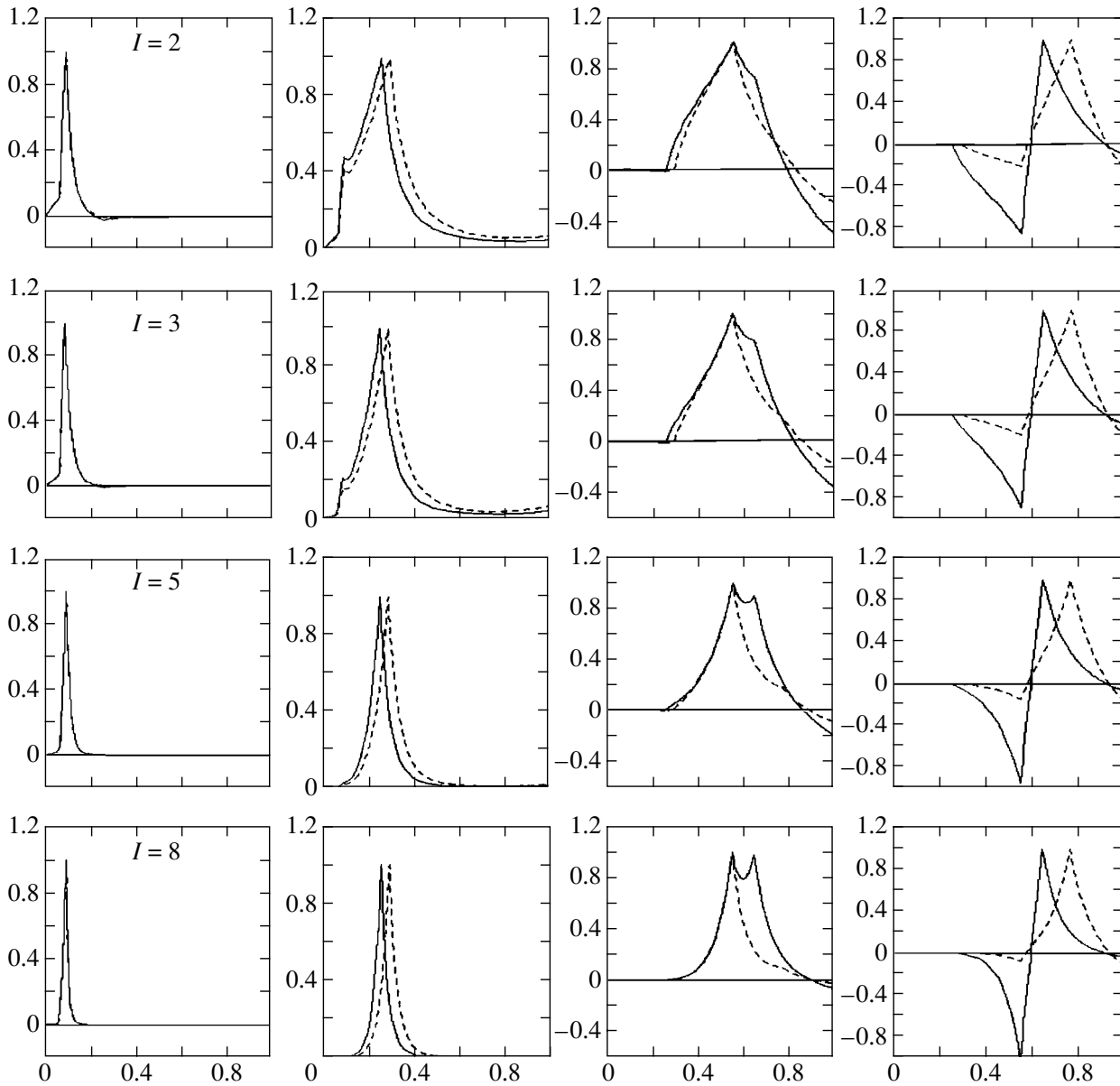


Fig. 9. The eigenfunctions of Saturn's oscillations for models Sa8 (solid lines) and Sa5 (dashed lines) (the gravitational modes $l = 2, 3, 5, 8$). The dimensionless radius β is along the horizontal axes. The normalized radial displacement amplitudes $\delta U_l(\beta)$ are along the vertical axes. Each gravitational mode reaches its maximum amplitude at the radial density jump. The discontinuity modes are determined by the density jumps at $\beta = 0.09, 0.26, 0.56,$ and 0.66 . The oscillation periods are given in Table 6.

where ρ_{\pm} is the density at the discontinuity, $\rho_- > \rho_+$, g_d is the local gravity at the discontinuity, and r_d is the distance from the discontinuity to the center of the planet (Table 4).

Figure 9 shows the eigenfunctions of the radial displacements of Saturn's oscillations (gravitational modes) with $l = 2, 3, 5,$ and 8 . We see that the radial distribution of the displacements for higher degrees l have the same structure as the quadrupole oscillations; as l increases, the displacements in oscillations concentrate toward the physical boundaries

(density jumps). An important feature of the gravitational modes related to the interfaces at $\beta = 0.66$ and 0.56 is that they have appreciable radial displacement amplitudes at the surface (Fig. 9) and appreciably longer periods (Table 6) than those for the fundamental acoustic mode (Table 5). If the molecular-metallic phase transition of hydrogen is continuous rather than discontinuous, as in model Sa8a, then the corresponding gravitational mode in the free-oscillation spectrum of Saturn will be absent (Table 6). If, however, there is a jump in the chemical

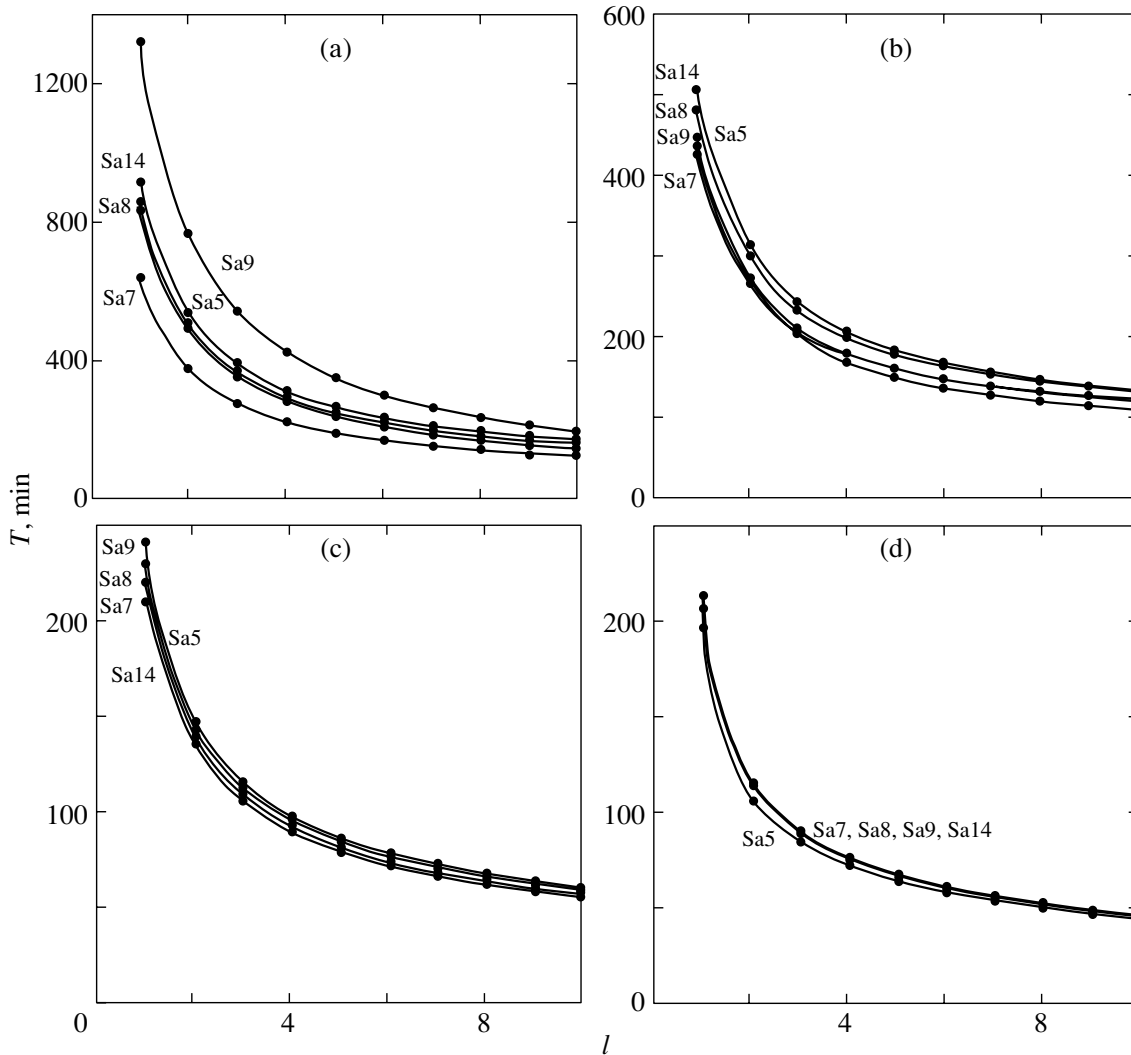


Fig. 10. The periods of the gravitational modes for Saturn's models (Sa5, Sa7, Sa8, Sa9, Sa14) versus l : $\beta =$ (a) 0.64–0.78; (b) 0.56–0.61; (c) 0.26–0.29, (d) 0.09–0.16.

composition when hydrogen is metallized in the interiors of Saturn, as in models Sa5, Sa7, Sa8, Sa9, and Sa14, then the corresponding gravitational mode is retained. The periods of the gravitational modes for models Sa5, Sa7, Sa8, Sa9, and Sa14 are plotted against l in Fig. 10.

Echelle diagrams are commonly used to compare the theoretical and observed frequencies. For low-degree ($l = 0, 1, 2, 3, 4, 6$) acoustic modes, we calculated these diagrams for three models of Saturn (Fig. 11).

The echelle diagrams for Saturn's models form no vertical lines, because the frequency spectrum of low degrees l is strongly affected by the planetary core structure (the low-degree modes have eigenfunctions that extend deep into the core and are severely distorted by the core and the density discontinuities). As

a result, as was noted above, the asymptotic approximation becomes virtually inapplicable.

Resonance phenomena in the core of Saturn are responsible for the irregular (at first glance) behavior of the curves in Fig. 11. As a result, the shape of these curves proves to be sensitive to the core size and structure (Fig. 11a— $M_c(\text{IR} + \text{He}) = 15.76M_\oplus$, $M_c(\text{IR}) = 7.51M_\oplus$, Fig. 11b— $M_c(\text{IR} + \text{He}) = 13.18M_\oplus$, $M_c(\text{IR}) = 4.74M_\oplus$, Fig. 11c— $M_c(\text{IR} + \text{He}) = 9.56M_\oplus$, $M_c(\text{IR}) = 3.79M_\oplus$). For Sa8 (Fig. 11b), the curves tend to approach one another; for Sa14 (Fig. 11a), there is a tendency for the number of intersections to increase.

We see that for low degrees and high radial orders, there are intersections between acoustic modes with different l , which makes it difficult to correctly identify the observed frequencies.

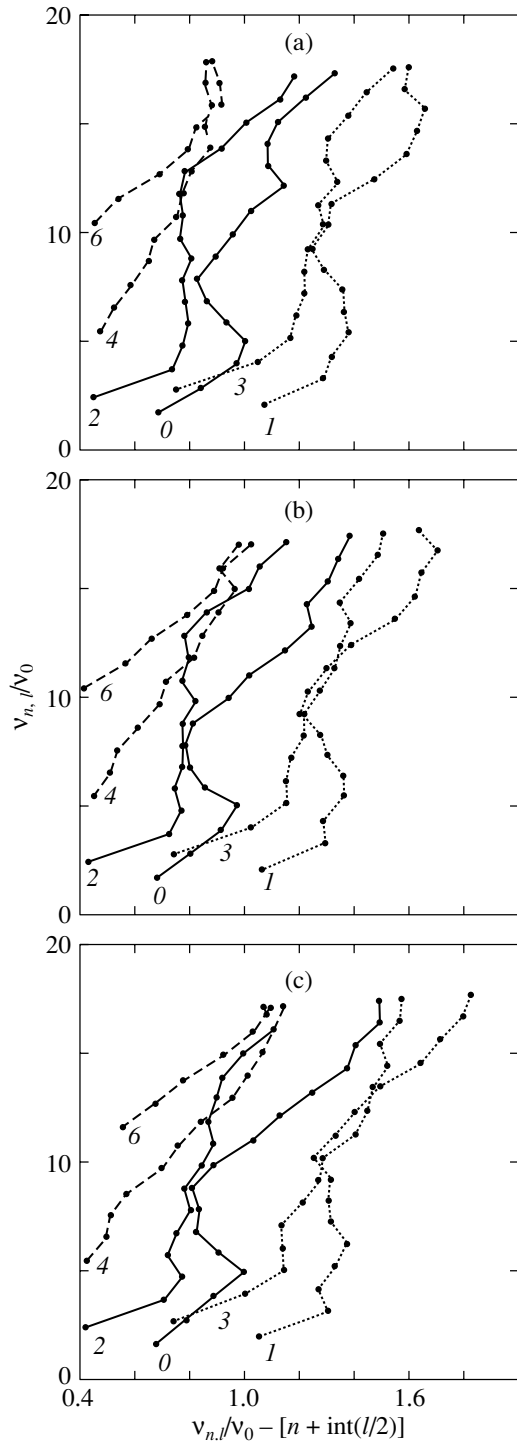


Fig. 11. Echelle diagrams for the acoustic-oscillation frequencies of Saturn for models Sa14 (a), Sa8 (b), and Sc8 (c) ($l = 0, 2$ —solid lines; $l = 1, 3$ —dotted lines; $l = 4, 6$ —dashed lines).

Estimating the Free-Oscillation Energy

We calculated the kinetic energies of various modes (see Eq. (4)) by taking the oscillation amplitude to be equal to 1-m at the planetary surface. The

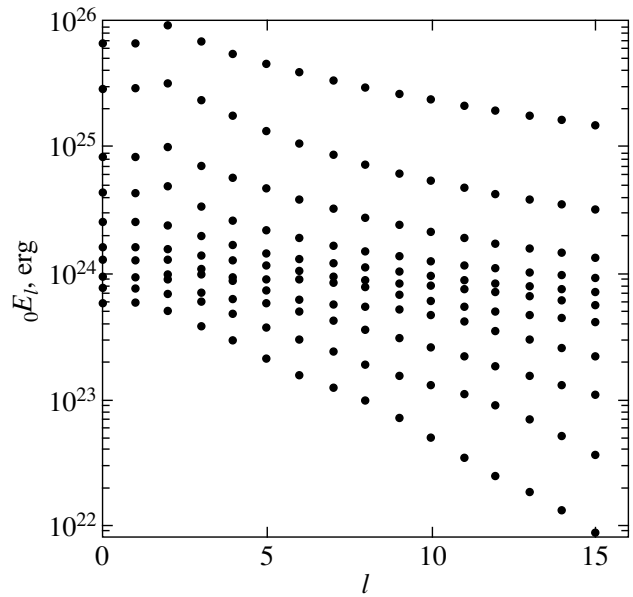


Fig. 12. The period-averaged energy of the acoustic oscillations for the fundamental mode and 10 overtones versus oscillation degree $l \leq 15$ for model Sa8. The oscillation amplitude was taken to be 1 m at the planetary surface.

period-averaged kinetic energies for the fundamental mode and 10 overtones are plotted against degree $l \leq 15$ in Fig. 12.

The energy of the fundamental mode ${}_0S_2$ is large, 9.3×10^{25} erg, being only five orders of magnitude lower than the total annual heat flux from the planetary interiors (Hanel *et al.* 1983)

$$q_{t,S} \approx 9 \times 10^{23} \text{ erg s}^{-1} \approx 2.8 \times 10^{31} \text{ erg yr}^{-1}.$$

As we see from Fig. 12, the energy of the fundamental mode ${}_0S_{15}$ is approximately an order of magnitude lower than the energy of the ${}_0S_2$ mode. For the ${}_nS_l$ overtones, the energy decreases faster with increasing l . The energy needed to excite free oscillations is much lower than the annual heat flux.

Let us estimate the lifetime of the eigenmodes if they are excited. The value of the dissipative factor for Saturn is very high for tidal periods, $Q_S \geq 1.4 \times 10^4$ (Gavrilov and Zharkov 1977). In the range of free-oscillation periods, this value can be lower. To estimate the lifetime, we assume that Q_S ranges from 10^3 to 10^5 for free-oscillation periods. The oscillation amplitudes decrease as $A = A_0 e^{-\sigma t / 2Q_S}$. Assuming that $Q_S \approx 10^3 - 10^5$, we obtain the lifetime $t = 2Q_S / \sigma \approx 1.8 \times (10^6 - 10^8)$ s for the fundamental mode ${}_0S_2$. This lifetime is slightly shorter than that for the other modes. We see that the lifetime of such oscillations is estimated to be in the range from several months to a year. Note that the Earth's radial oscillations with a very high Q are observed for a month.

Rotation Effects

As we noted above, all of the rotation effects were considered in detail by Vorontsov and Zharkov (1981a, 1981b) and Vorontsov (1981). The corrections for the Coriolis forces (in the second approximation) and ellipticity (in the first approximation) were calculated for the three-layer models of Saturn that were constructed by Zharkov *et al.* (1974a, 1974b). These corrections can also be used for modern models. Vorontsov and Zharkov (1981a, 1981b) concluded that the effect of mode coupling on the spectrum is negligible. The frequency differences do not exceed 0.5%, which is much smaller than the corrections for the second-order rotation effects. The corrections for mode coupling to the eigenfunctions are no larger than a few percent. This fact shows that, despite the rapid rotation of the planet, the classification of the free-oscillation spectrum by indices (l, n, m) is valid.

The free-oscillation spectrum of Saturn (the fundamental tone and the first overtones), which is split by the rotation of the planet (because of the Coriolis forces) and calculated by using the first-order perturbation theory, is shown in Fig. 13a. The overtones are virtually unsplit. The values of $\tau(l, n)$ calculated from formula (3) are given in Table 7.

Figure 13b shows the free-oscillation spectrum of Saturn corrected for the second-order rigid-body rotation effects (Vorontsov and Zharkov 1981a). The multiplets of the fundamental tones are subjected to the largest splitting by rotation. At low l , the rotation effect is mainly determined by the Coriolis forces. These forces decelerate the waves that travel in the direction of rotation ($m < 0$), causing the period to increase, and accelerate the oppositely traveling waves ($m > 0$). The asymmetry in multiplets increases with l . For high l , the ellipticity of the planet mainly contributes to the splitting.

Figure 13c shows the effect of differential rotation on the free-oscillation spectrum (Vorontsov 1981). This spectrum was calculated using a simple model distribution of differential rotation with cylindrical symmetry,

$$\Omega(r, \theta) = \Omega_0 \left[1 + 0.1 \left(\frac{r}{R} \sin \theta \right)^2 \right]. \quad (8)$$

This model distribution differs from the model of differential rotation Hubbard (1982), but, in general, Eq. (8) describes the observed increase in the angular velocity toward the equator.

Figure 13c provides a qualitative insight into the influence of differential rotation on the free-oscillation spectrum of Saturn (the results are given in a coordinate system that rotates with an angular velocity Ω). Having the strongest effect on the fundamental

tones, differential rotation generally compresses the multiplets compared to the splitting for rigid-body rotation. Relative to the rotating frame of reference used, the outer equatorial regions of the differentially rotating planet have a small excess rotation. As a result, the waves that travel in the direction of rotation ($m < 0$) accelerate, while the oppositely traveling waves ($m > 0$) decelerate. As l increases, differential rotation affects the spectrum more strongly, because the oscillations are pushed toward the surface, where the rotation nonuniformity is at a maximum.

In principle, the free-oscillation method allows the differential rotation in the interiors of Saturn to be determined.

DISCUSSION AND CONCLUSIONS

We have calculated a theoretical free-oscillation spectrum for the latest models of Saturn, each of which fits all of the available observational data. The results of our calculations are presented in sufficient detail graphically and in tables.

Of particular interest are the diagnostic potentialities of the discontinuity modes related to density jumps in the molecular envelope of Saturn and at the interface between its molecular and metallic envelopes. These two modes have nonzero displacements at the planetary surface. In Figs. 8 and 10, the periods of the discontinuity modes are plotted against degree l for model Sa8 and for all of the models studied, respectively. It follows from Fig. 8 that the $T_l = f(l)$ branches pertaining to the two outer density jumps are widely separated, and, if recorded, these discontinuity modes can be easily identified.

The results of our numerical experiments emphasize the relevancy not only of determining the periods from observations but also studying the excitation mechanisms in order to deal with the expected amplitudes of the eigenmodes.

Our modeling showed that the composition of Saturn differs markedly from the composition of the sun. More specifically, during its formation, Saturn was ~ 11 – 15 planetary masses short of the hydrogen–helium component. Saturn, as well as the other giant planets, (Zharkov 1993, 2003) must have been formed according to Schmidt's scenario, through the formation of embryonic nuclei, rather than according to Laplace's scenario. The masses of the embryonic nuclei themselves lie within the range $(3.5$ – $8) M_{\oplus}$. The corresponding values for Jupiter are 3 – $3.5 M_{\oplus}$ (Gudkova and Zharkov 1999a).

Space missions to the planets, particularly to the giant planets, have given a new impetus to the development of scenarios for the origin of the Solar system, the Earth, the planets, and their satellites. The models

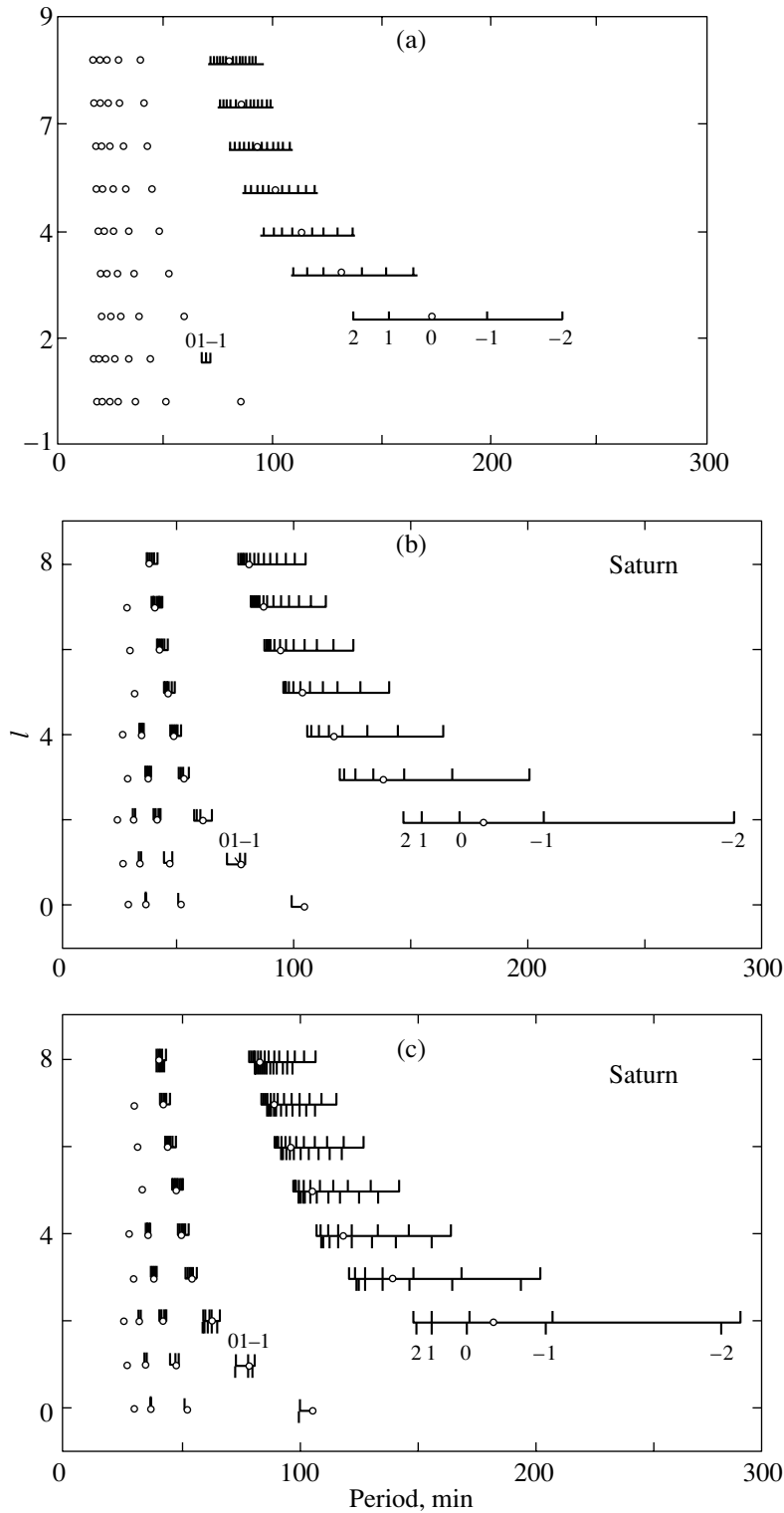


Fig. 13. Splitting of the free-oscillation spectrum for Saturn due to the rotation of the planet: (a) because of the Coriolis forces, the first-order perturbation is used for model Sa8; (b) with allowance made for the second-order rigid-body rotation effects (Vorontsov and Zharkov 1981b); and (c) with allowance made for the effect of differential rotation (Vorontsov 1981). The circles indicate the oscillation periods in the zeroth approximation. The vertical bars above the line indicate the multiplet splitting for rigid-body rotation; the vertical bars under the line (c) correspond to an allowance for the effect of differential rotation. The values of m are given near one multiplet. The results are presented for a rotating frame of reference. The fundamental tones and the first overtones are shown.

Table 7. The splitting $\tau(l, n)$ for model Sa8

n	l						
	2	3	4	5	6	7	8
	Acoustic oscillations						
0	0.481	0.323	0.245	0.197	0.165	0.142	0.124
1	0.049	0.053	0.049	0.044	0.038	0.034	0.031
2	0.017	0.017	0.018	0.020	0.020	0.019	0.018
3	0.017	0.015	0.010	0.008	0.008	0.009	0.010
	Gravitational oscillations						
$\beta = 0.09$	0.203	0.112	0.074	0.055	0.044	0.037	0.033
$\beta = 0.26$	0.280	0.162	0.113	0.086	0.069	0.057	0.049
$\beta = 0.56$	0.183	0.090	0.053	0.036	0.027	0.022	0.018
$\beta = 0.66$	0.167	0.085	0.053	0.037	0.028	0.023	0.019

constructed of the giant planets are important new boundary conditions for these problems.

The formation of the giant planets is considered in terms of two main hypotheses (Pollack 1985; Bodenheimer 1985). According to the first hypothesis, which dates back to the time of Laplace, the giant planets were formed through instability in the gas of the protosolar nebula when the nebular gas broke up into rings whose material condensed into a planet. In this case, a planet should have the same composition as the Sun. This hypothesis is in conflict with modern models of the giant planets. According to the second hypothesis, the formation of the giant planets roughly breaks down into two stages. Initially, dust grains composed of ices, silicates, iron, and its compounds combined into protobodies (planetesimals), which gradually accumulated into planetary protocores with masses of several Earth masses. These planetary embryos could have been immersed in a noticeable primordial hydrogen–helium atmosphere. As the mass of these gravitational centers reached a critical value, gravitational instability arose in the primordial gas–dust cloud and gas accretion onto the planetary protocores took place. The formation time scale of the planets is determined by the formation time of the embryos, their protocores. The second planet-formation scenario is within the framework of O.Yu. Schmidt’s cosmogonical ideas. It is often discussed in terms of the model by Mizuno (1980), according to which the critical masses of the cores of all the Jovian planets are approximately equal, being about $10\text{--}15M_{\oplus}$. However, the most recent models of the giant planets (Zharkov and Gudkova 1991; Gudkova and Zharkov 1999a; and this paper) do not confirm Mizuno’s hypothesis about approximately equal

masses $\sim 10\text{--}15M_{\oplus}$ for the embryos of all the giant planets onto which gas accretion took place. In reality, the cores of all of the giant planets are several times smaller.

Zharkov and Kozenko (1990) and Zharkov (1993) suggested a new scenario for the formation of Saturn, Uranus, and Neptune. After the formation of Jupiter in a time approximately equal to $\sim(1\text{--}2)\times 10^7$ yr, this planet began to push a massive embryo with a mass of $\sim 5M_{\oplus}$ out to the periphery of the Solar system in the direction of Saturn’s feeding zone. This embryo triggered the formation of Saturn. After the formation of Jupiter and Saturn, the embryos were pushed to the periphery in the directions of the feeding zones of Uranus and Neptune. These embryos captured the relatively small hydrogen–helium envelopes from the zones of Jupiter and Saturn to form Uranus and Neptune in a cosmogonically realistic time interval.

These ideas were further developed by Zharkov (2003). Jupiter is generally believed to be the first planet to be formed (Zharkov 1993). Before the formation of Jupiter, the feeding zones out of which the growing planets scooped protobodies could be assumed with a good approximation to be closed systems. This situation changed after the formation of Jupiter, because the protobodies from different feeding zones got mixed up under the influence of Jupiter. Zharkov (1993) pointed out that, as the embryos of Uranus and Neptune were pushed out to the periphery of the Solar system, they absorbed and scattered protobodies from distant feeding zones, some of which were absorbed by the molecular envelopes of Saturn and Jupiter. As a result, the composition of the condensate from which the embryos of these planets were formed and the composition of the condensate

in the molecular envelopes of both Jupiter and Saturn must generally be different. This circumstance makes it much more difficult to determine the composition of the IR component in the interiors of both planets. The uncertainty in the composition of the molecular envelopes must also have an effect on radiative-opacity calculations and on the identification of radiative zones in the molecular envelopes of Jupiter and Saturn.

REFERENCES

1. Z. Alterman, H. Jarosh, and C. L. Pekeris, *Proc. R. Soc. London, Ser. A* **252**, 80 (1959).
2. J. F. Appleby and J. S. Hogan, *Icarus* **59**, 336 (1984).
3. G. Backus and P. Gilbert, *Proc. Natl. Acad. Sci. USA* **47**, 362 (1961).
4. J. N. Bahcall and M. N. Pinsonneault, *Rev. Mod. Phys.* **67**, 781 (1995).
5. D. Bercovici and G. Schubert, *Icarus* **69**, 557 (1987).
6. P. Bodenheimer, in *Protostars and Planets II*, Ed. by D. C. Black and M. S. Matthews (Univ. Arizona Press, Tucson, 1985), p. 873.
7. B. J. Conrath and D. Gautier, *Icarus* **144**, 124 (2000).
8. B. J. Conrath, D. Gautier, K. A. Hanel, and J. S. Holstein, *Astrophys. J.* **282**, 807 (1984).
9. A. Dollfus, *Icarus* **12**, 1010 (1970).
10. A. B. Efimov, V. N. Zharkov, V. P. Trubitsyn, and A. M. Bobrov, *Astron. Zh.* **54**, 1118 (1977) [*Sov. Astron.* **21**, 635 (1977)].
11. D. Gautier and T. Owen, *Origin and Evolution of Planetary and Satellite Atmospheres*, Ed. by S. K. Atreya, J. B. Pollack, and M. S. Matthews (Univ. Arizona Press, Tucson, 1989), p. 487.
12. D. Gautier, B. Conrath, M. Flazer, *et al.*, *J. Geophys. Res.* **86**, 8713 (1981).
13. S. V. Gavrillov and V. N. Zharkov, *Icarus* **32**, 443 (1977).
14. T. Guillot, *Planet. Space Sci.* **47**, 1183 (1999).
15. T. Guillot, D. Gautier, G. Chabrier, and T. Mosser, *Icarus* **112**, 337 (1994).
16. T. Guillot, G. Chabrier, P. Morel, and D. Gautier, *Icarus* **112**, 354 (1994).
17. T. Guillot, D. Gautier, and W. Hubbard, *Icarus* **130**, 534 (1997).
18. T. V. Gudkova and V. N. Zharkov, *Astron. Vestn.* **22**, 66 (1996).
19. T. V. Gudkova and V. N. Zharkov, *Pis'ma Astron. Zh.* **22**, 66 (1996) [*Astron. Lett.* **22**, 58 (1996)].
20. T. V. Gudkova and V. N. Zharkov, *Astron. Vestn.* **31**, 113 (1997).
21. T. V. Gudkova and V. N. Zharkov, *Planet. Space Sci.* **47**, 120 (1999).
22. T. V. Gudkova and V. N. Zharkov, *Planet. Space Sci.* **47**, 1211 (1999).
23. T. V. Gudkova, V. N. Zharkov, and V. V. Leont'ev, *Astron. Vestn.* **22**, 252 (1988).
24. T. Gudkova, T. Mosser, J. Provost, *et al.*, *Astron. Astrophys.* **303**, 594 (1995).
25. R. A. Hanel, B. J. Conrath, V. G. Kunde, *et al.*, *Icarus* **53**, 262 (1983).
26. W. B. Hubbard, *Icarus* **52**, 509 (1982).
27. W. B. Hubbard and D. J. Stevenson, *Saturn*, Ed. by T. Gehrels and M. S. Matthews (Univ. Arizona Press, Tucson, 1984), p. 47.
28. W. B. Hubbard, V. P. Trubitsyn, and V. N. Zharkov, *Icarus* **21**, 147 (1974).
29. W. B. Hubbard, A. Burrows, and J. I. Lunine, *Ann. Rev. Astron. Astrophys.* **40**, 103 (2002).
30. L. D. Landau and E. M. Lifshits, *Fluid Mechanics* (Pergamon, Oxford, 1959).
31. U. Lee, *Astrophys. J.* **405**, 359 (1993).
32. P. Lognonne and T. Mosser, *Surv. Geophys.* **14**, 239 (1993).
33. M. S. Marley and C. C. Porco, *Icarus* **106**, 508 (1993).
34. H. Mizuno, *Progr. Theor. Phys.* **64**, 544 (1980).
35. B. Mosser, *Astron. Astrophys.* **293**, 586 (1995).
36. B. Mosser, T. Gudkova, and T. Guillot, *Astron. Astrophys.* **291**, 1019 (1994).
37. W. J. Nellis, S. T. Weir, N. C. Holms, *et al.*, *Properties of Earth and Planetary Materials at High Pressures and Temperature*, *Geophys. Monogr.* **101**, 357 (1998).
38. G. W. Null, E. L. Lau, E. D. Biller, and J. D. Anderson, *Astron. J.* **86**, 456 (1981).
39. C. L. Pekeris, Z. Alterman, and H. Jarosh, *Phys. Rev.* **122**, 1692 (1961).
40. J. B. Pollack, in *Protostars and Planets II*, Ed. by D. C. Black and M. S. Matthews (Univ. Arizona Press, Tucson, 1985), p. 791.
41. J. B. Provost, B. Mosser, and G. Beithomieu, *Astron. Astrophys.* **274**, 595 (1993).
42. D. Saumon, G. Chabrier, and H. M. Van Horn, *Astrophys. J., Suppl. Ser.* **99**, 713 (1995).
43. A. Seiff, D. B. Kirk, T. C. D. Knight, *et al.*, *Science* **272**, 844 (1996).
44. S. V. Vorontsov, *Astron. Zh.* **58**, 1275 (1981) [*Sov. Astron.* **25**, 724 (1981)].
45. S. V. Vorontsov, T. V. Gudkova, and V. N. Zharkov, *Pis'ma Astron. Zh.* **15**, 646 (1989) [*Sov. Astron. Lett.* **15**, 278 (1989)].
46. S. V. Vorontsov and V. N. Zharkov, *Astron. Zh.* **55**, 84 (1978) [*Sov. Astron.* **22**, 46 (1978)].
47. S. V. Vorontsov and V. N. Zharkov, *Usp. Fiz. Nauk* **134**, 675 (1981) [*Sov. Phys. Usp.* **24**, 697 (1981)].
48. S. V. Vorontsov and V. N. Zharkov, *Astron. Zh.* **58**, 1101 (1981) [*Sov. Astron.* **25**, 627 (1981)].
49. S. V. Vorontsov and V. N. Zharkov, *Itogi Nauki Tekh., Ser.: Astron.* **38**, 253 (1988).
50. S. V. Vorontsov, V. N. Zharkov, and V. M. Lubimov, *Icarus* **27**, 109 (1976).
51. S. Weir, A. C. Mitchell, and W. J. Nellis, *Phys. Rev. Lett.* **76**, 1860 (1996).
52. U. Von Zahn and D. M. Hunten, *Science* **272**, 849 (1996).
53. U. Von Zahn, D. M. Hunten, and G. Lehman, *J. Geophys. Res.* **103**, 22815 (1998).
54. V. N. Zharkov, *Geophys. Monograph* 74, IUGG 14, *Am. Geophys. Union* 7 (1993).

55. V. N. Zharkov, *The First O.Yu. Schmidt's Meeting, the 30 October 2002* (OIFZ RAN, Moscow, 2003), p. 102.
56. V. N. Zharkov and T. V. Gudkova, *Ann. Geophys.* **9**, 357 (1991).
57. V. N. Zharkov and A. V. Kozenko, *Pis'ma Astron. Zh.* **16**, 169 (1990) [*Sov. Astron. Lett.* **16**, 73 (1990)].
58. V. N. Zharkov, V. M. Lyubimov, and A. I. Osnach, *Izv. Akad. Nauk SSSR, Fiz. Zemli*, No. 10, 3 (1968).
59. V. N. Zharkov, A. B. Makalkin, and V. P. Trubitsyn, *Astron. Zh.* **51**, 1288 (1974).
60. V. N. Zharkov and V. P. Trubitsyn, *Icarus* **21**, 152 (1974).
61. V. N. Zharkov and V. P. Trubitsyn, *Astron. Zh.* **52**, 599 (1975) [*Sov. Astron.* **19**, 366 (1975)].
62. V. N. Zharkov and V. P. Trubitsyn, *Physics of the Planetary Interiors* (Nauka, Moscow, 1980) [in Russian].
63. V. N. Zharkov, V. P. Trubitsyn, I. A. Tsarevskii, and A. B. Makalkin, *Izv. Akad. Nauk SSSR, Fiz. Zemli*, No. 10, 3 (1974).

Translated by V. Astakhov

Orbital Evolution of New Distant Neptunian Satellites and ω -Librators in the Satellite Systems of Saturn and Jupiter

M. A. Vashkov'yak*

*Keldysh Institute of Applied Mathematics, Russian Academy of Sciences,
Miuskaya pl. 4, Moscow, 125047 Russia*

Received April 2, 2003

Abstract—We used data on the recently discovered three outer Neptunian satellites to analyze the long-period evolution of their orbits. We estimated the ranges of eccentricities and inclinations as well as approximate circulation periods of the pericenter arguments and the longitudes of the ascending nodes. The results were mainly obtained by using two different versions of the averaged Hill problem. Plane sections of the phase space of satellite orbital elements are given. We discuss the peculiarity of the evolution of several satellite orbits related to the librational variation of the pericenter argument ω . The ω -librators of Saturn's system were found to qualitatively differ from the libration orbit in the system of Jupiter.
© 2003 MAIK "Nauka/Interperiodica".

Key words: *celestial mechanics; Solar System—minor bodies, orbital evolution; Jovian; Saturnian, and Neptunian satellites; ω -librators.*

INTRODUCTION

The discovery of three new Neptunian satellites was reported in mid-January, 2003 (Marsden 2003a). These satellites were discovered as a result of observations made by J.-M. Petit, P. Rousset, O. Mousis, J. Kavelaars, and M. Holman and the follow-up measurements made by B. Gladman, M. Holman, J. Kavelaars, T. Grav, W. Fraser, and D. Milisavljevic. Green 2003 mentioned, besides the above researchers, the names of P. Nicholson and V. Carruba. The preliminary orbits of the satellites were computed by B.G. Marsden and R. Jacobson. The satellites in question have been named S/2002 N1, N2, and N3. Table 1 gives the new orbital elements of the satellites adopted from the Internet source at <http://www.harvard.edu/mpec/KO3/KO3A75.html>. We used standard Designations for Keplerian elements and the same initial epoch t_0 —2002 Nov. 22.0 TT = JDT 2452600.5—for all three satellites. The angular elements refer to the ecliptic and equinox of 2000.0. As pointed out in the circulars mentioned above, the orbital eccentricities of satellites N2 and N3 are only preliminary (they are marked by asterisks in Table 1).

Descriptions of the peculiar features of the earlier discovered Neptunian satellites can be found in many papers (see, e.g., the review by Vashkov'yak 1991).

The discovery of new satellites has made our knowledge about the Neptunian Satellite more complete. These satellites make up, or rather belong to, a group of distant or external satellites. Their semimajor axes, which are about 20–22 million km, exceed more than twice the apocentric distance of the Neptunian satellite Nereid (which has the most elongated orbit among all known satellites, with an eccentricity of 0.75 and an apocentric distance of about 9.6 million km). The Sun is the principal perturbation source for the outer satellites. Parameter

$$\gamma = -\frac{\mu a_0^2 c_{20} a^3}{\mu' a^5}, \quad (1)$$

which characterises the ratio of perturbing accelerations due to the flattening of the planet and solar attraction, does not exceed 10^{-5} for S/2002 N1, N2, and N3.

Below we report the values of the constant parameters for the Sun–Neptune System adopted in this paper:

$\mu = 6836\,548.25 \text{ km}^3 \text{ s}^{-2}$, the gravitational constant of Neptune;

$a_0 = 25\,225 \text{ km}$, the mean equatorial radius of Neptune;

$c_{20} = -0.003708$, the coefficient of the second equatorial harmonic of the potential of its attraction;

$\alpha_0 = 298^\circ 02$, $\delta_0 = 40^\circ 66$, the right ascension and declination of the Neptunian North Pole, respectively;

*E-mail: vashkov@keldysh.ru

Table 1. Orbital elements of new outer Neptunian satellites

Satellite	S/2002 N1	S/2002 N2	S/2002 N3
M_0 , deg	39.23980	191.17050	269.57627
n , deg/day	0.12551296	0.14308668	0.13106531
a , AU	0.1470004	0.1347032	0.1428189
e	0.4317281	0.1728137*	0.4726309*
ω , deg	179.13011	27.07148	144.58207
Ω , deg	228.89412	60.63766	53.65304
i , deg	120.50347	56.90003	42.50063

Table 2. Characteristics of the evolving orbits of the outer Neptunian satellites (analytical solution)

Satellite	S/2002 N1	S/2002 N2	S/2002 N3
c_1	0.212	0.298	0.427
c_2	0.074	0.007	0.060
e_{\min}	0.43	0.13	0.39
e_{\max}	0.84	0.72	0.65
\tilde{i}_{\min} , deg	121	38	31
\tilde{i}_{\max} , deg	147	57	45
$T_{\tilde{\omega}}$, year	2480	5060	2760
$T_{\tilde{\Omega}}$, year	2670	4400	3270

$\mu' = 132\,712\,442\,007 \text{ km}^3 \text{ s}^{-2}$, the gravitational constant of the Sun;

$a' = 4\,498\,252\,911 \text{ km}$, the semimajor axis of the orbit of Neptune;

$i' = 1^\circ 8'$, the inclination of the orbit of Neptune at time t_0 ;

$\Omega' = 131^\circ 2'$, the longitude of the ascending node of the orbit of Neptune at time t_0 ; and

$\lambda' = 310^\circ 7'$, the mean longitude of Neptune at time t_0 .

METHODS OF ANALYSIS.

CHARACTERISTICS OF EVOLVING ORBITS

Here we use three different methods to analyze the evolution of the orbits of satellites.

The first analytical solution is based on the integrable twice averaged Hill problem (Lidov 1961; Kozai 1962) and its general solution (Vashkov'yak 1999). The first integrals of the evolutionary system

$$a = c_0, \quad (1 - e^2) \cos^2 \tilde{i} = c_1, \quad (2)$$

$$e^2(2/5 - \sin^2 \tilde{i} \sin^2 \tilde{\omega}) = c_2$$

at $\gamma = 0$ were obtained by Lidov (1961). In formulas (2) the angular variables \tilde{i} and $\tilde{\omega}$ (unlike i , ω) refer to the orbital plane of the perturbing body (the Sun) whose position relative to the ecliptic is determined by i' and Ω' . The solution of this problem makes it possible to estimate the variation intervals of the eccentricities and inclinations and also the circulation periods of the arguments of the pericenter and longitudes of the ascending nodes of satellite orbits. Table 2 gives the corresponding e_{\min} , e_{\max} , \tilde{i}_{\min} , \tilde{i}_{\max} , $T_{\tilde{\omega}}$, and $T_{\tilde{\Omega}}$, as well as constants c_1 and c_2 .

Note that the constant c_1 does not exceed $3/5$ for any of the three satellites. This means that in the $(\tilde{\omega}, e)$ plane there are domains where the argument of the pericenter, $\tilde{\omega}$, exhibits libration-type variations $\pm\pi/2$ for $c_2 < 0$ (Lidov 1961). However, for the orbits of the satellites considered, the parameters $\tilde{i}, \tilde{\omega}$ have such values that $c_2 > 0$, and therefore $\tilde{\omega}$ (and also ω) varies monotonically. However, c_2 remains rather small, and this results in strong variation of the eccentricities. Rather appreciable e_{\max} values for all three orbits make them related in a sense to the highly elliptical orbit of Nereid.

The second combined (or numerically-analytical) method takes into account the additional terms of the perturbation function omitted in the twice averaged problem. These are, first and foremost, the periodic terms with the period equal to half the orbital period of Neptune. In addition, we also took into account the secular and long-periodic terms $\sim (a/a')^2 \sin i'$ and $\sim (a/a')^3 e'$ (here e' is the eccentricity of the orbit of Neptune). We allow for the secular perturbations due to Triton—the most massive Neptunian satellite—by formally reducing the coefficient c_{20} by

$$\delta = \frac{\mu_T}{2\mu} \left(\frac{a_T}{a_0} \right)^2, \quad (3)$$

where μ_T is the gravitational constant of Triton and a_T , the semimajor axis of its orbit (we assume that $a_T \ll a$). We have, for the adopted designations, $\mu_T/\mu = 0.00134$ and $a_T/a_0 = 14.33$, and the “effective” coefficient of the second zonal harmonic is computed according to the formula

$$c_{20}^{(\text{eff})} = c_{20} - \delta \quad (4)$$

and is equal to 0.1413.

Below we give the set of evolutionary equations, which includes only the most important periodic terms. This equation set has the form

$$\frac{da}{d\tau} = 0, \quad (5)$$

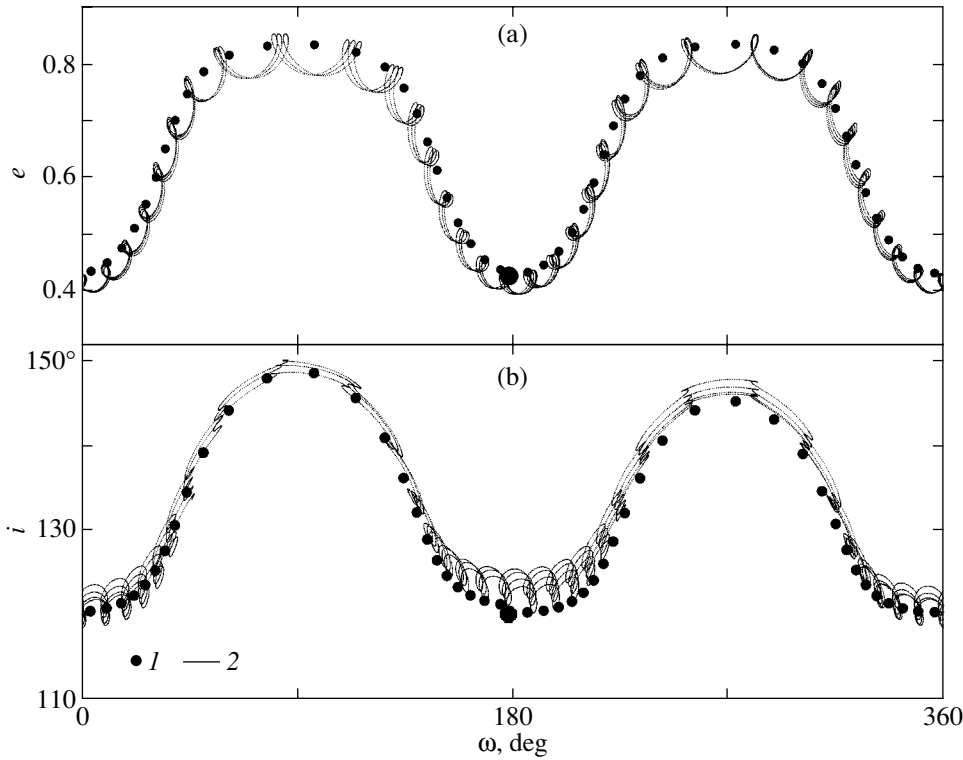


Fig. 1. Characteristics of the orbital evolution of the satellite S/2002 N1: (a) in the (ω, e) plane; (b) in the (ω, i) plane; (1) analytical solution; (2) numerically-analytical solution.

$$\begin{aligned} \frac{de}{d\tau} &= 10e\sqrt{1-e^2} [\sin^2 i \sin 2\omega \\ &+ C(2 - \sin^2 i) \sin 2\omega - 2S \cos i \cos 2\omega], \\ \frac{di}{d\tau} &= -\frac{2 \sin i}{\sqrt{1-e^2}} \{5(1-C)e^2 \cos i \sin 2\omega \\ &+ S[2 + e^2(3 + 5 \cos 2\omega)]\}, \\ \frac{d\omega}{d\tau} &= \frac{2}{\sqrt{1-e^2}} \{[4 + e^2 - 5 \sin^2 i + 5(\sin^2 i - e^2) \\ &\times \cos 2\omega] + C[5(2 - e^2 - \sin^2 i) \cos 2\omega \\ &+ 5 \sin^2 i - 2 - 3e^2] + 5S(2 - e^2) \cos i \sin 2\omega\}, \\ \frac{d\Omega}{d\tau} &= -\frac{2}{\sqrt{1-e^2}} \{(1-C) \\ &\times [2 + e^2(3 - 5 \cos 2\omega)] \cos i + 5Se^2 \sin 2\omega\}, \\ C &= \cos 2(\lambda' - \Omega), \quad S = \sin 2(\lambda' - \Omega), \\ \tau &= \frac{3\mu'a^3}{16\mu a^3} n(t - t_0), \quad \lambda' = \lambda'_0 + n'(t - t_0), \end{aligned}$$

where n and n' are the mean motions of the satellite and Neptune, respectively. The set of evolutionary equations (5) has only two first integrals (Moiseev 1945):

$$a = \bar{c}_0, \quad \frac{3\mu'a^2}{16a^3} W(e, i, \omega, \Omega, t) \quad (6)$$

$$+ n' \sqrt{\mu a(1 - e^2)} \cos i = \bar{c}_1,$$

where

$$\begin{aligned} W &= 2(e^2 - \sin^2 i) + e^2 \sin^2 i(5 \cos 2\omega - 3) \quad (7) \\ &+ 10Se^2 \cos i \sin 2\omega + [2 \sin^2 i + 10e^2 \cos 2\omega \\ &+ e^2 \sin^2 i(3 - 5 \cos 2\omega)]C, \end{aligned}$$

and appears to be unintegrable. We therefore solve it numerically.

The third and the most accurate method consists of the numerical integration of rigorous (unaveraged) equations of the satellite's motion in Cartesian coordinates with the allowance for the perturbing effect of the flattening of Neptune, and the attraction of the Sun and giant planets. The effect due to Triton can be allowed for approximately in the same way as in the second method.

To compare the results obtained using the methods described above, we show here the cross sections of the phase space of the orbital elements by planes (ω, e) and (ω, i) . In Figs. 1–3 for satellites N1, N2, N3, the large dots indicate the orbital-element values obtained using the first (analytical) method on time intervals $\sim T_{\omega}$. In this case, the motion along the phase-space trajectories of the integrable problem is in the direction of increasing ω . The thin lines show the results obtained using the

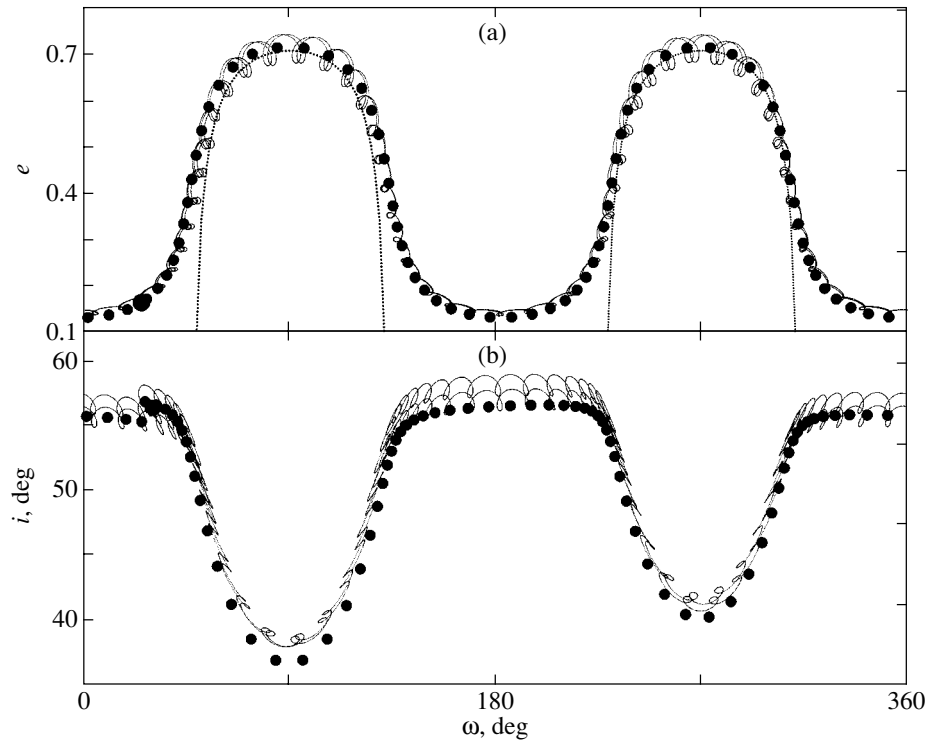


Fig. 2. Same as Fig. 1 but for S/2002 N2.

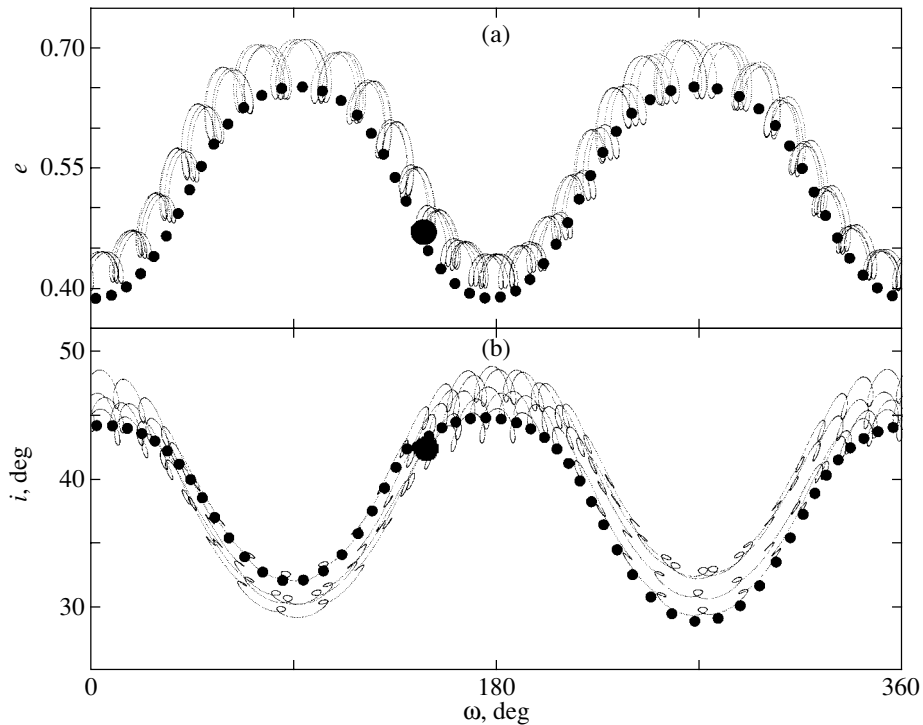


Fig. 3. Same as Fig. 1, but for S/2002 N3.

second (numerically-analytical) method over an approximately 10-thousand year long time interval. The larger filled circles in all figures indicate the corresponding initial positions.

The relations given here make it possible to estimate the real variation intervals for eccentricities and inclinations and how much they differ from the extreme values given by the analytical solution of the

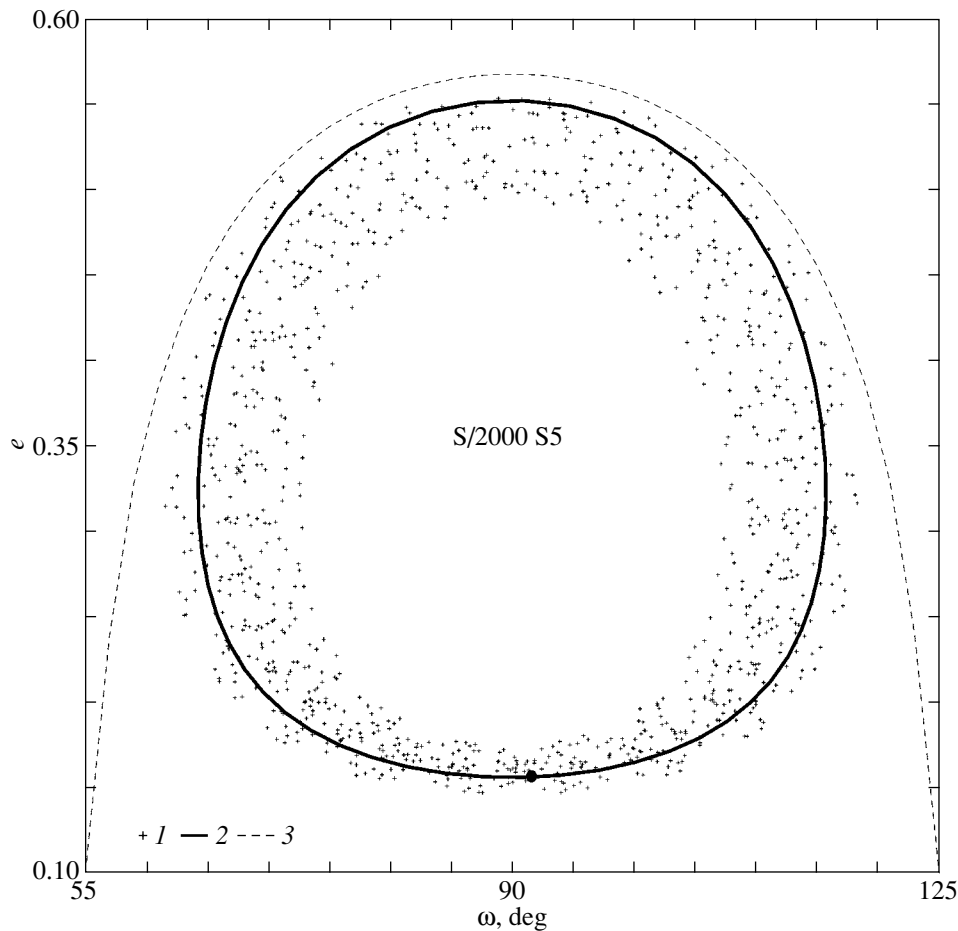


Fig. 4. The phase plane (ω , e) of the S/2000 S5 satellite: (1) the numerically analytical solution; (2) the analytical solution, and (3) the separatrix.

evolutionary problem. The extreme values of inclinations i differ from \tilde{i} , given in Table 2, by about 5° (Figs. 1b, 2b, 3b), and the eccentricities by 0.05 (Figs. 1a, 2a, and 3a). Somewhat greater discrepancies were found for isochronic differences of the time dependences of the orbital elements obtained using the first two methods for a ~ 1000 -year time intervals. Note that the difference between the extreme eccentricity values is maximum for the satellite N2 and amounts to about 0.6. The corresponding $c_2 = 0.007$ is the lowest among the three values given in Table 2 and the phase trajectory of the integrable problem in the (ω, e) plane is the closest to the separatrix that separates the domains of libration and circulation of ω . In Fig. 2a, this limiting value is shown by dashed lines only for N2. Note that the initial orbital eccentricities of the satellites N2 and N3 are only preliminary. We also point out the difference between the initial and final points of the analytical solution in the (ω, i) plane. No such difference can be seen in the $(\tilde{\omega}, \tilde{i})$ plane.

The third (numerical) method allowed us to es-

tablish that the variation interval of short-periodic oscillations of the major axes of the orbits of the three satellites are about 220, 150, and 240 thousand km for the satellites N1, N2, and N3, respectively.

Thus, the main qualitative characteristics of the orbital evolution of the satellites S/2002 N1, N2, and N3 can be satisfactorily described by the solution of the twice averaged Hill problem. More accurate qualitative characteristics can be obtained by numerically solving the evolutionary equations averaged over the motion of the satellite and with approximate allowance for periodic solar perturbations (with periods equal to half the orbital period of Neptune). Short-periodic perturbations are apparently required only for constructing full analytical theories of the motion of the above-mentioned satellites.

LIBRATION ORBITS OF SATELLITES

One of the interesting results of the qualitative analysis of the twice averaged Hill problem is that we found satellite orbits with libration-type variation

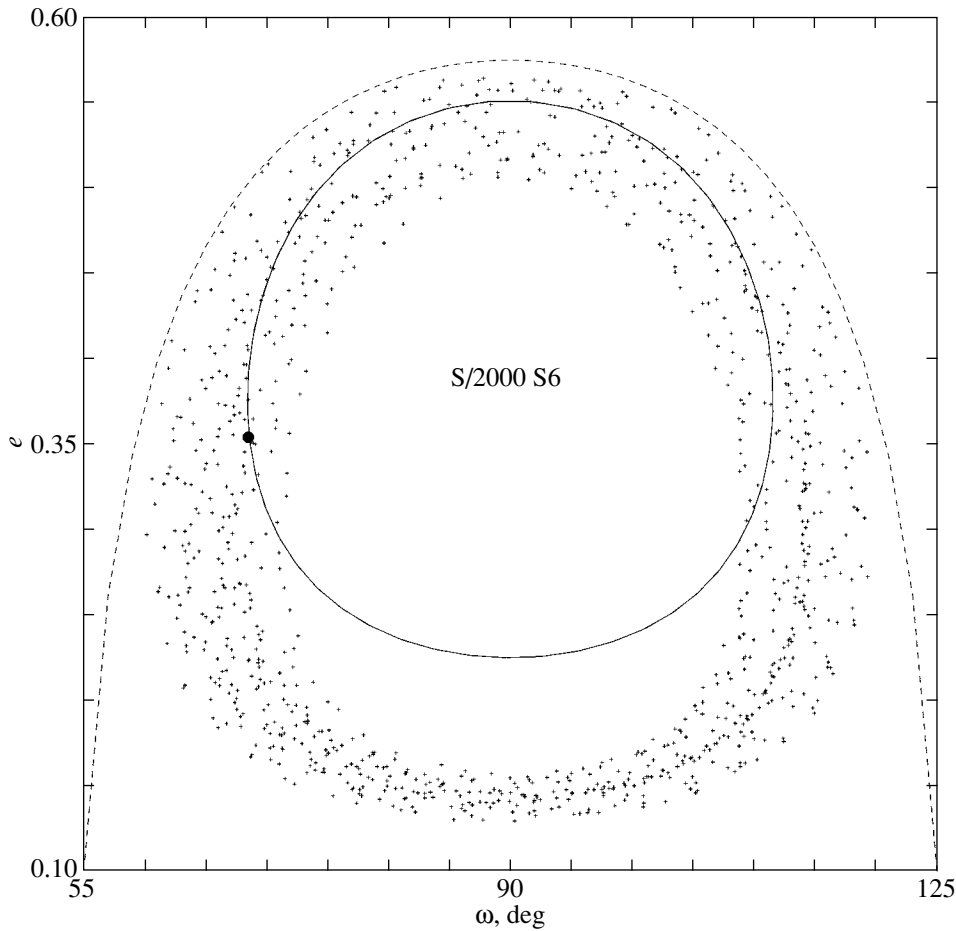


Fig. 5. Same as Fig. 4, but for S/2000 S6.

of the pericenter argument to exist at $c_1 < 3/5$. As mentioned above, the possibility of the existence of such orbits was first discovered by Lidov (1961). In the phase plane $(\tilde{\omega}, e)$, the trajectories with libration-type variation of $\tilde{\omega}$ embrace a stationary singular point with coordinates

$$\tilde{\omega} = \pm\pi/2, \quad e = \sqrt{1 - \sqrt{\frac{5c_1}{3}}}.$$

Kozai (1962) analyzed a more general problem with the additional terms $\sim(a/a')^{k \leq 8}$ by including W in the twice averaged perturbation function. In the case $a/a' \rightarrow 0$, he integrated the evolutionary problem in elliptical functions and repeated in the Delone elements the qualitative analysis of the evolution earlier performed by Lidov. Note that the work of Kozai is more illustrative: Kozai constructed families of integral curves $W(2\tilde{\omega}, \sqrt{1-e^2}) = \text{const}$ with different fixed a, c_1 , which particularly correspond to the orbit of asteroid (1373) Cincinnati. This orbit became the first real ω -librator to be discovered by Kozai.

For a stationary singular point surrounded by li-

bration trajectories in the $(\tilde{\omega}, e)$ plane, the following conditions

$$\dot{e} = 0, \quad \dot{\tilde{\omega}} = 0 \quad (8)$$

are satisfied. The second of these conditions means that the angular rate of the variation of the longitude of the ascending node $\dot{\Omega}$ is equal to that of the longitude of the pericenter, $g = \dot{\Omega} + \tilde{\omega} \text{sgn}(\cos i)$, i.e.,

$$\dot{\tilde{\Omega}} = \dot{g}. \quad (9)$$

This circumstance gives us grounds for calling the singular point a resonance point, and the libration-type variation of $\tilde{\omega}$ in its vicinity the Kozai resonance. Since all qualitative features revealed by Lidov are preserved in the case studied by Kozai, it would be proper, as suggested by Neistadt (Arnold *et al.* 2002, p. 219), to call it the Lidov–Kozai resonance. For the same reasons, the effect of the abrupt increase of eccentricity $c_1 \rightarrow 0$, $\tilde{\omega} \rightarrow \pi/2$, and, consequently, the inevitable collision between the satellite and a finite-sized central attractive body could justifiably be called the Lidov–Kozai mechanism.

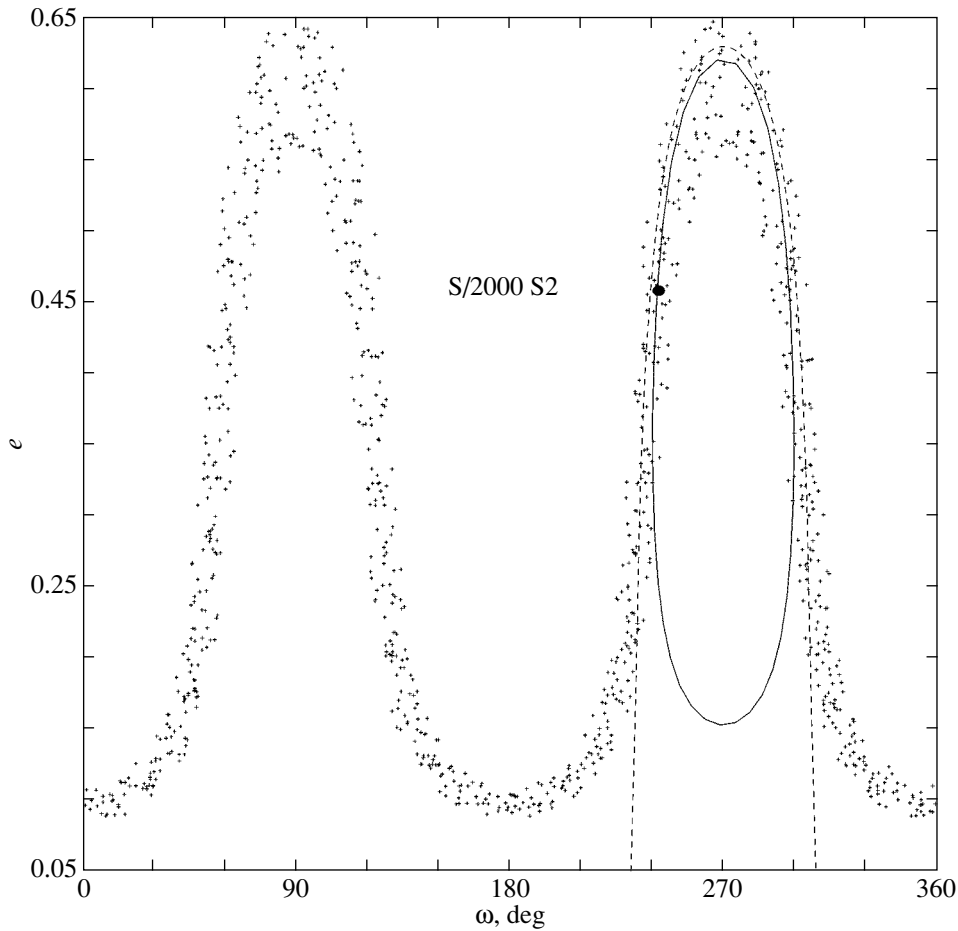


Fig. 6. Same as Fig. 4, but for S/2000 S2.

The overwhelming majority of the orbits of the natural satellites of the planets, including those of the recently discovered satellites of giant planets, exhibit circulation-type variations of the argument of the pericenter. However, the orbits of three satellites show libration-type variations of ω ; these are the Saturnian S/2000, S5, and S6, and the Jovian satellite S/2001 J10.

In the Saturnian system, ω -librators have been found both analytically (Vashkov'yak 2001) and by numerically integrating the rigorous equations of motion (Carruba *et al.* 2002). Figures 4 and 5 show the results of our computations in the (ω, e) plane made using the first two methods described in the previous section. We integrated equations of motion over a 10-thousand year long time interval and adopted the initial elements from the reports of Marsden (2001a, 2001b). Solid lines show the analytical solution of the twice averaged Hill problem in variables $(\tilde{\omega}, e)$, while dashed elements show the separatrices. Filled circles indicate the initial positions in the phase plane. Note that all crosses fall within the domains bounded by separatrices and therefore the librational nature

of the pericenter argument's changes in the doubly-averaged problem (the Lidov–Kozai resonance) is preserved, and in a more complete model of evolution. In this case, the phase points in the (ω, e) plane fill a ring-like domain near the trajectories of the integrable problem, and the periodic perturbations have comparatively little effect.

As is evident from Fig. 5, in the case of the satellite S/2000 S6, the analytical solution yields an eccentricity e_{\min} that differs appreciably from its real value. Moreover, note that analyzing this problem only in terms of the twice averaged problem at c_2 close to zero may even yield qualitatively incorrect results. It was on the basis of such an analysis that we classified the orbits of two Saturnian satellites—S/2000 S2 and S3—as ω -librators (or, as belonging to the IL group). However, the circulation nature of these orbits already becomes apparent when allowing for periodic solar perturbations with the period equal to half the orbital period of Saturn and even more so in the case of the numerical integration of rigorous equations of the motion of satellites. By way of illustration, Figure 6 shows the results of our computations of the

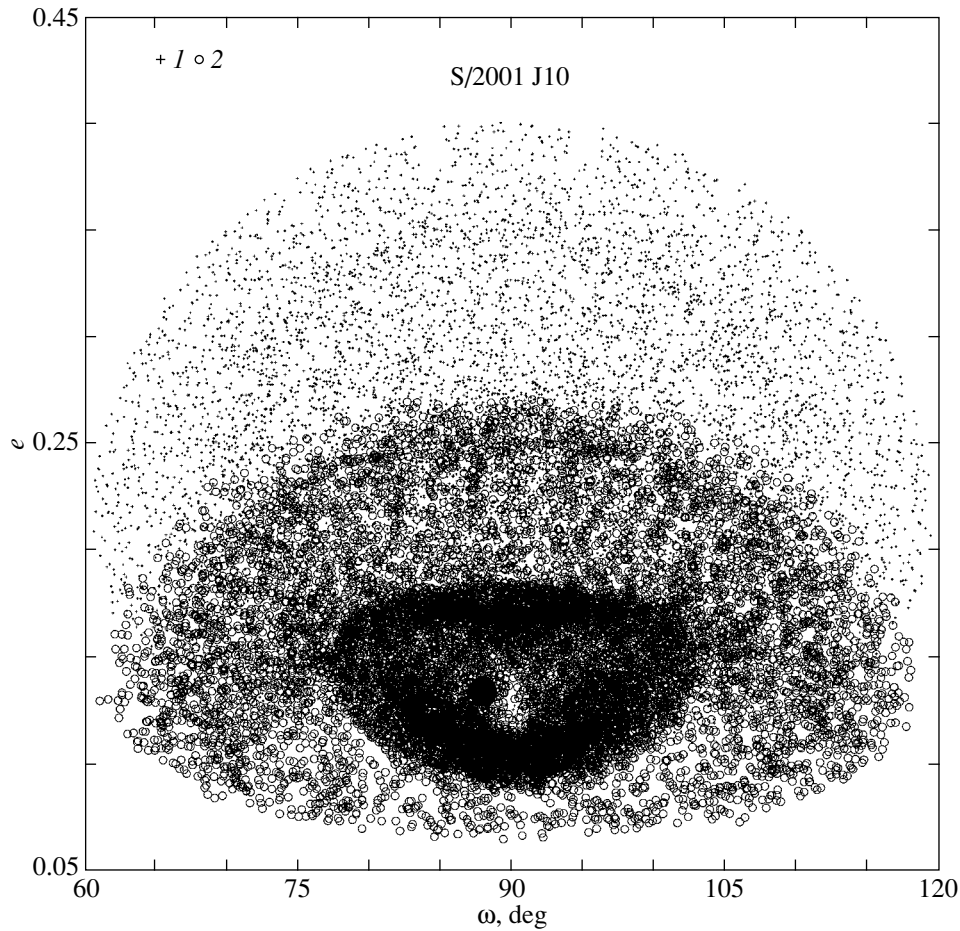


Fig. 7. The phase plane (ω , e) for the satellite S/2001 J10: (1) the numerically-analytical solution; (2) the numerical solution.

orbital evolution of the satellite S/2000 S2. As is evident from the figure, in the case of satellite S2 (in contrast to those of S5 and S6) first of all, the crosses are located on both sides of the separatrix, and, second, the initial phase-space point is located much closer to the latter. Therefore, even periodic perturbations due to the Sun—to say nothing about the short-periodic perturbations—transfer the orbit of the satellite S/2000 S2 into the group of circulation-type orbits (or IC) (the same is true for the orbit of the satellite S/2000 S3). The orbits of these satellites are thus good examples of the qualitative difference between the results obtained in terms of the twice averaged and rigorous problem in the cases where the phase-space trajectory is located very close to the separatrix. In other words, in this case, the closeness to the limiting solution also serves as a limit of applicability of the twice averaged model of the evolution.

In the Jovian system, the orbits of almost all satellites, including those discovered in 2003, show circulation-type variations of the arguments of their pericenters. The only exception is the orbit of the

satellite S/2001 J10. The libration-type nature of ω was discovered by Cuk *et al.* (2002), apparently using a numerical method, and the authors of this paper associate the libration of ω with the Kozai resonance and the Yarkovskii effect. At the same time, it can be established, based on the orbital elements of S/2001 J10 reported by Marsden (2003b), that for this satellite, the constant c_2 is positive and constant c_1 exceeds $3/5$, so that the real difference $c_1 - 3/5$ is equal to several hundredths. This means that in terms of the twice averaged Hill problem, the phase plane ($\tilde{\omega}$, e) has neither singularities nor libration points $\tilde{\omega}$, and the argument of the pericenter increases monotonically just as the longitude of the ascending node does. It also turns out that the circulation periods $\tilde{\omega}$ and $\tilde{\Omega}$ are almost equal to each other (both are close to the 1 : 1 resonance). The numerical values of these periods are approximately 147.9 and 147.1 yr, respectively, so that $\dot{g} \approx 0$.

Unlike the Saturnian satellites S/2000 S5 and S6 considered above, the real variation of the parameter ω of the orbit of S/2001 J10 is due primarily to the effect

of periodic solar perturbations (and perturbations of $\sim e'$, $\sin i'$). The crosses in Fig. 7 show the results of computations made using the numerically-analytical method over a 10-thousand year long time interval, while the circles show the results of the numerical integration of rigorous equations of motion. Although the extreme eccentricity values obtained with the two methods differ markedly from one another, even an approximate allowance for long-periodic solar perturbations yields a qualitatively correct result and the variation intervals of ω differ only slightly. For the orbit of a given satellite, the periodic terms in the right-hand sides of evolutionary equations (5) exceed appreciably the corresponding terms in the twice-averaged Hill problem. Therefore, the complete evolutionary system proves to be quite far from being integrable and the points on the (ω, e) fill the libration domain rather densely. This is the fundamental difference between the libration of the ω parameter of the orbit of the satellite S/2001 J10 and the Lidov–Kozai resonance. A total of 20 new Jovian satellites were discovered at the beginning of March 2003. All three methods described in this paper reveal the libration of the argument of the pericenter of the orbit of the satellite S/2003 J20 relative to 90 degrees as a consequence of the Lidov–Kozai resonance ($c_1 = 0.3$, $c_2 = -0.02$).

REFERENCES

1. V. I. Arnol'd, V. V. Kozlov, and A. I. Neshtadt, *Mathematical Aspects of Classical and Celestial Mechanics* (URSS, Moscow, 2002) [in Russian].
2. V. Carruba, J. A. Burns, P. D. Nicolson, *et al.*, Amer. Astron. Soc., DPS meeting #34, #35.01 (2002).
3. M. Cuk, J. A. Burns, V. Carruba, *et al.*, Amer. Astron. Soc., DPS meeting #34, #23.08 (2002).
4. W. E. Green, IAU Circ. No. 8047 (2003).
5. Y. Kozai, Astron. J. **67**, 591 (1962).
6. M. L. Lidov, Issk. Sputniki Zemli **8**, 5 (1961).
7. B. G. Marsden, MPE Circ. **T07** (2001a).
8. B. G. Marsden, MPE Circ. **T06** (2001b).
9. B. G. Marsden, MPE Circ. **A75** (2003a).
10. B. G. Marsden, MPE Circ. **C53** (2003b).
11. N. D. Moiseev, Tr. Gos. Astron. Shternberg Inst. **XV**, 100 (1945).
12. S. N. Vashkov'yak, Itogi Nauki Tekhn., Ser. Issled. Kosm. Prostranstva **35**, 162 (1991).
13. M. A. Vashkov'yak, Pis'ma Astron. Zh. **25**, 554 (1999) [Astron. Lett. **25**, 476 (1999)].
14. M. A. Vashkov'yak, Pis'ma Astron. Zh. **27**, 533 (2001) [Astron. Lett. **27**, 455 (2001)].

Translated by A. Dambis

Periodic Solutions Near a Central Libration Point in the Problem of the Motion of a Star inside an Elliptical Galaxy

S. A. Gasanov*

Sternberg Astronomical Institute, Universitetskii pr. 13, Moscow, 119992 Russia

Received April 10, 2003

Abstract—We consider the three-dimensional problem of the motion of a star inside an inhomogeneous rotating elliptical galaxy with a homothetic density distribution. We construct and analyze the periodic solutions near a central libration point by using Lyapunov's method. © 2003 MAIK "Nauka/Interperiodica".

Key words: *celestial mechanics*.

INTRODUCTION

Abalakin (1959) studied the problem of the three-dimensional motion of a material point inside an inhomogeneous ellipsoidal body with a homothetic density distribution in a fixed coordinate system. Abalakin found periodic solutions and performed a qualitative analysis. In an earlier paper (Gasanov 2001), we analyzed the flat problem of the motion of a material point inside an inhomogeneous rotating ellipsoidal body with a homothetic density distribution. We derived an expansion of the force function of the problem up to the fourth-order terms of the second eccentricities of the ellipsoid, which are considered to be small parameters. We derived a formula for the perturbing function and solved the equations of the perturbed motion in canonical elements.

Within the framework of the spatial problem, Gasanov and Luk'yanov (2002) found stationary solutions or libration points L_k ($k = 1, 2, \dots, 7$), one of which (L_1) is located at the coordinate origin and is adopted as the central point. We showed that the libration point located at the galactic center is stable in Lyapunov's sense. We constructed zero-velocity surfaces and the domains of possible motion inside and outside the galaxy, and showed that the motions inside the galaxy are stable in Hill's sense, i.e., each star moves inside a closed region. We showed that a Roche model can be constructed for galaxies shaped as three-axial ellipsoids or as oblate ellipsoids of revolution.

In this paper, we construct periodic solutions near the central libration point $L_1 = L_1(0, 0, 0)$ using the Lyapunov method within the framework of the problem of the motion of a star inside an inhomogeneous

rotating elliptical galaxy with a homothetic density distribution.

Let T be an elliptical galaxy that is bounded by the elliptical surface

$$\frac{x^2}{A^2} + \frac{y^2}{B^2} + \frac{z^2}{C^2} = 1, \quad A \geq B \geq C, \quad (1)$$

and has a homothetic (ellipsoidal) density distribution. Density ρ in this galaxy is a function of a certain parameter $p = p(x, y, z)$ and varies continuously from the center to the outer surface. On this basis, we set the density distribution T in the body in the form of a converging power series in parameter p (Gasanov 2001):

$$\rho = \rho(p) = \rho_0 + \sum_{n=1}^{\infty} \rho_n \varepsilon^n p^n, \quad (2)$$
$$0 < \varepsilon < 1, \quad 0 \leq p \leq 1,$$

where ε is a small parameter that characterizes the density distribution. The following additional conditions

$$\rho(0) = \rho_0 > 0, \quad \rho(1) = \rho_f, \quad (3)$$
$$\rho_n < 0, \quad n = 1, 2, \dots$$

are satisfied. Here ρ_0 and ρ_f are the density values at the center and the surface of the ellipsoidal body, respectively. In expansion (2) for the density ρ , we leave only the terms up to ε order inclusive, i.e., only the terms with the coefficients ρ_0 and ρ_1 .

FORMULATION OF THE PROBLEM

Let us consider now the problem of the motion of a P inside an elliptical galaxy rotating at a constant and relatively small angular speed Ω about the OZ axis exclusively under the action of the attraction force of

*E-mail: gasnizh@sai.msu.ru

the latter. The coordinates x, y, z refer to a Cartesian coordinate system with the origin O at the center of the galaxy and axes $OX, OY, \text{ and } OZ$ directed along the corresponding principal axes of the ellipsoid (1). In view of the definition of the second eccentricities λ and μ of ellipsoid (1), we have

$$A^2 = C^2(1 + \lambda^2), \quad B^2 = C^2(1 + \mu^2), \quad (4)$$

$$\mu^2 \leq \lambda^2 < 1.$$

We derived the following formula for the total potential V retaining the terms up to the order ε inclusive:

$$V = V_0 + R, \quad V_0 = -\frac{1}{2}(V_{01}x^2 + V_{02}y^2 + V_{03}z^2), \quad (5)$$

$$R = \frac{\varepsilon}{4}(R_1x^4 + R_2y^4 + R_3z^4 + 2R_4x^2y^2 + 2R_5x^2z^2 + 2R_6y^2z^2),$$

where V_0 is the potential of attraction for nonperturbed motion and R the perturbing function. Moreover, the coefficients $V_{0i} > 0$ and $R_k > 0$ ($i = 1, 2, 3; k = 1, 2, \dots, 6$) given in the Appendix are polynomial functions of the second eccentricities λ and μ , and are commensurable with Ω^2 and Ω^2/C^2 , respectively. Here C is the polar axis of ellipsoid (1).

In the coordinate system xyz rotating at a constant and relatively small angular velocity Ω about the z axis, the equations of the motion of a star inside an inhomogeneous gravitating elliptical galaxy have the following form:

$$\frac{d^2x}{dt^2} - 2\Omega \frac{dy}{dt} = \frac{\partial U}{\partial x}, \quad (6)$$

$$\frac{d^2y}{dt^2} + 2\Omega \frac{dx}{dt} = \frac{\partial U}{\partial y},$$

$$\frac{d^2z}{dt^2} = \frac{\partial U}{\partial z}.$$

Hereafter, we use the system of equations (6), where we set

$$U = V_0 + R + \frac{\Omega^2}{2}(x^2 + y^2) \quad (7)$$

to construct periodic solutions near the libration point L_1 using the Lyapunov method.

We found the constraint imposed by the Poincare inequality (a theorem about the existence of a rotating body as an equilibrium figure (Poincare 1911; Ogorodnikov 1958)) on the angular velocity Ω of rotation of the coordinate system in the case of nonperturbed motion ($\varepsilon = 0$) in the following form (Gasanov 2001; Gasanov and Luk'yanov 2002)

$$\Omega^2 < g^2, \quad g^2 < V_{01} \leq V_{02}, \quad (8)$$

and the last double inequality is true in view of relation (4). In the case of nonperturbed motion inequality (8) has the form:

$$\Omega^2 < g^2 - \varepsilon \bar{g}^2. \quad (9)$$

The quantities g^2 and \bar{g}^2 commensurable with Ω^2 can be found in our previous papers (Gasanov (2001) and Gasanov and Luk'yanov (2002)). It follows from this that angular velocity Ω satisfies inequalities (8) and (9).

We showed (Gasanov 2001; Gasanov and Luk'yanov 2002) that in the case of nonperturbed motion at $R = 0$ or with $\varepsilon = 0$, the characteristic equation of system (6)

$$(\Lambda^4 + p\Lambda^2 + q)(\Lambda^2 + g_3^2) = 0 \quad (10)$$

$$(p = 4\Omega^2 + g_1^2 + g_2^2, \quad q = g_1^2g_2^2),$$

has three pairs of purely imaginary roots $\Lambda_k = \pm i\theta_k$, $k = 1, 2, 3$. Quantities g_1^2, g_2^2 , and g_3^2 in equation (10) are determined by the following equalities

$$g_1^2 = V_{01} - \Omega^2, \quad g_2^2 = V_{02} - \Omega^2, \quad g_3^2 = V_{03} \quad (11)$$

in view of condition (8). The same condition implies that

$$g_1^2 \leq g_2^2. \quad (12)$$

In this case there are no resonances between θ_1 and θ_2

$$\theta_1 = \sqrt{\frac{p}{2} - D}, \quad \theta_2 = \sqrt{\frac{p}{2} + D}, \quad D = \sqrt{\frac{p^2}{4} - q}, \quad (13)$$

which are commensurable with Ω . The two remaining roots can be found from the following equation

$$\Lambda^2 + g_3^2 = 0, \quad (\theta_3 = g_3). \quad (14)$$

It is obvious that $p \geq 0, q \geq 0$ and it can be easily proved that $p^2 - 4q \geq 0$ (Gasanov and Luk'yanov 2002).

Let $\Lambda = \pm i\theta$ be a pair of such roots of characteristic equation (10). Following the Lyapunov method, we set

$$T = \frac{2\pi}{\theta} \left(1 + h_2c^2 + h_3c^3 + h_4c^4 + h_5c^5 + \dots \right) \quad (15)$$

and introduce instead of t the new independent variable τ via the following substitution

$$\tau = \frac{2\pi}{T}(t - t_0). \quad (16)$$

The system of equations (6) with the terms up to the order of ε inclusive in the expansion of the perturbing function R can then be written in the following form:

$$\frac{d^2x}{d\tau^2} - 2\Omega \left(\frac{T}{2\pi} \right) \frac{dy}{d\tau} = \left(\frac{T}{2\pi} \right)^2 \quad (17)$$

$$\begin{aligned} & \times \left[-g_1^2 + \varepsilon(R_1x^2 + R_4y^2 + R_5z^2) \right] x, \\ & \frac{d^2y}{d\tau^2} + 2\Omega \left(\frac{T}{2\pi} \right) \frac{dx}{d\tau} = \left(\frac{T}{2\pi} \right)^2 \\ & \times \left[-g_2^2 + \varepsilon(R_4x^2 + R_2y^2 + R_6z^2) \right] y, \\ & \frac{d^2z}{d\tau^2} = \left(\frac{T}{2\pi} \right)^2 \left[-g_3^2 + \varepsilon(R_5x^2 + R_6y^2 + R_3z^2) \right] z. \end{aligned}$$

We now try to satisfy equations (17) by segments of power series in arbitrary constant c up to the fifth order inclusive (Lyapunov 1956; Duboshin 1964):

$$\begin{aligned} x &= x_1c + x_2c^2 + x_3c^3 + x_4c^4 + x_5c^5, \quad (18) \\ y &= y_1c + y_2c^2 + y_3c^3 + y_4c^4 + y_5c^5, \\ z &= z_1c + z_2c^2 + z_3c^3 + z_4c^4 + z_5c^5. \end{aligned}$$

To determine the coefficients x_k, y_k, z_k in equation (18), which must be periodic functions of variable τ (sines and cosines of multiples of τ), we substitute them into Eqs. (17). Here we take into account the fact that for each θ , there is a unique periodic solution, which at the same time uniquely determines all constants h_k (Lyapunov 1956; Duboshin 1964).

PERIODIC SOLUTION FOR COEFFICIENTS

$x_n, y_n,$ AND z_n

We obtain, after substituting equalities (18) into the system of equations (17) for the coefficients $x_n, y_n,$ and z_n ($n = 1, 2$), which correspond to $\varepsilon = 0$, the following system of homogeneous linear equations:

$$\begin{aligned} \frac{d^2x_n}{d\tau^2} - \frac{2\Omega}{\theta} \frac{dy_n}{d\tau} &= -\frac{g_1^2}{\theta^2} x_n, \quad (19) \\ \frac{d^2y_n}{d\tau^2} + \frac{2\Omega}{\theta} \frac{dx_n}{d\tau} &= -\frac{g_2^2}{\theta^2} y_n, \\ \frac{d^2z_n}{d\tau^2} &= -\frac{g_3^2}{\theta^2} z_n. \end{aligned}$$

The solutions to the system of equations (19) at $\theta = \theta_k$, ($k = 1, 2$) can be written in the following form (Matveev 1967):

$$\begin{aligned} x_1 &= x_2 = c_{11} \cos \tau + d_{11} \sin \tau, \quad (20) \\ y_1 &= y_2 = \frac{1}{\sigma_0} \left(d_{11} \cos \tau - c_{11} \sin \tau \right), \\ z_1 &= z_2 = 0, \end{aligned}$$

where c_{11} and d_{11} are arbitrary constants that have the dimensions of length and σ_0 is a dimensionless quantity determined by the following equation:

$$\sigma_0 = \frac{\pm 2\Omega\theta_k}{\theta_k^2 - g_1^2} = \frac{\theta_k^2 - g_2^2}{\pm 2\Omega\theta_k}. \quad (21)$$

We find the solutions to the system of equations (19) at $\theta = \theta_3$ in the following form:

$$\begin{aligned} x_1 &= x_2 = 0, \quad y_1 = y_2 = 0, \quad (22) \\ z_1 &= z_2 = g_{11} \cos \tau + h_{11} \sin \tau, \end{aligned}$$

where g_{11} and h_{11} are arbitrary constants that have the dimensions of length.

Thus, the periodic solutions to the system of equations (19) at $\theta = \theta_k$ and $k = 1, 2$ without mutual resonances can be written in the form given by formula (20) and at $\theta = \theta_3$, in the form of formula (22).

By analogy with Eq. (19), the coefficients $x_k, y_k,$ and z_k , $k = 3, 4, 5$ can be found from the equation sets given in the Appendix. We write the solutions to these equation sets in the following form:

$$\begin{aligned} x_k &= \sum_{s=0}^k [c_{ks} \cos s\tau + d_{ks} \sin s\tau], \quad (23) \\ y_k &= \sum_{s=0}^k [e_{ks} \cos s\tau + f_{ks} \sin s\tau], \\ z_k &= \sum_{s=0}^k [g_{ks} \cos s\tau + h_{ks} \sin s\tau], \quad k = 3, 4, 5. \end{aligned}$$

Similarly, we substitute solutions (20) and (23) into the system of equations for $x_3, y_3,$ and z_3 at $\theta = \theta_k$ and $k = 1, 2$ to obtain

$$x_3 = c_{31} \cos \tau + d_{31} \sin \tau + \varepsilon c_{33} (\cos 3\tau + \sigma_1 \sin 3\tau), \quad (24)$$

$$\begin{aligned} y_3 &= \frac{1}{\sigma_0} (d_{31} \cos \tau - c_{31} \sin \tau) \\ &+ \varepsilon f_{33} (\sin 3\tau - \sigma_1 \cos 3\tau), \quad z_3 = 0, \end{aligned}$$

where c_{31} and d_{31} are arbitrary constants that have the dimensions of length. Coefficients c_{33} and f_{33} , which also have the dimensions of length, and dimensionless quantity σ_1 are given in the Appendix. Dimensionless quantity h_2 is equal to

$$h_2 = \frac{d_{11}^2 + c_{11}^2}{8\sigma_0^2\theta_k} \frac{\varepsilon}{\xi_0^2 + \eta_0^2} \quad (25)$$

$$\times \left[3\sigma_0^3\xi_0 R_1 + 3\eta_0 R_2 + \sigma_0(\xi_0 + \sigma_0\eta_0) R_4 \right],$$

where the quantities ξ_0 and η_0 that are commensurable with Ω are given in the Appendix.

We now construct the periodic solution to the system of equations for $x_3, y_3,$ and z_3 that corresponds to $\theta = \theta_3$. This solution has the following form:

$$\begin{aligned} x_3 &= 0, \quad y_3 = 0, \quad (26) \\ z_3 &= g_{31} \cos \tau + h_{31} \sin \tau + \varepsilon h_{33} (\sin 3\tau + \sigma_2 \cos 3\tau), \end{aligned}$$

where coefficients g_{31} and h_{31} are arbitrary constants having the dimensions of length. Coefficient h_{33} , which also has the dimensions of length, and dimensionless quantity σ_2 are given in the Appendix. In this case the dimensionless quantity is equal to

$$h_2 = \frac{3\epsilon R_3}{8\theta_3^2} (g_{11}^2 + h_{11}^2). \quad (27)$$

We now pass on to solving the system of equations for x_4, y_4 , and z_4 at $\theta = \theta_k$ and $k = 1, 2$. We obtain for this system of equations

$$x_4 = c_{41} \cos \tau + d_{41} \sin \tau + 3\epsilon c_{33} (\cos 3\tau + \sigma_1 \sin 3\tau), \quad (28)$$

$$y_4 = \frac{1}{\sigma_0} (d_{41} \cos \tau - c_{41} \sin \tau) + 3\epsilon f_{33} (\sin 3\tau - \sigma_1 \cos 3\tau),$$

$$z_4 = 0,$$

and

$$h_3 = 2h_2, \quad (29)$$

where c_{41} and d_{41} are arbitrary constants having the dimensions of length.

We now find the solution to the equations for x_4, y_4 , and z_4 that corresponds to the root $\theta = \theta_3$. We similarly obtain

$$x_4 = 0, \quad y_4 = 0, \quad (30)$$

$$z_4 = g_{41} \cos \tau + h_{41} \sin \tau + 3\epsilon h_{33} (\sin 3\tau + \sigma_2 \cos 3\tau),$$

where g_{41} and h_{41} are arbitrary constants having the dimensions of length. Here we also find that h_3 can be expressed by formula (29) and h_2 is then determined from equation (27).

We first consider the system of equations for x_5, y_5 , and z_5 at $\theta = \theta_3$. Taking into account solutions (22), (23), and (26) in this system of equations, we obtain, by analogy with the previous cases:

$$x_5 = 0, \quad y_5 = 0, \quad z_5 = g_{51} \cos \tau + h_{51} \sin \tau + \epsilon h_{53} (\sin 3\tau + \sigma_2 \cos 3\tau) + \epsilon^2 h_{55} (\sigma_4 \cos 5\tau + \sin 5\tau), \quad (31)$$

where g_{51} and h_{51} are arbitrary constants having the dimensions of length. Coefficients h_{53} and h_{55} , which also have the dimensions of length, and dimensionless quantity σ_4 are given in the Appendix. The dimensionless quantity h_4 is equal to:

$$h_4 = \left(1 + 2\frac{h_{31}}{h_{11}}\right) h_2 + O(\epsilon^2), \quad (32)$$

provided that h_2 is determined by equation (27) and

$$h_{31}g_{11} = g_{31}h_{11}. \quad (33)$$

We now pass on to the case $\theta = \theta_k$ and $k = 1, 2$. Taking into account in the system of equations x_5, y_5 , and z_5 solutions (20), (23), and (24), we obtain:

$$x_5 = c_{51} \cos \tau + d_{51} \sin \tau + \epsilon c_{53} (\cos 3\tau + \sigma_1 \sin 3\tau) + \epsilon^2 c_{55} (\cos 5\tau + \sigma_3 \sin 5\tau), \quad (34)$$

$$y_5 = \frac{1}{\sigma_0} (d_{51} \cos \tau - c_{51} \sin \tau) + \epsilon f_{53} (\sin 3\tau - \sigma_1 \cos 3\tau) + \epsilon^2 f_{55} (\sin 5\tau - \sigma_3 \cos 5\tau), \quad z_5 = 0,$$

where c_{51} and d_{51} are arbitrary constants having the dimensions of length. The coefficients $c_{5k}, f_{5k}, k = 3, 5$, which also have the dimensions of length, and the dimensionless quantity σ_3 are given in the Appendix.

We find the following formula for the dimensionless quantity h_4 :

$$h_4 = \left(1 + 2\frac{c_{31}}{c_{11}}\right) h_2 + O(\epsilon^2), \quad n = 1, 2, 4, \quad (35)$$

provided that h_2 is determined by equation (25) and

$$c_{31}d_{11} = d_{31}c_{11}. \quad (36)$$

FAMILIES OF PERIODIC SOLUTIONS

The families of periodic solution (18) for $\theta = \theta_k, k = 1, 2$ and $\theta = \theta_3$ can be rewritten in the following form:

$$x = a_1 \cos \tau + a_2 \sin \tau + \epsilon a_3 (\cos 3\tau + \sigma_1 \sin 3\tau) + \epsilon^2 a_4 (\cos 5\tau + \sigma_3 \sin 5\tau), \quad (37)$$

$$y = b_1 \sin \tau + b_2 \cos \tau + \epsilon b_3 (\sin 3\tau - \sigma_1 \cos 3\tau) + \epsilon^2 b_4 (\sin 5\tau - \sigma_3 \cos 5\tau),$$

$$z = 0,$$

and

$$x = 0, \quad y = 0, \quad z = c_1 \cos \tau + c_2 \sin \tau + \epsilon c_3 (\sin 3\tau + \sigma_2 \cos 3\tau) + \epsilon^2 c_4 (\sin 5\tau + \sigma_4 \cos 5\tau), \quad (38)$$

respectively, where coefficients a_k, b_k , and $c_k, k = 1, 2, 3, 4$ having the dimensions of length are given in the Appendix. The constants h_2, h_3 , and h_4 for the family of periodic solutions (37) and (38) are determined by Eqs. (25), (29), and (35) and Eqs. (27), (29), and (32), respectively. Note that the families of periodic solutions (37) and (38) contain terms with the

coefficient ε^2 , which can be ignored. Moreover, given the roots θ_k , $k = 1, 2, 3$ of the characteristic equation of system (19), one can unambiguously determine the total orbital period T of the star from equation (15). In this case, equation (16) also allows us to unambiguously determine the variable τ , on which the families of periodic solutions (37) and (38) depend.

Consider now the families of periodic solutions (37) and (38) for $\varepsilon = 0$, i.e., in the case of nonperturbed motion $R = 0$. After elementary manipulations, these families acquire the following form:

$$z = 0, \quad \frac{x^2}{a^2} + \frac{y^2}{b^2} = 1 \quad (39)$$

$$\left(a^2 = a_1^2 + a_2^2, \quad b^2 = \frac{a^2}{\sigma_0^2} \right)$$

and

$$x = 0, \quad y = 0, \quad z = c_1 \cos \tau + c_2 \sin \tau. \quad (40)$$

Therefore, for $\varepsilon = 0$ (in the case of nonperturbed motion $R = 0$), the family of periodic solutions (37) that corresponds to the roots θ_k , $k = 1, 2$ is a family of ellipses in the plane $z = 0$ with the semiaxes a and b defined above. Family (40) that corresponds to the root θ_3 in the case $R = 0$ has the form of the motion along a rectilinear interval of the z axis.

Because $C \leq B \leq A$, and in view of (4), (8), and (21), we have $\sigma_0^2 < 1$, it follows that if the inequality

$$a_1^2 + a_2^2 < \sigma_0^2 B^2 = \sigma_0^2 C^2 (1 + \mu^2) \quad (41)$$

is satisfied, the ellipses of family (39) should be located inside the given elliptical galaxy bounded by ellipsoidal surface (1). If condition

$$|c_1 + c_2| < C \quad (42)$$

is satisfied, the straight-line intervals of family (40) are also located inside the given galaxy.

In view of formulas (XI) given in the Appendix for the quantities a_k , b_k , and c_k , ($k = 1, 2$) in conditions (41) and (42), we obtain

$$|f(c)| < 1, \quad |f(c)| < \frac{1}{1 + \lambda}, \quad (43)$$

respectively. These two conditions for $f(c)$ can be substituted for by the following single condition:

$$|f(c)| = \left| c \left(1 - \frac{3}{2} c^2 \right) \left(1 + c - \frac{3}{2} c^2 \right) \right| < \frac{1}{2}, \quad (44)$$

because $0 < \lambda < 1$. Condition (44) can be rewritten in the form of a double inequality

$$-2 < 9c^5 - 6c^4 - 12c^3 + 4c^2 + 4c < 2, \quad (45)$$

which yields the domain of the variation of arbitrary constant c in the form

$$-0.9613 < c < 1.3042. \quad (46)$$

Here $c_1^* = -0.9613$ and $c_2^* = 1.3042$ are the only real roots of polynomials $f(c) + 1/2$ and $f(c) - 1/2$, respectively. We computed these roots using the MATLAB package. Since the power series of arbitrary constant c converge absolutely only if $|c| < 1$, condition (46) can be rewritten in the following form

$$-0.9613 < c < 1. \quad (47)$$

Note that arbitrary constant c can also be constrained to a more narrow domain:

$$|c| < 0.9613. \quad (48)$$

Thus, if conditions (44) or (47) are satisfied, the ellipses of family (39) and straight-line segments of family (40) are located inside the given elliptical galaxy.

In conclusion, we analyze the ratio of the total orbital periods T of the star (formula (15)) and of the elliptical galaxy $-T_1 = 2\pi/\Omega$ for $\theta = \theta_k$, $k = 1, 2$

$$\frac{T}{T_1} = \frac{\Omega}{\theta_k} (1 + h_2 c^2 + 2h_2 c^3 - 5h_2 c^4), \quad (49)$$

and where $\theta = \theta_3$:

$$\frac{T}{T_1} = \frac{\Omega}{\theta_3} (1 + h_2 c^2 + 2h_2 c^3 - 5h_2 c^4). \quad (50)$$

In Eqs. (49) and (50) we took into account formulas (XIV) and (XV), respectively, from the Appendix. Because $\Omega^2 < V_{03} = \theta_3^2$, it immediately follows from formula (50), to a first approximation, that $T < T_1$ for $\theta = \theta_3$. It is evident that this inequality is also true, to a first approximation, for $\theta = \theta_k$, $k = 1, 2$.

CONCLUSIONS

In this paper, we used the Lyapunov method to construct and analyze the periodic solutions in the vicinity of the central libration point in terms of the three-dimensional problem of the motion of a star inside an inhomogeneous rotating elliptical galaxy with a homothetic density distribution. The coefficients of these periodic solutions contain an arbitrary constant up to the fifth order inclusive.

In the future, we plan to apply our previous results to real elliptical galaxies.

ACKNOWLEDGMENTS

I am grateful to Dr. L.G. Lukyanov for valuable advice and comments.

APPENDIX

The quantities given in (B) have the following form

$$\begin{aligned}
 V_{01} &= \chi_0 \left[1 - \frac{3}{10}(3\lambda^2 + \mu^2) \right. \\
 &\quad \left. + \frac{9}{56}(5\lambda^4 + 2\lambda^2\mu^2 + \mu^4) \right], \\
 V_{02} &= \chi_0 \left[1 - \frac{3}{10}(\lambda^2 + 3\mu^2) \right. \\
 &\quad \left. + \frac{9}{56}(\lambda^4 + 2\lambda^2\mu^2 + 5\mu^4) \right], \\
 V_{03} &= \chi_0 \left[1 - \frac{3}{10}(\lambda^2 + \mu^2) \right. \\
 &\quad \left. + \frac{3}{56}(3\lambda^4 + 2\lambda^2\mu^2 + 3\mu^4) \right], \\
 R_1 &= \chi_1 \left[1 - \frac{5}{14}(5\lambda^2 + \mu^2) \right. \\
 &\quad \left. + \frac{5}{72}(35\lambda^4 + 10\lambda^2\mu^2 + 3\mu^4) \right], \\
 R_2 &= \chi_1 \left[1 - \frac{5}{14}(\lambda^2 + 5\mu^2) \right. \\
 &\quad \left. + \frac{5}{72}(3\lambda^4 + 10\lambda^2\mu^2 + 35\mu^4) \right], \\
 R_3 &= \chi_1 \left[1 - \frac{5}{14}(\lambda^2 + \mu^2) \right. \\
 &\quad \left. + \frac{5}{72}(3\lambda^4 + 2\lambda^2\mu^2 + 3\mu^4) \right], \\
 R_4 &= \chi_1 \left[1 - \frac{15}{14}(\lambda^2 + \mu^2) \right. \\
 &\quad \left. + \frac{5}{24}(5\lambda^4 + 6\lambda^2\mu^2 + 5\mu^4) \right], \\
 R_5 &= \chi_1 \left[1 - \frac{5}{14}(3\lambda^2 + \mu^2) \right. \\
 &\quad \left. + \frac{5}{24}(5\lambda^4 + 2\lambda^2\mu^2 + \mu^4) \right], \\
 R_6 &= \chi_1 \left[1 - \frac{5}{14}(\lambda^2 + 3\mu^2) \right. \\
 &\quad \left. + \frac{5}{24}(\lambda^4 + 2\lambda^2\mu^2 + 5\mu^4) \right],
 \end{aligned}$$

where

$$\begin{aligned}
 \chi_0 &= \frac{Q\rho_0}{3}, \quad \chi_1 = -\frac{Q\rho_1}{5C^2}, \\
 Q &= 4\pi G\sqrt{(1 + \lambda^2)(1 + \mu^2)},
 \end{aligned}$$

and G is the gravitational constant.

The system of equations for x_3, y_3, z_3 :

$$\begin{aligned}
 \frac{d^2x_3}{d\tau^2} - \frac{2\Omega}{\theta} \frac{dy_3}{d\tau} &= -\frac{g_1^2}{\theta^2}x_3 + \frac{2\Omega h_2}{\theta} \frac{dy_1}{d\tau} \\
 + \frac{1}{\theta^2} \left[-2h_2g_1^2 + \varepsilon(R_1x_1^2 + R_4y_1^2 + R_5z_1^2) \right] x_1, \quad (I)
 \end{aligned}$$

$$\begin{aligned}
 \frac{d^2y_3}{d\tau^2} + \frac{2\Omega}{\theta} \frac{dx_3}{d\tau} &= -\frac{g_2^2}{\theta^2}y_3 - \frac{2\Omega h_2}{\theta} \frac{dx_1}{d\tau} \\
 + \frac{1}{\theta^2} \left[-2h_2g_2^2 + \varepsilon(R_4x_1^2 + R_2y_1^2 + R_6z_1^2) \right] y_1, \\
 \frac{d^2z_3}{d\tau^2} &= -\frac{g_3^2}{\theta^2}z_3 \\
 + \frac{1}{\theta^2} \left[-2h_2g_3^2 + \varepsilon(R_5x_1^2 + R_6y_1^2 + R_3z_1^2) \right] z_1.
 \end{aligned}$$

The system of equations for x_4, y_4, z_4 :

$$\begin{aligned}
 \frac{d^2x_4}{d\tau^2} - \frac{2\Omega}{\theta} \frac{dy_4}{d\tau} &= -\frac{g_1^2}{\theta^2}x_4 + \frac{2\Omega}{\theta} \frac{d}{d\tau} (h_3y_1 + h_2y_2) \\
 &\quad - \frac{2}{\theta^2}g_1^2(h_3x_1 + h_2x_2) \\
 &\quad + \varepsilon \left[2(R_1x_1x_2 + R_4y_1y_2 + R_5z_1z_2) \right. \\
 &\quad \left. + (R_1x_1^2 + R_4y_1^2 + R_5z_1^2)x_2 \right], \quad (II) \\
 \frac{d^2y_4}{d\tau^2} + \frac{2\Omega}{\theta} \frac{dx_4}{d\tau} &= -\frac{g_2^2}{\theta^2}y_4 \\
 - \frac{2\Omega}{\theta} \frac{d}{d\tau} (h_3x_1 + h_2x_2) &- \frac{2}{\theta^2}g_2^2(h_3y_1 + h_2y_2) \\
 + \varepsilon \left[2(R_4x_1x_2 + R_2y_1y_2 + R_6z_1z_2)y_1 \right. \\
 &\quad \left. + (R_4x_1^2 + R_2y_1^2 + R_6z_1^2)y_2 \right], \\
 \frac{d^2z_4}{d\tau^2} &= -\frac{g_3^2}{\theta^2}z_4 - \frac{2}{\theta^2}g_3^2(h_3z_1 + h_2z_2) \\
 + \varepsilon \left[2(R_5x_1x_2 + R_6y_1y_2 + R_3z_1z_2)z_1 \right. \\
 &\quad \left. + (R_5x_1^2 + R_6y_1^2 + R_3z_1^2)z_2 \right].
 \end{aligned}$$

The system of equations for x_5, y_5, z_5 :

$$\begin{aligned}
 \frac{d^2x_5}{d\tau^2} - \frac{2\Omega}{\theta} \frac{dy_5}{d\tau} &= -\frac{g_1^2}{\theta^2}x_5 \\
 + \frac{2\Omega}{\theta} \frac{d}{d\tau} (h_4y_1 + h_3y_2 + h_2y_3) \\
 - \frac{g_1^2}{\theta^2} \left[(2h_4 + h_2^2)x_1 + 2h_3x_2 + 2h_2x_3 \right] \\
 + \frac{\varepsilon}{\theta^2} \left[R_1(3x_2^2 + 2h_2x_1^2 + 3x_1x_3)x_1 \right. \\
 &\quad + R_4(2h_2y_1^2 + y_2^2 + 2y_1y_3)x_1 \\
 &\quad + R_5(2h_2z_1^2 + z_2^2 + 2z_1z_3)x_1 \\
 &\quad \left. + R_4(x_3y_1 + 2x_2y_2)y_1 + R_5(x_3z_1 + 2x_2z_2)z_1 \right], \quad (III)
 \end{aligned}$$

$$\begin{aligned}
 \frac{d^2y_5}{d\tau^2} + \frac{2\Omega}{\theta} \frac{dx_5}{d\tau} &= -\frac{g_2^2}{\theta^2}y_5 \\
 - \frac{2\Omega}{\theta} \frac{d}{d\tau} (h_4x_1 + h_3x_2 + h_2x_3)
 \end{aligned}$$

$$\begin{aligned}
& -\frac{g_2^2}{\theta^2} \left[(2h_4 + h_2^2)y_1 + 2h_3y_2 + 2h_2y_3 \right] \\
& + \frac{\varepsilon}{\theta^2} \left[R_2(3y_2^2 + 2h_2y_1^2 + 3y_1y_3)y_1 \right. \\
& \quad + R_4(2h_2x_1^2 + x_2^2 + 2x_1x_3)y_1 \\
& \quad \left. + R_6(2h_2z_1^2 + z_2^2 + 2z_1z_3)y_1 \right. \\
& \left. + R_4(y_3x_1 + 2x_2y_2)x_1 + R_6(y_3z_1 + 2y_2z_2)z_1 \right], \\
& \quad \frac{d^2z_5}{d\tau^2} = -\frac{g_3^2}{\theta^2} z_5 \\
& -\frac{g_3^2}{\theta^2} \left[(2h_4 + h_2^2)z_1 + 2h_3z_2 + 2h_2z_3 \right] \\
& + \frac{\varepsilon}{\theta^2} \left[R_3(3z_2^2 + 2h_2z_1^2 + 3z_1z_3)z_1 \right. \\
& \quad + R_5(2h_2x_1^2 + x_2^2 + 2x_1x_3)z_1 \\
& \quad \left. + R_6(2h_2y_1^2 + y_2^2 + 2y_1y_3)z_1 \right. \\
& \left. + R_5(z_3x_1 + 2x_2z_2)x_1 + R_6(z_3y_1 + 2y_2z_2)y_1 \right].
\end{aligned}$$

The coefficients have the following form

$$\begin{aligned}
c_{33} &= A_0c_{11} \left[\sigma_0^3(\Omega\sigma_0 + 4\theta_k)R_1 - 3\Omega R_2 \right. \\
& \quad \left. + 2\sigma_0(\Omega\sigma_0 - 2\theta_k)R_4 \right], \quad (IV) \\
f_{33} &= \frac{A_0c_{11}}{\sigma_0} \left[-3\Omega\sigma_0^4R_1 + (\Omega + 4\sigma_0\theta_k)R_2 \right. \\
& \quad \left. + 2\sigma_0^2(\Omega - 2\sigma_0\theta_k)R_4 \right], \\
c_{53} &= A_0 \left\{ -\sigma_0^3(\Omega\sigma_0 + 4\theta_k)(3c_{11} - c_{31})\Omega R_1 \right. \\
& \quad \left. - 9\Omega(c_{11} + c_{31})R_2 \right. \\
& \quad \left. + 4\sigma_0[3(\Omega\sigma_0 + \theta_k)c_{11} + (2\Omega\sigma_0 - \theta_k)c_{31}]R_4 \right\}, \\
f_{53} &= \frac{3A_0}{\sigma_0} \left\{ (3c_{11} - c_{31})\sigma_0^4\Omega R_1 \right. \\
& \quad \left. + (\Omega + 4\sigma_0\theta_k)(c_{11} + c_{31})R_2 \right. \\
& \quad \left. - 4\sigma_0^2[(\Omega + \sigma_0\theta_k)c_{11} + \sigma_0\theta_k c_{31}]R_4 \right\}, \\
c_{55} &= B_0 \left\{ (\Omega\sigma_0 + 12\theta_k)\sigma_0^2c_{33}R_1 + 5\Omega f_{33}R_2 \right. \\
& \quad \left. + [(3\Omega\sigma_0 - 4\theta_k)c_{33} - \sigma_0(\Omega\sigma_0 - 8\theta_k)f_{33}]R_4 \right\}, \\
f_{55} &= -\frac{B_0}{\sigma_0} \left\{ 5\Omega\sigma_0^3c_{33}R_1 + (\Omega + 12\sigma_0\theta_k)f_{33}R_2 \right. \\
& \quad \left. + \sigma_0[(3\Omega\sigma_0 - 4\theta_k)f_{33} - (\Omega - 4\theta_k)c_{33}]R_4 \right\}, \\
h_{33} &= -\frac{R_3}{32\theta_3^2} h_{11}(3g_{11}^2 - h_{11}^2), \\
h_{53} &= \frac{3}{h_{11}}(h_{11} + h_{31})h_{33},
\end{aligned}$$

$$h_{55} = \frac{3R_3^2}{1024\theta_3^4} (5g_{11}^4 + h_{11}^4 - 10g_{11}^2h_{11}^2)h_{11}.$$

In addition,

$$A_0 = \frac{3d_{11}^2 - c_{11}^2}{32\sigma_0^2\theta_k} \frac{1}{p_0}, \quad (V)$$

$$B_0 = \frac{5d_{11}^4 + c_{11}^4 - 10d_{11}^2c_{11}^2}{32\sigma_0\theta_k(3d_{11}^2 - c_{11}^2)} \frac{1}{p_0 + 8\Omega^2\sigma_0},$$

where

$$p_0 = (1 + \sigma_0^2)\Omega\theta_k + 2\sigma_0(2\theta_k^2 - \Omega^2). \quad (VI)$$

Because quantities c_{k1} , d_{k1} , g_{k1} , and h_{k1} , $k = 1, 3, 4, 5$ are arbitrary constants, we obtain, by setting $c_{31} = -3c_{11}$ in condition (37) and Eqs. (IV):

$$\begin{aligned}
d_{31} &= -3d_{11}, \quad c_{53} = -6c_{33}, \quad (VII) \\
f_{53} &= -6f_{33}.
\end{aligned}$$

Therefore

$$a_1 = c \left[(1 + c - 3c^2)c_{11} + c_{41}c^3 + c_{51}c^4 \right], \quad (VIII)$$

$$a_3 = c^3(1 + 3c - 6c^2)c_{33},$$

$$a_2 = c \left[(1 + c - 3c^2)d_{11} + d_{41}c^3 + d_{51}c^4 \right],$$

$$a_4 = c_{55}c^5, \quad b_1 = -\frac{a_1}{\sigma_0}, \quad b_2 = \frac{a_2}{\sigma_0},$$

$$b_3 = c^3(1 + 3c - 6c^2)f_{33}, \quad b_4 = f_{55}c^5,$$

$$c_1 = c \left[g_{11}(1 + c) + g_{31}c^2 + g_{41}c^3 + g_{51}c^4 \right],$$

$$g_{31} = \frac{g_{11}}{h_{11}}h_{31},$$

$$c_2 = c \left[h_{11}(1 + c) + h_{31}c^2 + h_{41}c^3 + h_{51}c^4 \right],$$

$$c_3 = c^3 \left[(1 + 3c + 3c^2)h_{11} + 3h_{31}c^2 \right] h_{33},$$

$$c_4 = h_{55}c^5,$$

where

$$\sigma_1 = \frac{d_{11}^2 - 3c_{11}^2}{3d_{11}^2 - c_{11}^2} \frac{d_{11}}{c_{11}}, \quad (IX)$$

$$\sigma_2 = \frac{g_{11}^2 - 3h_{11}^2}{3g_{11}^2 - h_{11}^2} \frac{g_{11}}{h_{11}},$$

$$\sigma_3 = \frac{d_{11}^4 + 5c_{11}^4 - 10d_{11}^2c_{11}^2}{5d_{11}^4 + c_{11}^4 - 10d_{11}^2c_{11}^2} \frac{d_{11}}{c_{11}},$$

$$\sigma_4 = \frac{g_{11}^4 + 5h_{11}^4 - 10g_{11}^2h_{11}^2}{5g_{11}^4 + h_{11}^4 - 10g_{11}^2h_{11}^2} \frac{g_{11}}{h_{11}},$$

and the coefficients c_{nn} , f_{nn} , and h_{nn} , $n = 3, 5$, are given above.

Note that depending on the conditions of the problem under study, we can appropriately choose the arbitrary constants c_{k1} , d_{k1} , g_{k1} , and h_{k1} , $k = 1, 3, 4, 5$.

For example, in view of choice (VII) we can set

$$\begin{aligned}
 c_{11} &= C\sigma_0, & d_{11} &= C\mu\sigma_0, & (X) \\
 g_{11} &= C\lambda, & h_{11} &= C, \\
 c_{31} &= -3C\sigma_0, & c_{41} &= -\frac{3}{2}C\sigma_0, \\
 c_{51} &= \frac{9}{4}C\sigma_0, & d_{31} &= -3C\sigma_0\mu, \\
 d_{41} &= -\frac{3}{2}C\mu\sigma_0, & d_{51} &= \frac{9}{4}C\mu\sigma_0, \\
 g_{31} &= -3C\lambda, & g_{41} &= -\frac{3}{2}C\lambda, \\
 g_{51} &= \frac{9}{4}C\lambda, & h_{31} &= -3C, \\
 h_{41} &= -\frac{3}{2}C, & h_{51} &= \frac{9}{4}C.
 \end{aligned}$$

In this case we obtain for $a_k, b_k,$ and $c_k, k = 1, 2, 3, 4,$ the following equalities:

$$\begin{aligned}
 a_1 &= C\sigma_0 f(c), & a_2 &= C\mu\sigma_0 f(c), & (XI) \\
 a_3 &= c_{33}h(c), & a_4 &= c_{55}c^5, \\
 b_1 &= -Cf(c), & b_2 &= C\mu f(c), \\
 b_3 &= f_{33}h(c), & b_4 &= f_{55}c^5, \\
 c_1 &= C\lambda f(c), & c_2 &= Cf(c), \\
 c_3 &= h_{33}h(c), & c_4 &= h_{55}c^5,
 \end{aligned}$$

where

$$\begin{aligned}
 f(c) &= c\left(1 - \frac{3}{2}c^2\right)\left(1 + c - \frac{3}{2}c^2\right), & (XII) \\
 h(c) &= c^3(1 + 3c - 6c^2),
 \end{aligned}$$

λ and μ are the second eccentricities of the given elliptical galaxy, and σ_0 is determined by equation (21). In addition, quantities $\sigma_k, k = 1, 2, 3, 4,$ have the following form

$$\sigma_1 = \frac{\mu^2 - 3}{3\mu^2 - 1}\mu, \quad \sigma_2 = \frac{\lambda^2 - 3}{3\lambda^2 - 1}\lambda, \quad (XIII)$$

$$\begin{aligned}
 \sigma_3 &= \frac{\mu^4 - 10\mu^2 + 5}{5\mu^4 - 10\mu^2 + 1}\mu, \\
 \sigma_4 &= \frac{\lambda^4 - 10\lambda^2 + 5}{5\lambda^4 - 10\lambda^2 + 1}\lambda.
 \end{aligned}$$

We then obtain for $h_n, n = 2, 3, 4$ for $\theta = \theta_k, k = 1, 2$

$$\begin{aligned}
 h_2 &= \frac{1 + \mu^2}{8\theta_k} \frac{C^2\varepsilon}{\xi_0^2 + \eta_0^2} \\
 &\times \left[3\sigma_0^3\xi_0 R_1 + 3\eta_0 R_2 + \sigma_0(\xi_0 + \sigma_0\eta_0)R_4 \right], & (XIV) \\
 h_3 &= 2h_2, & h_4 &= -5h_2, \\
 \xi_0 &= \sigma_0\theta_k - \Omega, & \eta_0 &= \theta_k - \Omega\sigma_0.
 \end{aligned}$$

The same quantities for $\theta = \theta_3$ are equal to

$$\begin{aligned}
 h_2 &= \frac{3C^2\varepsilon R_3}{8\Omega^2} (1 + \lambda^2), & (XV) \\
 h_3 &= 2h_2, & h_4 &= -5h_2.
 \end{aligned}$$

REFERENCES

1. V. K. Abalkin, *Byull. ITA* **7**, 327 (1959).
2. G. N. Duboshin, *Celestial Mechanics. Analytical Procedures and Qualitative Methods* (Nauka, Moscow, 1964) [in Russian].
3. S. A. Gasanov, *Pis'ma Astron. Zh.* **27**, 150 (2001) [*Astron. Lett.* **27**, 124 (2001)].
4. S. A. Gasanov and L. G. Luk'yanov, *Astron. Zh.* **79**, 944 (2002) [*Astron. Rep.* **46**, 851 (2002)].
5. A. M. Lyapunov, *Collected Works* (Izd. Akad. Nauk SSSR, Moscow, 1956) [in Russian].
6. N. M. Matveev, *Integration of Ordinary Differential Equations* (Vysshaya Shkola, Moscow, 1967) [in Russian].
7. K. F. Ogorodnikov, *Dynamics of Stellar Systems* (GIFML, Moscow, 1958) [in Russian].
8. H. Poincare, *Lecons sur les Hypotheses Cosmogoniques* (Librairie Scientifique A. Hermann et fils, Paris, 1911).